Fakultät Maschinenwesen
der Technischen Universität Dresden

Synthesis, characterization and modification of carbon nanomaterials

Dissertation

zur Erlangung des akademischen Grades
Doktoringenieur
(Dr.-Ing.)

vorgelegt von

Dipl.-Ing. Franziska Schäffel
geboren am 29.08.1980 in Dresden

It appears to be true that 'having an idea'
is not necessarily the result of some great mental leap:
it is often the result of merely being able, for one sublime moment,
to avoid being stupid!

Sir Alan Walsh

Eingereicht am:	09.10.2009
Tag der Verteidigung:	09.12.2009
Gutachter:	Prof. Dr. L. Schultz Prof. Dr. G. Cuniberti

Contents

1 Introduction

Carbon is an extraordinary and presumably the most diverse element in the periodic table. The interest in carbon arises from the variety of structural forms in which this element appears in our lives. This peculiarity stems from its ability to form different types of valence bonds through atomic orbital hybridization. Thus carbon structures appear in all dimensions, viz. diamond (3d), graphite or better graphene (2d), carbon nanotubes (1d) and fullerenes (0d). As diverse the structures are as divers are the properties of carbon structures. For example, while diamond is insulating, single walled carbon nanotubes (SWCNT) can be semiconducting or metallic [1].

With the discovery of fullerenes in 1985 [2] and carbon nanotubes (CNT) in 1991 [3] research in carbon nanostructures erupted and has not ebbed away to date. Many believe that Iijima's report in 1991 is of particular importance because it gave clear experimental evidence for the existence of CNT and a description of their structure thereby bringing carbon nanotubes into the awareness of the scientific community as a whole [3]. However, some 40 years before L. Radushkevich and V. Lukyanovich reported on tubular hollow graphite fibers with a diameter of 50 nm, which were most probably the first multi walled CNT (MWCNT) grown from iron catalysts [4]. Acknowledgement of the discovery of CNT should also go to R. Bacon and M. Endo. R. Bacon synthesized graphite whiskers in the late 1950's, introduced a scroll structure model, and reported on their exceptional mechanical strength for the first time [5]. The impressive work on filamentous carbon of M. Endo in the 1970's included their structural characterization as "hollow tubes" consisting of concentric carbon sheets "like the annual ring structure of a tree", much as we like to describe MWCNT these days [6].

The unique and extraordinary properties of CNT have attracted widespread attention and make them attractive for many applications. A SWCNT may be envisaged as a cylinder obtained by rolling up a planar strip of graphene, i.e. a single layer of sp^2-hybridized carbon. The unique electronic and mechanical properties of these molecular nanostructures make them one of the most promising building blocks for nanoscale science and nanotechnology. Their small size, unrivaled aspect ratio, ballistic transport properties, large current density, and outstanding mechanical properties render CNT promising candidates for applications in nanoelectronics, nanomechanics, and composite materials [1; 7–9]. Many of these applications demand very pure CNT with a well-defined CNT diameter distribution on a bulk scale.

A wide variety of techniques has been developed over the years to fabricate CNT. The most established synthesis routes are those utilizing arc discharge, laser ablation, and chemical vapor deposition (CVD). All of these methods lead to CNT material with different characteristics that may be used in different fields. In most techniques catalyst materials, mainly the transition metals iron, cobalt, and nickel, are used to promote CNT nucleation and growth. In comparison to laser evaporation and arc discharge, chemical vapor deposition (CVD) is advantageous due to its upward scalability, low cost, and rather low production temperatures [10–14]. Furthermore, substrate-based CVD techniques, where the catalyst is situated on a substrate, allow for the synthesis of aligned CNT [15] at defined positions [16–18] and thus hold significant potential for the integration of CNT into nanoelectronic devices. In CVD processes, the formation of CNT is stimulated by the presence of metal catalyst particles. Carbon species are formed through the catalytic dehydrogenation of a hydrocarbon precursor at the catalyst surface. CNT growth is generally assumed to occur via carbon dissolution into the metal nanoparticles and subsequent carbon precipitation from the saturated metal particle thereby forming tubular sp^2-hybridized carbon solids [19].

The expectations from CNT technology are high. However, significant problems have to be overcome until CNT can reliably be utilized in real applications other than providing mechanical strength in bulk CNT composit materials. The electronic properties of SWCNT depend sensitively on their diameter and chirality, giving rise to either metallic or semiconducting properties [20; 21]. The realization of CNT-based nanoelectronics requires detailed knowledge of the CNT's electronic properties and the ability to modify them in a controlled manner. Although CNT are meanwhile studied for almost two decades, the synthesis of SWCNT in high yield with accurate diameter and chirality control remains a challenge. A key aspect in addressing this challenge is an improved understanding of the nucleation and growth mechanisms essential for the formation of CNT.

The present thesis aims to provide new insights into several aspects of CNT research. This includes investigations of the *controlled growth of CNT from pre-engineered catalyst particles*. Conventional catalyst materials such as iron and cobalt are utilized to catalyze the CNT formation. The preparation of catalyst particles is a very crucial step in CNT synthesis. In this work gas-phase prepared nanoparticles have been used as pre-defined catalyst which was readily deposited onto appropriate substrates for CNT synthesis in CVD. This type of catalyst is advantageous over thin film catalysts, where the catalytically active islands, also called "catalyst particles", form *in situ* and can thus not be independently controlled.

The gas-phase approach further allows for a comprehensive characterization of the catalyst particles *prior* to the CNT synthesis reaction and thus allows to correlate catalyst and CNT morphologies which in turn is essential to gaining deeper insight in the *CNT growth mechanisms* involved. Conventional growth models assume that CNT growth occurs at atomic steps on the surface of the catalyst particle. However, the data obtained within the present study rather point to CNT growth from the oxide support as mediated by the interaction between the metallic catalyst particle and the oxidic substrate.

Further, *catalytic hydrogenation* of graphite in hydrogen atmosphere has been investigated. This process can be considered the reverse to the process of CNT formation, with the same reaction partners involved. Metallic nanoparticles are dispersed onto graphite and exposed to hydrogen at elevated temperatures. As opposed to the formation of graphitic carbon via dissolution of carbon in and precipitation from a catalyst, catalytic hydrogenation results in carbon removal from an exposed graphite edge. The catalyst helps to dissociate molecular hydrogen which then reacts with carbon (from the graphite) to form methane, leaving an etch track behind [22; 23]. Catalytic hydrogenation is a potential key engineering route for the fabrication of graphene-based devices with atomic precision and has hence attracted tremendous interest recently [24–26]. The hydrogenation mechanism, though, is poorly understood. Thus, complementary to the CNT growth studies, cobalt catalyzed hydrogenation of graphite is exploited and investigations using aberration-corrected high-resolution transmission electron microscopy are conducted to gain insight into the hydrogenation reaction. This study is intended to deepen the understanding of the mutual interplay between metal catalyst particle, carbon, and hydrogen for both de-hydrogenation (CNT growth) and hydrogenation (etching) processes.

Within the development of a CNT technology as a whole the functionalization of CNT has evolved to be a very important research field, since it allows for a tailored modification of the chemical and physical properties of CNT. Especially, selective functionalization of the CNT ends is envisaged to provide new possibilities for building CNT architectures and networks for, e.g., nanoelectromechanical systems (NEMS). A second objective of this thesis is the *hard magnetic termination and thus functionalization of CNT tips.* In these studies FePt is utilized as hard magnetic catalyst material in a CVD process, and the synthesis conditions are tuned to obtain CNT with a hard magnetic particle at each tip via the so-called tip growth mode [27]. Chemically $L1_0$-ordered FePt exhibits a very large magneto-crystalline anisotropy [28]. This allows for a reduction of the nanoparticle size to below 4 nm at room temperature while still retaining the stability of the magnetization against thermal fluctuations and demagnetization [29]. Hence, a combination of such a nanoparticulate hardmagnet with a CNT is of strong interest in ferromagnetic nanodevices, e.g. as tips for magnetic force microscopy or magnetically actuated NEMS. Here, two synthesis approaches are followed:

- CNT growth from FePt in *thermally activated* CVD: The CNT are fabricated from gas-phase prepared FePt nanoparticles via thermally activated CVD (TCVD). Although FePt is hardly used as catalyst for CNT synthesis these experiments demonstrate the general possibility to grow CNT from FePt and provide important data to further our understanding of the CNT growth mechanisms.
- CNT growth from FePt in *plasma enhanced* CVD: Here, CNT are mainly grown from Fe-Pt multi-layer thin films as well as from chemically prepared FePt nanoparticles in plasma enhanced CVD (PE-CVD). Since PE-CVD is a method known to yield CNT with a catalyst particle at the tip, the latter is the most promising approach for the realization of hard-magnetically terminated CNT.

2 Fundamentals

In this chapter, a brief introduction of the fundamentals of graphene is presented, as CNT can basically be envisaged as rolled up sheets or strips of graphene. The second part introduces the CNT themselves, including important facts on their structure, properties and synthesis. The actual ideas on CNT growth mechanisms are then delineated, since the present investigations provide valuable data for an understanding of the CNT growth. In a third part the catalytic hydrogenation of graphite, i.e. the etching of graphite via a process reverse to the formation of CNT, is described. Finally, the FePt alloy system and its suitability as hard magnetic catalyst material for CNT synthesis is introduced.

2.1 Basics of graphene

Carbon is the sixth element in the periodic table with electrons in the $1s^2$, $2s^2$ and $2p^2$ atomic orbitals. It shows a high affinity to form covalent bonds to various elements including other carbon atoms. Carbon atoms can be $sp-$, sp^2- and sp^3-hybridized and thus form linear, trigonal and tetragonal structures. In graphite, the sp^2-hybridized carbon atoms are hexagonally arranged to form a planar two-dimensional honeycomb lattice (the so-called graphene layer) with a lattice constant $a = \sqrt{3}a_0$ where $a_0 = 142\,\mathrm{pm}$ is the nearest neighbor inter-atomic distance [30]. The inter-plane distance between two adjacent graphene layers is $335\,\mathrm{pm}$ [30]. While the in-plane $\sigma-$bonds with the graphene layers are even stronger than the C-C bonds in sp^3-hybridized diamond, the inter-plane bonds are very weak van der Waals forces, leading to an easy shearing of graphite along the layer plane.

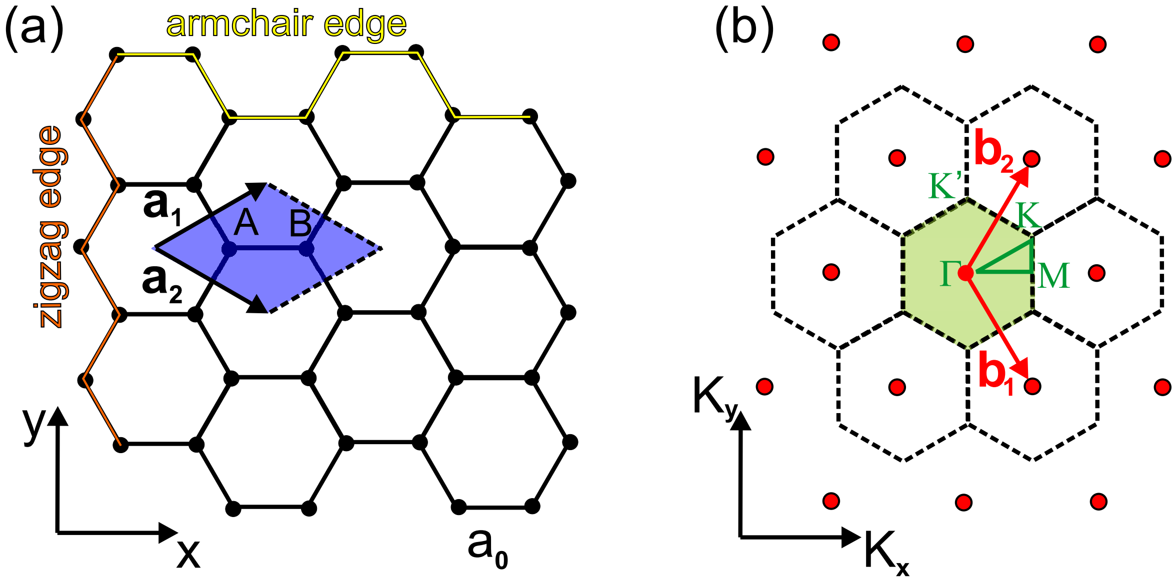

Figure 2.1: Crystal structure of graphene: a) 2-dimensional hexagonal lattice of a graphene sheet with basis vectors $\mathbf{a}_1$ and $\mathbf{a}_2$. The unit cell is indicated in blue. The graphene armchair and zigzag edges are highlighted in yellow and orange, respectively. b) Reciprocal lattice (dashed) with reciprocal lattice vectors $\mathbf{b}_1$ and $\mathbf{b}_2$. The first Brillouin zone is marked green.

The hexagonal lattice of graphene is shown in Figure 2.1 a. The unit cell is a rhombus (blue) with a basis of two non-equivalent carbon atoms (A and B). Expressed in cartesian coordinates x and y the real space basis vectors $\mathbf{a}_1$ and $\mathbf{a}_2$ are

$$\mathbf{a}_1 = (\sqrt{3}a/2; a/2) \qquad \mathbf{a}_2 = (\sqrt{3}a/2; -a/2). \tag{2.1}$$

The graphene armchair and zigzag edges are highlighted in yellow and orange, respectively. The corresponding reciprocal lattice is depicted in Figure 2.1 b together with the first Brillouin zone (green), the high symmetry points (Γ, M, K), and the reciprocal basis vectors $\mathbf{b}_1$ and $\mathbf{b}_2$, given by

$$\mathbf{b}_1 = (2\pi/\sqrt{3}a; 2\pi/a) \qquad \mathbf{b}_2 = (2\pi/\sqrt{3}a; -2\pi/a). \tag{2.2}$$

Figure 2.2 shows the band structure of isolated graphene. The conduction and valence bands touch at the six corners of the first Brillouin zone (K, K') and have a linear dispersion near the Fermi edge [31; 32]. At these touching points, the electronic density of states is zero. This is why graphene is called a zero-gap semiconductor or zero-overlap semimetal.

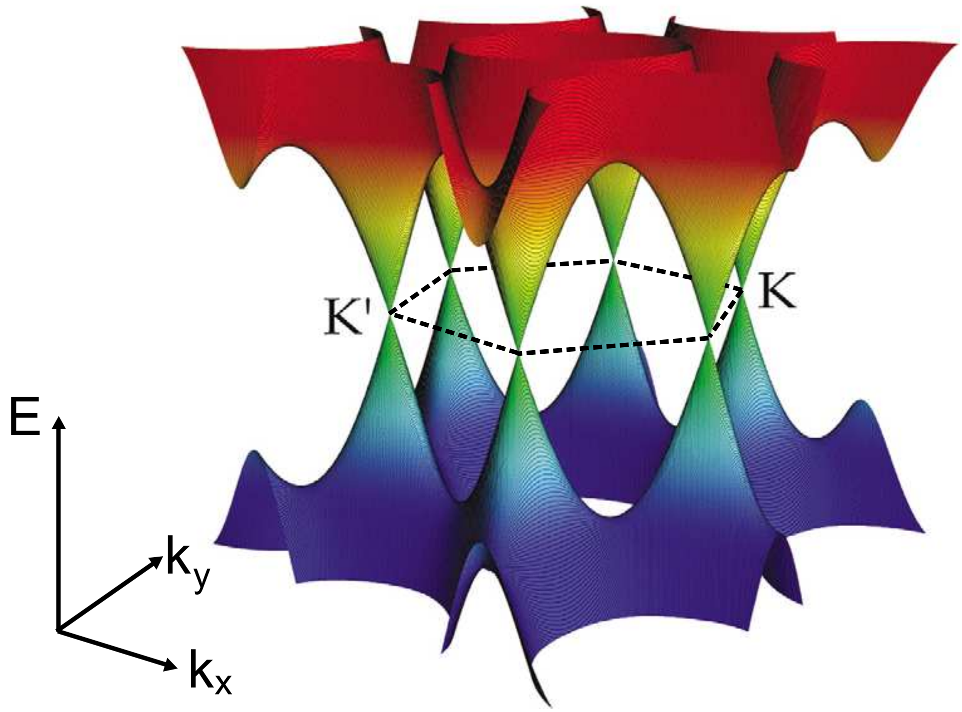

Figure 2.2: Band structure of graphene [33]. The conduction and valence bands touch at the six corners of the first Brillouin zone.

The isolation of graphene in 2004 has made it a subject of intense focus in both basic and applied research [31]. Unique electronic properties, such as its high intrinsic carrier mobility at room temperature [34; 35], make graphene a promising candidate for new-generation molecular electronics applications, e.g. for graphene-based interconnects and field-effect transistors [36]. The electronic properties of graphene depend sensitively on the number of graphene layers [32]. Only single layer and double layer graphene are zero-gap semiconductors with only a single type of electrons and holes, respectively. In the case of the so-called few layer graphene (3 to $<$ 10 layers), the conduction and valence bands start to overlap, and several charge carriers appear [37; 38]. Thicker graphene structures can be considered as thin films of graphite.

2.2 Basics of carbon nanotubes

2.2.1 Structure and electronic properties

The variety of CNT is roughly divided in multi-wall CNT (MWCNT) and single-wall CNT (SWCNT). In 1991, MWCNT were identified by S. Iijima who examined carbon soot as obtained from arc discharge of graphite electrodes via transmission electron microscopy (TEM) [3]. He observed coaxial tubes of graphene sheets. Two years later, SWCNT formed of only a single rolled-up sheet of graphene were successfully synthesized and identified by two independent groups [39; 40].

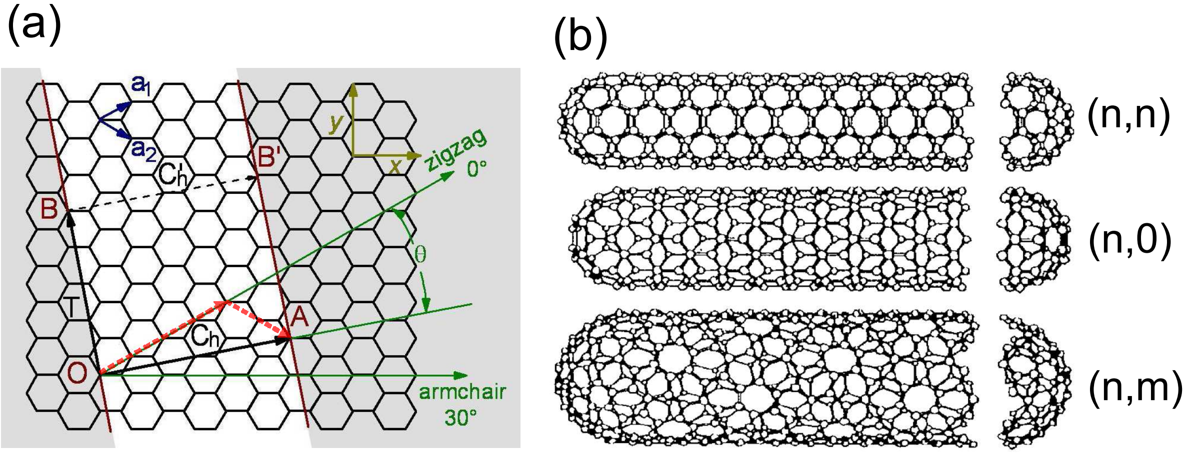

Figure 2.3: Structures of SWCNT: a) Hexagonal lattice of graphene [41]. A graphene strip (white) is rolled up along the chiral vector $\mathbf{C}_h = 4{\cdot}\mathbf{a}_1 + 2{\cdot}\mathbf{a}_2$ into a (4,2) chiral SWCNT. The translation vector $\mathbf{T} = 4{\cdot}\mathbf{a}_1 - 5{\cdot}\mathbf{a}_2$ runs along the SWCNT axis. b) Classification of the three types of SWCNT, i.e. armchair (5,5), zigzag (9,0) and chiral (10,5) nanotubes (from top to bottom) [1].

Since the rolling up of graphene strips to form a SWCNT can be carried out in various different directions, e.g. armchair, zigzag, or any direction in between, an infinite number of different SWCNT structures can be generated. Figure 2.3 a shows the planar honeycomb lattice of a graphene sheet. A strip of graphene (white) is rolled up such that the lattice points O and A, and B and B', coincide. The vector **OA** defines the chiral or Hamada vector $\mathbf{C}_h$ [21] which provides an unambiguous notation of a SWCNT structure. It can be expressed as a linear combination of the real space basis vectors $\mathbf{a}_1$ and $\mathbf{a}_2$ of the graphene lattice:

$$\mathbf{C}_h = n \cdot \mathbf{a}_1 + m \cdot \mathbf{a}_2 \equiv (n, m) \qquad (n, m \text{ are integers}, 0 \leq |m| \leq |n|). \tag{2.3}$$

Only integers are allowed for n and m. Depending on the chiral vector, SWCNT can be classified in three groups presented in Figure 2.3 b: armchair (n,n), zigzag (n,0), and chiral (n,m) SWCNT. The specific chiral vectors for the SWCNT displayed in Figure 2.3 are (4,2) (Fig. 2.3 a), (5,5), (9,0), and (10,5) (Fig. 2.3 b) [1].

The length of the chiral vector determines the circumference of the SWCNT. Thus the SWCNT diameter d can be directly deduced from the chiral vector and is defined as

$$d = \frac{|\mathbf{C}_h|}{\pi} = \frac{a \cdot \sqrt{n^2 + m^2 + nm}}{\pi}. \tag{2.4}$$

The chiral angle Θ is defined as the angle between the zigzag direction $\mathbf{a}_1$ and the chiral vector $\mathbf{C}_h$ (cf. Fig. 2.3). It is thus equal to the tilt angle of the hexagons with respect to the SWCNT axis and can be directly deduced from $\mathbf{C}_h$ as

$$\cos\Theta = \frac{\mathbf{C}_h \cdot \boldsymbol{a}_1}{|\mathbf{C}_h| \cdot |\boldsymbol{a}_1|} = \frac{2n + m}{2 \cdot \sqrt{n^2 + m^2 + nm}} \qquad (0^\circ \leq |\Theta| \leq 30^\circ). \tag{2.5}$$

Thus, the achiral zigzag and armchair nanotubes possess chiral angles of $\Theta = 0$ and $\Theta = 30^\circ$, respectively. All other nanotubes with $-30^\circ < \Theta < 30^\circ$ are chiral, with right handed helices for $\Theta > 0$ and left handed helices for $\Theta < 0$.

The vector **OB** is called the translation vector **T** which is parallel to the tube axis and normal to the chiral vector in the unrolled honeycomb lattice. It is defined by the first lattice point reached by a vector which is parallel to the tube axis and originates in O. It can be expressed as

$$\mathbf{T} = t_1 \cdot \mathbf{a}_1 + t_2 \cdot \mathbf{a}_2 \qquad \text{with } t_1 = \frac{2m + n}{d_R},\ t_2 = -\frac{2n + m}{d_R}. \tag{2.6}$$

Here, d_R is the greatest common divisor of (2m+n) and (2n+m). In the example in Figure 2.3 a the translation vector is $\mathbf{T}=4\cdot\mathbf{a}_1-5\cdot\mathbf{a}_2 \equiv (4,-5)$. While the vectors $\mathbf{a}_1$ and $\mathbf{a}_2$ define the area of the unit cell of the graphene lattice, the unit cell of the likewise defined SWCNT is given by the rectangle generated by $\mathbf{C}_h$ and $\mathbf{T}$. The number of hexagons per unit cell, N, can now be derived by dividing the surface area of the SWCNT unit cell by the area of the graphene unit cell

$$N = \frac{|\mathbf{C}_h \times \mathbf{T}|}{|\mathbf{a}_1 \times \mathbf{a}_2|} = \frac{2(n^2+m^2+nm)}{d_R}. \tag{2.7}$$

It has been shown that carbon nanotubes are capped by a fullerene-like hemisphere on each end. Their effect on the mechanical and electronic properties of the nanotubes can be neglected due to the extreme aspect ratio of typically 10^4 to 10^7 [1; 42]. However, they seem to play an important role in CNT nucleation as will be discussed later in this chapter. Further, SWCNT tend to agglomerate to bundles with hexagonal structure due to inter-tube van der Waals interactions.

A major problem in current CNT research is the control of their electronic properties, which strongly depend on the angle at which a graphene strip is rolled up to form a single-wall CNT. A large variety of metallic and semiconducting CNT can be obtained this way. In order to derive the electronic properties of SWCNT, a description in reciprocal space is reasonable. As shown in chapter 2.1, the first Brillouin zone of graphene is a hexagon around the Γ point with linearly dispersed valence and conduction bands touching at the hexagon corners, i.e. at the K and K' points. Upon rolling an infinitely long graphene strip to a SWCNT the rolling direction defines the boundary conditions for the wavefunction in the graphene lattice and hereby determines the quantization of the allowed wave vectors. The reciprocal vectors $\mathbf{K}_T$ along the nanotube axis and $\mathbf{K}_C$ along the circumferential direction are parallel to $\mathbf{T}$ and $\mathbf{C}_h$, respectively. They can be derived from the orthogonality relation $\mathbf{R}_i \cdot \mathbf{K}_j = 2\pi\delta_{ij}$, where $\mathbf{R}_i$ and $\mathbf{K}_j$ denote corresponding lattice vectors of the real and the reciprocal space, respectively. Due to the infinite length of the SWCNT only $\mathbf{K}_T$ is continuous in the Brillouin zone, while $\mathbf{K}_C$ gives discrete k values along the $\mathbf{C}_h$ direction. Using equations 2.6 and 2.7 and the relations

$$\mathbf{C}_h \cdot \mathbf{K}_C = 2\pi, \qquad \mathbf{T} \cdot \mathbf{K}_C = 0, \qquad \mathbf{C}_h \cdot \mathbf{K}_T = 0, \qquad \mathbf{T} \cdot \mathbf{K}_T = 2\pi, \tag{2.8}$$

$\mathbf{K}_C$ and $\mathbf{K}_T$ can be expressed as

$$\mathbf{K}_C = \frac{1}{N}(-t_2\mathbf{b}_1 + t_1\mathbf{b}_2), \qquad \mathbf{K}_T = \frac{1}{N}(m\mathbf{b}_1 - n\mathbf{b}_2) \tag{2.9}$$

with $\mathbf{b}_1$ and $\mathbf{b}_2$ being the reciprocal lattice vectors of graphene (cf. equation 2.2). The first Brillouin zone of a SWCNT is therefore represented by a set of parallel line segments with length $|\mathbf{K}_T|$ and distance $|\mathbf{K}_C|$. Two points in reciprocal space that differ by $N\mathbf{K}_C = (-t_2\mathbf{b}_1 + t_1\mathbf{b}_2)$ are equivalent, since $N\mathbf{K}_C$ corresponds to a reciprocal lattice vector. None of the other vectors $q\mathbf{K}_C$ with $q = 1, \ldots, N$-1 (with N being the number of hexagons per unit cell, cf. equation 2.7) are reciprocal lattice vectors of graphene, because t_1 and t_2 do not have a common divisor other than unity. The SWCNT reciprocal lattice vectors can be expressed as

$$\mathbf{K} = \mu\frac{\mathbf{K}_T}{|\mathbf{K}_T|} + q\mathbf{K}_C, \qquad \text{with integer} \;\; q = 0, ..., N \;\; \text{and} \;\; -\frac{\pi}{|\mathbf{T}|} < \mu < \frac{\pi}{|\mathbf{T}|}. \tag{2.10}$$

Therefore, N allowed wave vectors $q\mathbf{K}_C$ give rise to a set of N parallel line segments in reciprocal space separated by $|\mathbf{K}_C|$. The length of these line segments, $|\mathbf{K}_T|$=$2\pi/|\mathbf{T}|$, represents the length of the one dimensional first Brillouin zone [1].

Figure 2.4 shows exemplarily the first Brillouin zones of a (10,10) armchair SWCNT (Fig. 2.4 a) and a (17,0) zigzag SWCNT (Fig. 2.4 b). The line segments of the metallic (10,10) SWCNT cross the corners (K, K') of the first Brillouin zone of graphene, while the segments of the semiconducting (17,0) nanotube miss them. The dispersion relations and the densities of states (DOS) of the (10,10) armchair and the (17,0) zigzag nanotube clearly demonstrate their metallic and semiconducting properties, respectively (Figure 2.5, [41]). While the bands cross the Fermi level where the DOS is finite in case of the (10,10) SWCNT, the band structure of the (17,10) SWCNT exhibits a gap and the DOS vanishes at the Fermi level.

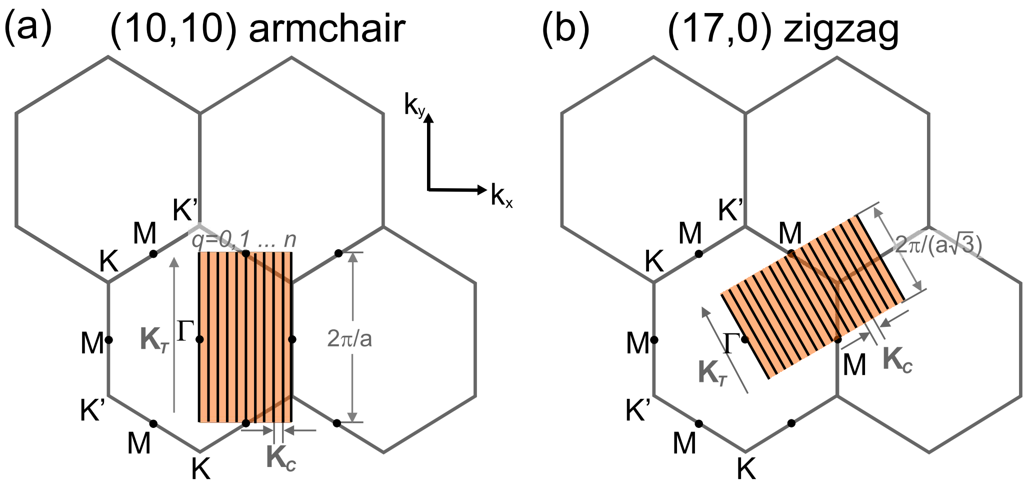

Figure 2.4: (a) Brillouin zone of a (10,10) armchair SWCNT. (b) Brillouin zone of a (17,0) zigzag SWCNT. The segment length is $2\pi/a$ for a (n, n) nanotube giving rise to $n+1$ ($n = N/2$, here: 11) black lines in the marked region in a). These lines are parallel to $\mathbf{K}_T$, i.e. parallel to the nanotube axis. For the (17,0) zigzag tube in b) the first Brillouin zone consists of 18 lines in the marked region that are rotated by 30°. The length of the first Brillouin zone is $2\pi/(a\sqrt{3})$.

In summary, the electronic properties of SWCNT depend sensitively on their structure, as defined by the chiral indices or the angle at which the graphene strip is rolled up. This is a major problem in CNT research to be overcome if CNT are to be integrated into nanoelectronics.

2.2.2 Synthesis of carbon nanotubes

A large variety of methods has so far been developed to synthesize CNT. Among these, the traditional arc-discharge routes [3; 43], laser evaporation [44; 45] and chemical vapor deposition (CVD) [10; 13; 15] are the three primarily employed techniques. After a brief summary of the first two methods, CVD will be described in more detail, as it is by far

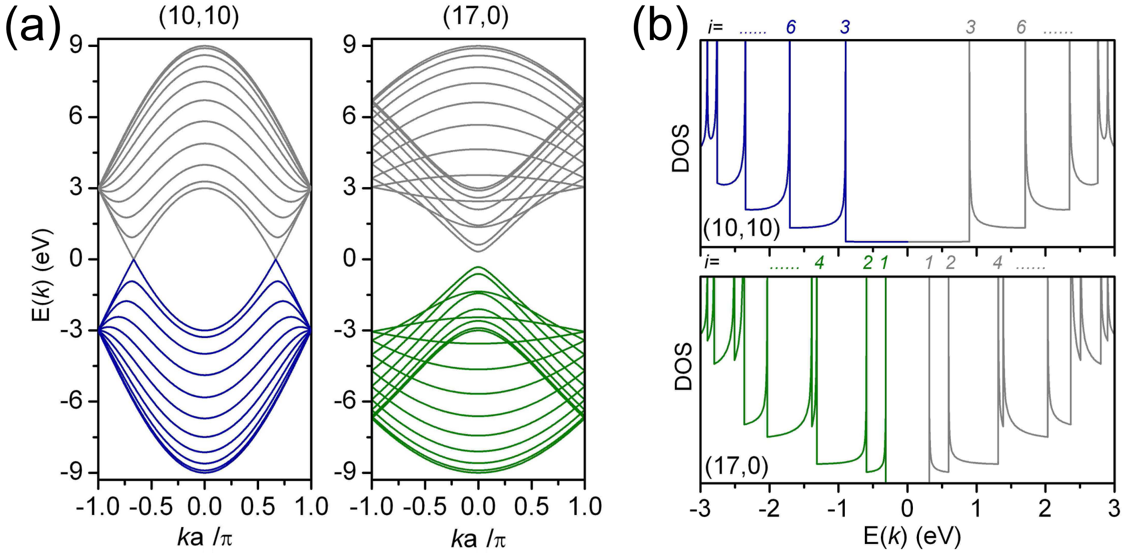

Figure 2.5: a) Band structures of a metallic (10,10) and a semiconducting (17,0) SWCNT. b) Corresponding densities of states (DOS). [41]

the most active area in the synthesis of carbon nanotubes, and it is also the approach used in the present investigations.

Arc discharge

Historically, electric arc discharge is the method that lead to the discovery of multi-wall CNT [3] and later became the first method to produce single-wall CNT [39; 40]. Already in 1992, T. Ebbesen and P. M. Ajayan reported on the synthesis of MWCNT in macroscopic quantities via this method [46]. In arc discharge, a voltage of approx. 20 to 35 V is applied between two high-purity graphite electrodes in an inert gas atmosphere. The gas between the electrodes is ionized and a hot plasma is formed. Due to the high temperatures of the arc of up to 3000 K carbon sublimes from the positive electrode and is deposited as soot on the negative electrode. Arc discharge methods inherently yield a variety of sp^2 carbon materials, mainly fullerenes and MWCNT. The addition of a few at.-% metal catalyst material to the negative electrode leads to the formation of

SWCNT [39; 40]. An optimization of SWCNT synthesis with arc discharge was achieved by Journet et al. by adding 1 at.-% yttrium and 4.1 at.-% nickel as catalyst to the carbon rod [47]. Yields of up to 80 % SWCNT have been reported [47].

Laser ablation

Another well established CNT synthesis method is laser ablation [44; 48], which historically lead to the discovery of fullerenes [2]. Here, a laser is used to vaporize a graphite target which is pre-mixed with a few at.-% of a catalyst material. The target is typically kept at temperatures at or above 1000 °C in an inert gas environment such as nitrogen, argon, or helium. SWCNT form in the gas phase and are transported towards a cold finger in the inert gas flow. For the carbon vaporization, continuous [49] or pulsed laser setups [50] are used. SWCNT yields of up to 70 % can be obtained. SWCNT obtained from laser ablation have a very uniform diameter and tend to bundle up into ropes. This method is advantageous in that it yields CNT material that can easily be purified by acid treatment [51]. These CNT in general contain very few structural defects. Further, it allows for a fine tuning of the diameter and the diameter distribution of the SWCNT, e.g. by applying different furnace temperatures [52]. Due to the low production rate and the high cost of special lasers it is not the most economic method. The high quality of the obtained CNT material, however, makes this method indispensable for fundamental research.

Chemical vapor deposition

Over the years, a wide variety of chemical vapor deposition (CVD) methods has been developed including plasma-enhanced (PE-CVD) [15; 53], laser-assisted [54] or thermally activated chemical vapor deposition (TCVD) [13]. CVD is by far the most frequently used method of CNT synthesis, since CVD techniques are advantageous in that they allow low-temperature and large-scale synthesis of CNT [11–14]. The different CVD routes generally involve a catalyst which helps to decompose a hydrocarbon at elevated temperatures (~400 °C - 1000 °C). In most of the CVD methods ethylene or acetylene are used as the carbon feedstock. The common understanding of the CVD growth of CNT is that the hydrocarbon is decomposed, the carbon then dissolves in the catalyst, and when the catalyst is supersaturated with carbon, the latter precipitates in form of a nanotube. In floating catalyst approaches, a metal catalyst precursor is usually sublimed in one zone of a CVD reactor, the metal atoms nucleate and grow to particles along the flow direction of the process gases and help to decompose the carbon source in the CNT nucleation zone of the oven. The CNT are thus nucleated in the gas flow [55] which makes this method suitable for continuous CNT production [14]. In supported catalyst CVD routes the catalyst is deposited onto a suitable substrate, e.g. onto Si, SiO_2, or Al_2O_3 (Fig. 2.6). Here, a localized growth of CNT at specific positions is feasible [16]. Furthermore, substrate-based CVD allows for the synthesis of vertically aligned CNT [15]. Recently, the horizontal growth of CNT as obtained from alignment in the gas flow direction has intensively been studied. This technique allows for the fabrication of flat CNT networks and thus holds great potential for the integration of CNT into nanoelectronic devices [56; 57].

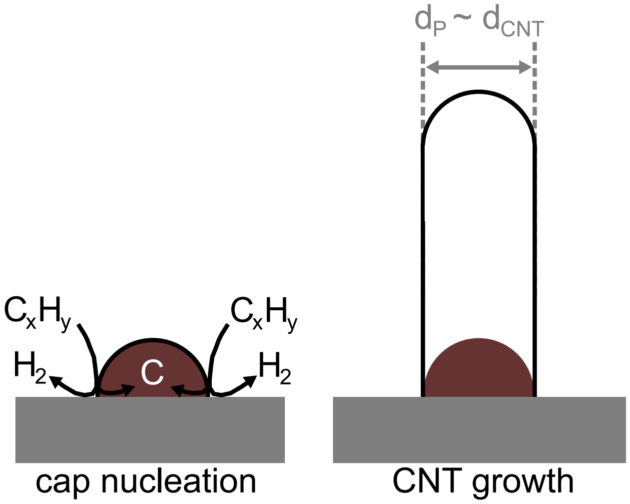

Figure 2.6: Scheme of substrate-based CVD. The carbon source is decomposed at the catalyst surface. Upon supersaturation of the catalyst particle with carbon, carbon is precipitated as a graphitic nucleation cap. Further incorporation of carbon leads to nanotube growth. Commonly, the CNT diameter d_{CNT} is predetermined by the particle diameter d_P.

In substrate-based CVD, the preparation of the catalyst material is a crucial step, since in many cases the diameter of the metallic catalyst particles d_P determines the diameter of the nanotube d_{CNT} as is schematically shown in Figure 2.6. Commonly, thin metal films are deposited onto a support [58; 59]. Upon heating in the CVD reactor, these thin films disaggregate and small metal islands, often also referred to as "catalyst particles", are formed. Control over the particle size can be achieved through the adjustment of the layer thickness [60]. However, these routes have the drawback that the catalyst "particles" are formed *in-situ*, hence, they do not offer simultaneous control over the catalyst areal density and the catalyst size together with a narrow diameter distribution. In some cases the catalyst films are pre-patterned to enhance positional control, e.g. by photolithographic patterning [61; 62].

Recently, there has been a development from catalyst thin films towards readily prepared catalyst particles in order to gain more control over the CNT properties, viz. their size and their density. These isolated catalysts have so far mainly been prepared by chemical methods, such as decomposition or chemical reaction of metal precursors [63; 64], or micellar approaches [65–67]. In addition, metal-containing molecular nanoclusters or proteins have been widely used [68–70]. An alternative synthesis route is the preparation of isolated catalyst particles via gas-phase based methods. Such routes are attractive in that they allow for the synthesis of individual monodisperse particles and they do not require a series of chemical steps and thus inherently yield nanoparticles with a high degree of purity. Sato et al. have shown that nanoparticles prepared by laser ablation and classified with a differential mobility analyzer allow the synthesis of CNT with controlled diameters [71]. All these approaches demonstrate the importance of controlled catalyst preparation in CVD.

The aim of the present investigations is the synthesis of pre-defined catalyst particles via inert gas condensation using a DC magnetron sputtering setup. This approach is highly promising for the preparation of individual catalyst particles for diameter and density controlled CNT synthesis, since it enables simultaneous control of the catalyst diameter and density [72–74]. Details about the experimental work and the results are presented in chapters 3.1, 3.2 and 4, respectively.

In thermally activated CVD routes, a vertical CNT alignment relies on the density of the growing CNT, which results in a "crowding effect". As the nanotubes grow, their outer shells interact with the neighboring nanotubes by van der Waals interactions [61]. The CNT form rigid bundles which are stiff enough to keep growing along the primary direction away from the substrate. Yet, isolated growth of aligned CNT via this method is not possible. The possibility to align individual CNT is inherently provided by plasma-enhanced CVD (PE-CVD), where a strong electric field generates a plasma directly above the CVD substrate and the growing CNT follow the field lines [15]. Further, this method is known to yield CNT with catalyst particles residing at the CNT tips [15; 53]. It is therefore highly appealing for the tip-functionalization of CNT. In the present work, PE-CVD was applied for the synthesis of hard-magnetically terminated CNT as will be reported in chapter 5.2.

Despite the large variety of available CNT fabrication techniques many applications in nanoelectronics demand selective control of their electronic properties, that strongly depend on the angle at which the graphene strip is rolled up to form a single-wall CNT. Many groups concentrate on post-synthesis separation of metallic and semiconducting CNT via dielectrophoresis, density differentiation or ultracentrifugation [75–77]. Also covalent functionalization of CNT, e.g. via substitution of carbon atoms by boron or nitrogen atoms leads to a modification of the electronic properties [78]. However, direct synthesis of SWCNT samples that exclusively contain metallic *or* semiconducting nanotubes has so far not been successful. This is in part due to a lack of understanding of the CNT growth mechanisms. Some existing growth concepts are therefore discussed in the following section.

2.2.3 Growth models

Although carbon nanotubes have been extensively investigated over almost two decades, the basic understanding of the growth mechanism(s) involved is still a topic of controversy. In the cases of arc discharge and laser ablation, CNT are obtained from the condensate of a hot carbon gas. In CVD processes, the growth of CNT is stimulated by the presence of a catalyst, usually a transition metal such as Fe, Co or Ni. Carbon species are formed as a consequence of the catalytic dehydrogenation of the hydrocarbon precursor at the catalyst surface. CNT growth is generally assumed to occur via carbon dissolution into metal nanoparticles and subsequent carbon precipitation from the saturated metal particle leading to the formation of tubular sp^2-hybridized carbon solids [19]. Tube formation is preferred over other forms of carbon such as graphitic sheets with open edges, since tubes contain no dangling bonds and therefore constitute a low energy state.

Vapor-Liquid-Solid model

The commonly accepted growth mechanism, i.e. carbon dissolution and subsequent precipitation of excess carbon to form CNT or carbon nanofibers (CNF), originates from the so-called vapor-liquid-solid (VLS) model which was introduced by Baker et al. in 1972 for the growth of filamentous carbon in a CVD process [79]. Similar to present-day CNT synthesis via CVD, the Baker experiment involved deposition of a nanometer thick nickel film on a silicon substrate and its exposure to acetylene (C_2H_2). Nickel thin film disintegration occurred at $552°C$ to form particles with diameters of approx. 30 nm. Growth of filamentous carbon was first observed at $600°C$. *In-situ* characterization with electron microscopy allowed for the development of a growth model. The catalyst particles were generally observed to remain at the filament tip with a diameter matching the diameter of the filament. After a certain time of exposure to C_2H_2 the catalyst particles ceased to grow filaments and were seen to be encapsulated with carbon. In the literature this is often referred to as "catalyst poisoning".

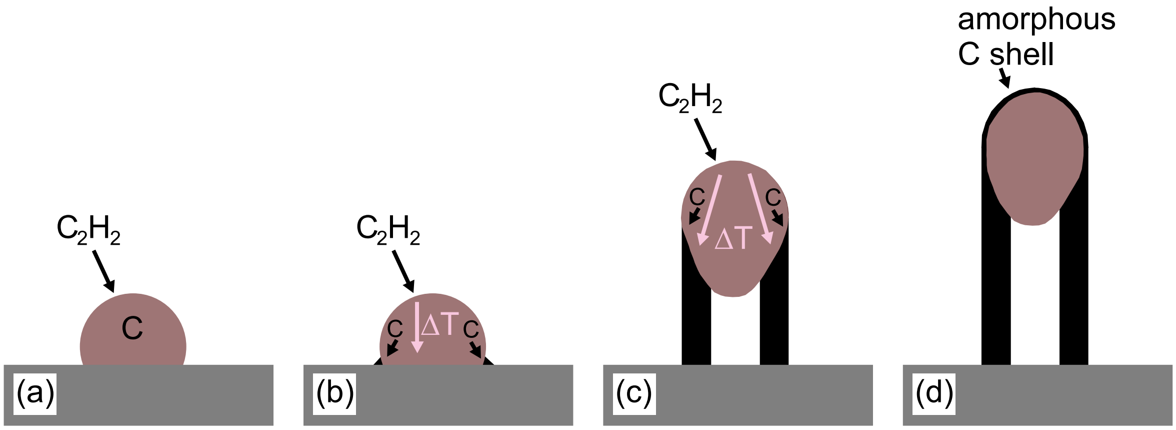

Figure 2.7: CNT growth mechanism: Scheme of the vapor-liquid-solid model.

A schematic illustration of the VLS model developed on the basis of these experimental findings is presented in Figure 2.7. The catalyst forms a liquid droplet (Fig. 2.7 a). The carbon containing *gas* is decomposed at the exposed catalyst surface and (partially) dissolved in the *liquid* catalyst. Acetylene decomposition on the nickel surface results in the release of a considerable amount of heat, equal to $-\Delta H_f(C_2H_2)$ for C_2H_2 decomposition[1] + ΔH_{sol} for carbon dissolution in nickel[2] [79]. This additional heating of the catalyst leads to the development of a thermal gradient between the exposed particle surface and the particle-substrate interface. As a consequence the dissolved carbon diffuses towards the substrate and is subsequently precipitated as a *solid* (Fig. 2.7 b). Since carbon precipitation is an endothermic reaction (cf. $\Delta H_{prec} = -\Delta H_{sol}$ = 40.5 kJ/mol), the temperature gradient becomes even larger, and the regions where precipitation occurs will be at the lowest temperature [79]. Therefore, excess carbon at the particle surface diffuses towards the particle-carbon fiber interface and is consumed there for carbon fiber growth (Fig. 2.7 c). The rate determining step of this model is the diffusion of carbon in the liquid catalyst. The carbon fiber growth rate remains constant as long as the heat input from C_2H_2 decomposition is balanced by losses due to heat radiation etc.. However, if the excess carbon at the particle surface does not reach the

---

[1] $\Delta H_f(C_2H_2)$ = 223.6 kJ/mol ... enthalpy of formation for C_2H_2

[2] ΔH_{sol} = - 40.5 kJ/mol ... enthalpy of solution

carbon fiber growth zone fast enough, the free particle surface available for adsorption and decomposition is reduced which in turn leads to a decrease in the heat input and subsequently to a decrease in the carbon diffusion rate. Therefore a reduction of the growth rate is observed, until the particle is finally encapsulated with carbon (Fig. 2.7 d) and fiber growth ceases.

The VLS model requires a catalyst particle in the liquid state which decomposes the gaseous carbon source and allows for the diffusion and precipitation of carbon to form a filament. However, examples of CNT growth have been reported, where *no* catalyst is needed [80; 81]. Also, the VLS model cannot explain CNT growth at temperatures as low as $350°C$ where the catalyst particle - even under consideration of a size-related reduction of the melting temperature - should be in the solid phase [82; 83]. Hofmann et al. introduced the so called vapor-solid (VS) model in order to explain the observation of CNT growth below the melting point of the catalyst material [84].

Vapor-Solid model

The vapor-solid (VS) model by Hofmann et al. suggests that the catalyst can be in the solid state during CNF or CNT growth [84] which is also its most essential difference as compared to the standard VLS-model. In Figure 2.8 the fundamental processes during CNT or CNF growth are sketched, i.e. (1) adsorption of the carbon source at the catalyst surface, (2) dissociation of the carbon source, (3) diffusion of the growth species, and (4) nucleation and growth of a CNT or CNF through carbon precipitation.

For the development of their model, Hofmann et al. compare CVD experiments with thermal and plasma activation and derive the corresponding activation energy for CNF growth from an analysis of the different growth rates [84]. From experiments using PE-CVD at low reaction temperatures ($150\,°C$ - $500\,°C$) they determined the activation energies to be below 0.4 eV, while for thermal CVD, the activation energy reached approximately 1.2 eV. Determining and analyzing the energy barriers for the four sequential reaction steps (cf. Fig. 2.8), they then derived the growth rate determining step. The

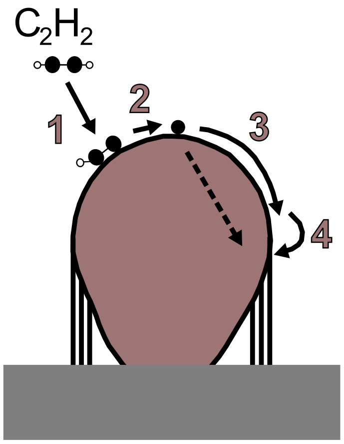

Figure 2.8: CNT growth mechanism: Scheme of the vapor-solid model: 1) Adsorption of the carbon precursor, 2) precursor dissociation, 3) carbon transport, 4) carbon incorporation at the CNT growth zone.

energy barrier for carbon incorporation is low, since no covalent bonds are broken. In the VLS model by Baker et al. the rate determining step is carbon diffusion [79]. Hence the activation barrier for PE-CVD and thermal CVD would have to be comparable, which is not observed in this experiment. From *ab initio* density functional calculations, Hofmann et al. find the energy barrier for the C_2H_2 dissociation on a stepped Ni (111) surface to be at least 1.3 eV. For comparison, the dissociation energy for C_2H_2 without a catalyst particle is 5.58 eV, highlighting the influence of the catalyst. The dissociation energy barrier of 1.3 eV agrees well with the activation energy value of 1.2 eV as determined from the thermal CVD experiments, however, does not explain the low activation energy of $< 0{,}4$ eV as determined from the PE-CVD experiments. Hofmann et al. argue that in PE-CVD the plasma creates highly reactive species, such as radicals, in the gas phase and/or on the catalyst surface, which e.g. allows for direct chemisorption of atomic carbon at the catalyst surface, i.e. an effective reduction of the adsorption energy. From their *ab initio* calculations they further observe an activation barrier of 0.4 eV for carbon diffusion on the Ni (111) surface and 0.5 eV on the Co (111) surface, which is in good agreement with the experimental values from PE-CVD. Therefore they conclude that carbon transport takes place through surface diffusion towards the growth zone only and that surface diffusion is the rate determining step. As mentioned above, the essential novelty of the VS-model is that the catalyst does not have to be in the liquid phase. Thus the model explains the observation of CNT growth at low temperatures.

However, *in-situ* CNT growth experiments by the same group [85] and by Helveg et al. [86] using a transmission electron microscope with an environmental cell reveal the catalyst particles to behave "liquid-like", which in this context denotes that the catalyst shows fast dynamic reshaping, while lattice fringes can still be observed indicating long range crystalline order. Clearly, this still leaves key questions open, such as how the nanotubes nucleate and whether the catalyst is liquid or solid.

Limitations of the existing models

As pointed out in the previous paragraphs, it is generally assumed that a transition metal catalyst particle has multiple purposes during CVD synthesis of CNT, namely the catalytic decomposition of the carbon source, the nucleation, *and* the growth of the CNT. However, there is an increasing number of studies which show that this picture is incomplete in that CNT can be synthesized without metal catalysts or even without catalyst particles [87–91]. Further, recent studies show that novel metallic catalysts, including noble metals, can act as catalyst in CNT growth [45; 92–94]. Unlike the typical transition metal catalyst elements from the "iron-family", the solubility of carbon in, e.g., gold is extremely low in the bulk phase thereby questioning carbon dissolution mechanisms. Recently, however, the solubility of carbon in nanosized gold particles during CNT growth was reported [95]. Also, CNT growth from non-metal catalysts was demonstrated [87–91]. Interestingly, in many cases, oxygen seems to play a key role in the catalyst activation as is known for CNT synthesis using laser ablation [45; 92]. Further, a "catalyst-free" CNT synthesis was reported using porous Al_2O_3 templates [96; 97].

These findings suggest that the role of the catalyst particle may not be as multi-faceted as was previously suggested. Clearly, the argument that catalyst particles in

CVD are mandatory to decompose the hydrocarbon is redundant. In addition, it is known that oxides typically used as catalyst supports in CNT-based CVD synthesis can themselves form graphitic carbon layers and thus provide an interface for ordered sp^2-hybridized carbon formation [98]. Thus, the argument that the catalyst particles provide the interface for the graphitic carbon formation is not a prerequisite and the simplistic view of the support playing a catalytically passive role should be revisited. Henceforth, the role of the catalyst particle in CNT synthesis is addressed in investigations presented in chapter 4.2.

CNT growth modes in substrate based CVD

Two alternative CNT growth modes are described for substrate-based CVD techniques. While in the so-called tip-growth mode, carbon is incorporated in the CNT tip, in the base-growth mode, carbon addition occurs at the CNT support [27].

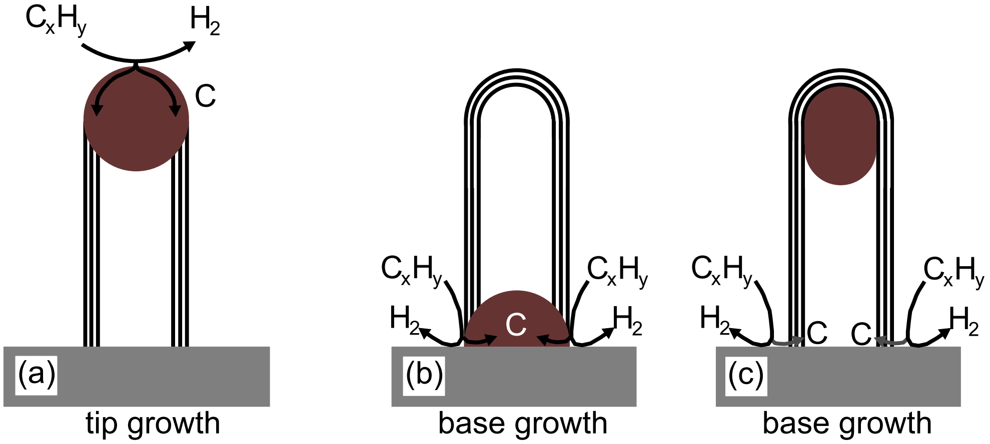

Figure 2.9: Schematic illustration of the CNT growth modes in substrate-based CVD. a) Tip growth. b, c) Base growth.

Figure 2.9 schematically illustrates the different CNT growth modes. In case of the tip-growth mode, as for example in plasma-enhanced CVD, the catalyst particle generally terminates the CNT tip. Some catalyst materials also might remain within the CNT as the growth progresses. The picture is more diverse for the base-growth mode. Depending on the strength of the catalyst-substrate interaction, the catalyst particle may remain at the substrate (Fig. 2.9 b) or be lifted off the substrate (Fig. 2.9 c). In the latter case, carbon incorporation at the CNT base may result from spill-over reactions via the oxide support. Here, the substrate acts as catalyst for the decomposition of the carbon feedstock [98; 99]. Thus, the variation of catalyst and/or substrate material may be utilized to tailor the CNT product. For the fabrication of hard-magnetically terminated CNT the growth modes depicted in Figures 2.9 a and 2.9 c are desired (cf. chapter 5).

2.3 Catalytic hydrogenation of graphite

Catalytic hydrogenation of graphite can be considered the reverse of catalytic CNT growth. Both processes involve metal catalyst particles, (graphitic) carbon and hydrogen as reaction partners with the reactant(s) and product(s) swapped. While graphitic carbon is formed via decomposition of a hydrocarbon, carbon dissolution in a catalyst particle and its precipitation in a sp^2-hybridized state in the CNT growth process, catalytic hydrogenation represents the decomposition (etching) of graphitic carbon in hydrogen atmosphere forming a hydrocarbon (CH_4) as reaction product. The latter basically involves the dispersion of metallic nanoparticles on graphite and their subsequent exposure to hydrogen at elevated temperatures. The catalyst helps to dissociate molecular hydrogen which then reacts with carbon from an exposed graphite edge to form methane via the following reaction:

$$C(s) + 2H_2(g) \longrightarrow CH_4(g). \tag{2.11}$$

It is well known that methane is the only reaction product from the hydrogenation reaction [22; 100]. Further, while in catalytic CNT growth the concentration of H_2 formed during the reaction is negligible as compared to the concentration of the hydrocarbon, it is the concentration of the formed CH_4 that can be neglected in catalytic hydrogenation as compared to the H_2 present during the reaction. Yet, recent studies by Campos et al. reveal that CNT may be synthesized during a catalytic hydrogenation experiment [26].

The catalytic hydrogenation leads to the catalyst "eating up" the graphite it is in contact with leaving pronounced etch tracks behind. Inherent to the process is a significant anisotropy of the etching which predominantly occurs along specific crystallographic directions. This anisotropy has recently stimulated a strong interest in catalytic hydrogenation as it is considered a promising engineering tool in graphene nanoribbon fabrication [24–26][3]. During the etching process the nanoparticle acts as a knife to cut channels through the graphene layers. As the nanoparticle erodes the graphite sheet, it moves while maintaining maximum surface contact with the graphite step edge as this is energetically favored [100]. This re-shapes the etching particles into typical "half-moon"-type morphologies.

Etching of graphite by various metal and oxide particles has also been observed in oxygen [101–104], carbon dioxide [104; 105], water [104; 105], nitrous oxide [106], and hydrogen [22; 23; 100; 107–111]. Depending on the etching conditions, different catalytic activities such as, e.g., the formation of etch channels or etch pits, were observed. Although catalytic hydrogenation reactions have been investigated for a long time, the hydrogenation mechanism itself remains controversial [25]. Two primary hydrogenation mechanisms are proposed. One is the so-called interfacial hydrogen mechanism [23; 101]. Here, it is argued that the catalytic gasification of carbon occurs via a two-step procedure. Firstly, molecular H_2 is dissociated on the metal particle surface. The atomic hydrogen then migrates on or through the catalyst to the leading graphite-catalyst interface where it reacts to CH_4. The rate determining step is argued to be the chemisorption/dissociation of hydrogen [23; 101]. An alternative proposal is the carbon dissolution mechanism which suggests that at the graphite-catalyst interface, carbon atoms dissolve

---

[3] The gapless band structure of two-dimensional graphene makes it unsuitable for direct use in graphene-based field effect transistors. Integration of graphene into semiconducting nanoelectronics therefore necessitates the fabrication of graphene nanoribbons whose lateral confinement results in the opening of a band gap.

into the catalyst. The dissolved carbon then diffuses towards the catalyst surface where it reacts with hydrogen to form CH_4 [23; 109–111]. This methane forming surface reaction is proposed as the rate determining step [23]. The interfacial hydrogen mechanism is usually favored [100], however, recent work related to the controlled cutting of few layer graphene provides support for the carbon dissolution argument [25].

The catalytic hydrogenation utilizing cobalt nanoparticles has been investigated as one part of the present thesis. Detailed studies using aberration-corrected high-resolution transmission electron microscopy are conducted to investigate the structural properties of this process, viz. to resolve the atomic structure of the graphite and the catalyst particles to elucidate the etching process. The respective results will be discussed in chapter 4.3.

2.4 The Fe-Pt system

A main objective of the present study is to hard-magnetically functionalize CNT at their tip. FePt is thus choosen as catalyst, since it offers a large magneto-crystalline anisotropy in the chemically ordered tetragonal $L1_0$ phase [28]. FePt has a high application potential, e.g. in ultrahigh-density recording media as well as for biological separation [112–115]. Figure 2.10 shows the phase diagram of the Fe-Pt system.

The alloy constituents are fully miscible in the liquid and in the solid phase, respectively. Alloys with concentrations close to the equiatomic composition exhibit a disorder-order transformation from the face centered cubic $A1$ phase (γ(Fe,Pt), cf. Fig. 2.11 a) to the $L1_0$ tetragonal phase (γ_2(Fe,Pt), cf. Fig. 2.11 b) upon cooling. The stability region of the magnetically interesting $L1_0$ phase which is the thermodynamically stable structure at room temperature ranges from 35 to 55 at. % Pt at 600°C. The primitive unit cell of the $L1_0$ structure has the space group P4/mmm [117] and is composed of alternating layers of Fe and Pt along the [001] direction (Fig. 2.11 b). The ratio of the c-axis (along [001]) and the a-axis (along [100] or [010]) ranges from $0.96 \leq c/a \leq 0.98$

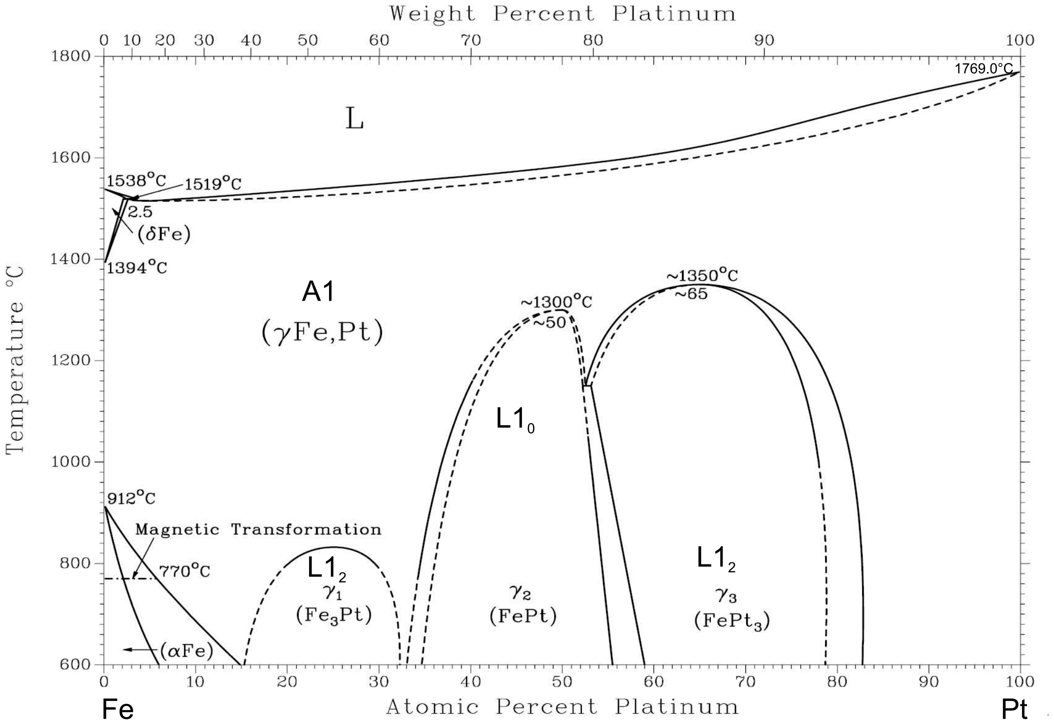

Figure 2.10: Equilibrium phase diagram of the Fe-Pt system [116].

in ordered FePt [118–120]. The strong spin-orbit coupling of the heavy Pt atoms in the tetragonally distorted $L1_0$ structure gives rise to the high magnetocrystalline anisotropy of this alloy [121]. In the (soft-magnetic) disordered $A1$ phase, the magneto-crystalline anisotropy constant is $K_U = 1.1 \cdot 10^5$ J/m^3, while in the ordered $L1_0$ phase, it reaches $K_U = 6.6 - 10 \cdot 10^6$ J/m^3 [28]. The easy axis of magnetization in the $L1_0$ phase points along the c-axis.

The bulk thermodynamic ordering temperature of the stoichiometric composition $Fe_{50}Pt_{50}$ is approx. 1300°C. In nanoparticles it can be significantly reduced. For particle sizes smaller than 5 nm, the equilibrium ordering temperature is known to decrease with decreasing particle size [122; 123]. Volume diffusion is a prerequisite for ordering of the atoms. Therefore the creation and healing of vacancies is crucial for the disorder-order transition which occurs via nucleation and growth of ordered domains with a defined phase boundary until the disordered regions are consumed (first order phase transition)

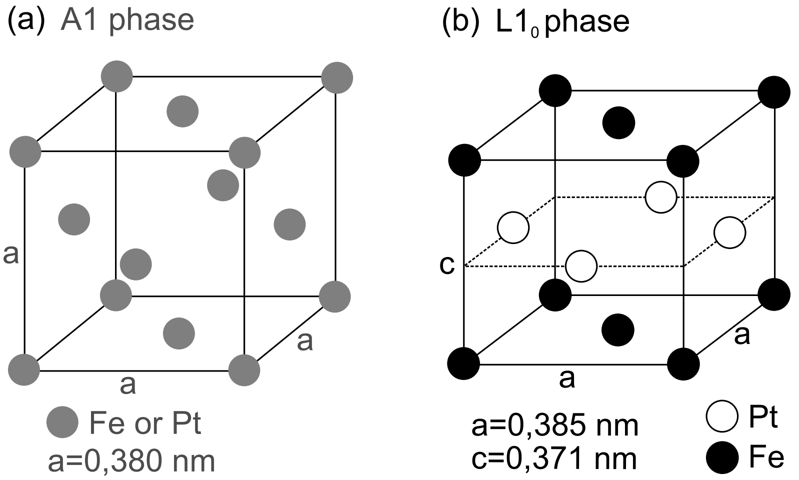

Figure 2.11: Schematic illustration of the unit cell of a) the disordered $A1$ phase and b) the chemically ordered $L1_0$ phase.

[124]. The domains are separated by anti-phase boundaries. Subsequently, the domains grow further to minimize the area of the anti-phase boundaries [125].

However, the metastable disordered $A1$ phase can be stabilized at room temperature by rapid quenching. As a consequence, the formation of the $L1_0$ structure may be kinetically hindered, as often observed in thin film deposition. Also, as-prepared FePt nanoparticles from wet-chemical or gas-phase preparation are usually found in the chemically disordered $A1$ structure. Additional thermal treatment steps are required to transfer them into the hard-magnetic $L1_0$ phase [112; 113; 126–128].

3 Experimental details

The following chapter introduces the experimental procedures and methods used within this study. The first step is the provision of the catalyst material. Gas-phase prepared nanoparticles have primarily been used as catalyst for the CNT synthesis. Thus, the preparation of nanoparticles via inert gas condensation is introduced. This section is followed by a detailed description of the two chemical vapor deposition (CVD) techniques used, namely the thermally activated CVD and the plasma-enhanced CVD. Further, the major methods for sample characterization, i.e. scanning and transmission electron microscopy (SEM, TEM), Raman spectroscopy and vibrating sample magnetometry (VSM), are briefly introduced.

3.1 Preparation of catalyst particles from the gas phase

The catalyst nanoparticles are synthesized from a Haberland-type gas aggregation source [129]. Figure 3.1 shows the schematic illustration of the nanoparticle deposition system of the type *Nanodep 60* (*Oxford Applied Research Ltd.*) which basically consists of a nucleation chamber and a deposition chamber. Optionally, a quadrupole mass filter can be inserted between these two modules for in-flight particle size sizing and size fractionation. An inert sputtering gas (Argon or Helium) is fed into the nucleation chamber and is ionized due to a bias voltage applied between the anode and the target which serves as the cathode. Due to their positive charge the inert gas ions are accelerated towards the target and metal atoms and ions are sputtered from it. To optimize the sputtering yield, an annular permanent magnet is placed behind the target whose stray fields direct the ionized gas onto spiral trajectories thereby increasing the ion concentration via secondary ionization. The nanoparticles nucleate from a supersaturated metal vapor and grow through coagulation and coalescence [130]. After growth of the particles in an adjustable aggregation volume, they are ejected through a double aperture system into high vacuum (10^{-5} mbar $\leq$ p $\leq$ 10^{-4} mbar). As a consequence and in contrast to other gas phase techniques, further agglomeration of the particles is hereby suppressed [113]. In the deposition chamber, the particles are then deposited onto appropriate substrates for the CVD processing, preferentially onto thermally oxidized silicon substrates coated with a 10 nm thick layer of Al_2O_3. For transmission electron microscopy (TEM) analysis, particles are simultaneously deposited onto carbon-coated copper grids (referred to as TEM witness plates) mounted on the sample holder next to the CVD substrates.

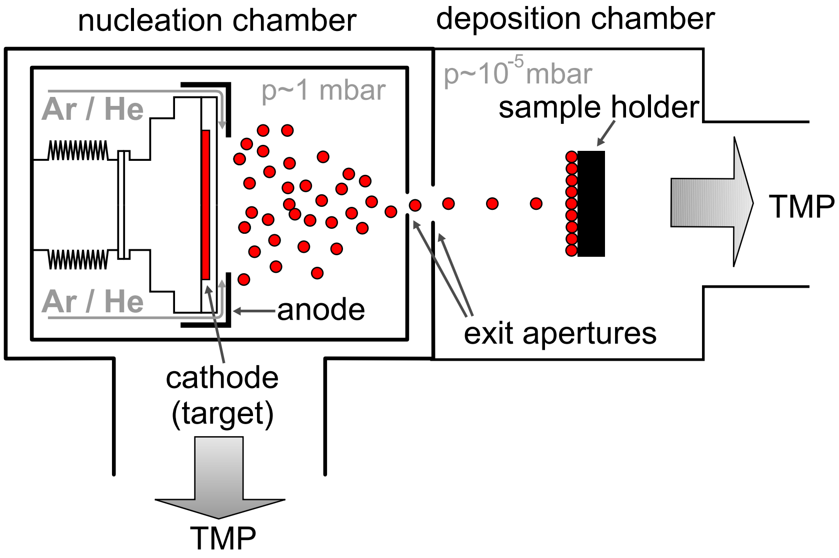

Figure 3.1: Setup of the nanoparticle deposition system *Nanodep60* (*Oxford Applied Research Ltd.*) consisting of a nucleation and a deposition chamber.

The gas-phase preparation route allows for the synthesis of very pure catalyst particles with a well defined size distribution. The mean particle size can be controlled by varying the sputtering power, the gas pressure, and/or the gas mixture [73; 131]. Different deposition times lead to different nanoparticle densities on the substrates. Since the metal target can be easily exchanged, the preparation of different metal and alloy particles is feasible. During this work, elemental iron and cobalt as well as FePt alloy targets have been exploited for nanoparticle preparation. Since the target composition is directly transferred to the growing particles, the composition of the used FePt is 50 at.-% iron and 50 at.-% platinum in order to obtain stoichiometric FePt nanoparticles [132]. Unlike in the use of thin film catalysts, the gas-phase-based approach also allows for the characterization of the particles (on witness plates) *prior* to the CVD processing, which cannot be easily achieved in routines where the catalyst particles form *in-situ*.

3.2 CNT synthesis via substrate based chemical vapor deposition

3.2.1 Thermally activated CVD

In this work a substrate-based thermally activated CVD technique is applied for the CNT synthesis from conventional (Fe, Co) and hard magnetic (FePt) catalyst materials. The predefined gas-phase prepared nanoparticles are primarily deposited onto thermally oxidized silicon substrates coated with a 10 nm thick Al_2O_3 layer. For studies investigating the effect of different CVD supports, also TiN and graphite substrates are used. Experiments utilizing Fe nanoparticles as catalyst are performed in a purpose-built vertical high vacuum CVD system, consisting of a sealable elevator-like transfer stage and a 2 cm wide quartz tube tightly fitting into a hollow SiC heating rod as illustrated in Figure 3.2 a. The substrate is mounted on a vertical vacuum-compatible transfer stage on top of the reactor. Further, a horizontal CVD setup has been designed and constructed in cooperation with M. H. Rümmeli (IFW) and C. Schünemann (IFW) and is schematically illustrated in Figure 3.2 b. This setup is used for experiments with predefined Co and FePt nanoparticles. Here, the CVD substrate is placed in a horizontal quartz tube (inner diameter 9 mm, length 70 cm) which fits into a movable tube furnace with a length of 25 cm.

The experimental routine is similar for both setups. Before the experiments, the whole system is evacuated to a base pressure of $1{\cdot}10^{-5}$ mbar. This provides well defined starting conditions. During any transfer of a particle sample from the nanoparticle

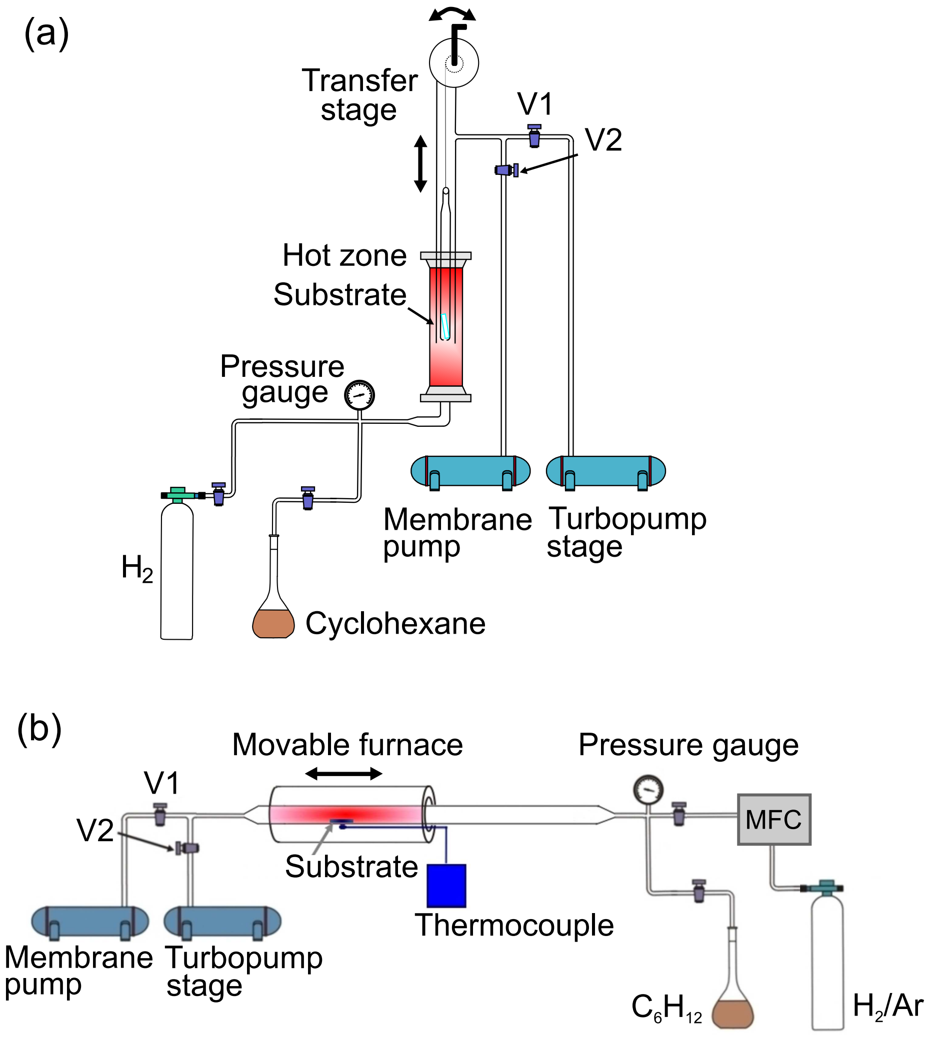

Figure 3.2: Setups for thermally activated CVD: a) vertical and b) horizontal assembly.

deposition system into the CVD reactor, the particles are exposed to ambient air and thus oxidized. Therefore, the CVD system is firstly flooded with hydrogen. Once the hydrogen pressure p_{H_2} is constant, the sample is transferred into the hot zone. In case of the vertical CVD setup, the elevator-like stage is lowered into the reaction zone, whereas in the horizontal setup, the furnace rod is simply moved over the sample. The H_2 gas provides excellent thermal conductivity and reduces any surface oxide that may have formed on the catalyst particles. After a certain hydrogen treatment time, t_{H_2}, the system is re-evacuated within 1 min to typically $1{\cdot}10^{-4}$ mbar. The carbon feedstock is then provided by gently flooding the system with cyclohexane vapor ($p_{C_6H_{12}}, t_{C_6H_{12}}$). Cyclohexane is an aromatic hydrocarbon with a high standard vapor pressure of 130 mbar which is known to yield CNT material which does not require any further purification [133]. The vapor is then removed by pumping the system again. At the same time, the sample is quickly withdrawn from the hot zone to bring the reaction to a rapid stop. In the vertical CVD reactor, the CVD process temperature, T_{CVD}, is checked before and after every experiment with a thermocouple placed at the resting position of the sample in the hot zone. In the horizontal setup, the process temperature can be controlled at all times using a thermocouple that is placed between the sample rod and the movable furnace rod (cf. Figure 3.2 b). For every CVD system and every catalyst material the synthesis parameters are optimized to obtain clean CNT material with a high yield. Table 3.1 summarizes the CNT synthesis parameters applied for the different catalyst materials.

Table 3.1: Process parameters for the CNT synthesis with thermal CVD

	p_{H_2}(mbar)	$t_{H_2}(min)$	$p_{C_6H_{12}}$(mbar)	$t_{C_6H_{12}}(min)$	$T_{CVD}(^\circ C)$
Fe	20	4	60	5	800
Co	60	5	50	5	750
FePt	60	3	50	5	590-830

3.2.2 Plasma enhanced chemical vapor deposition

Among various CVD methods plasma enhanced CVD (PE-CVD) has received considerable attention because it can provide vertically well aligned CNT at relatively low temperatures with high purity and yield [15]. In contrast to thermally activated CVD, the plasma creates reactive species, such as radicals, in the gas phase and/or on the catalyst surface which allows for a reduction of the activation energy for CNT growth.

PE-CVD is further a method known to yield CNT with the catalyst particle at the tip [15; 53].

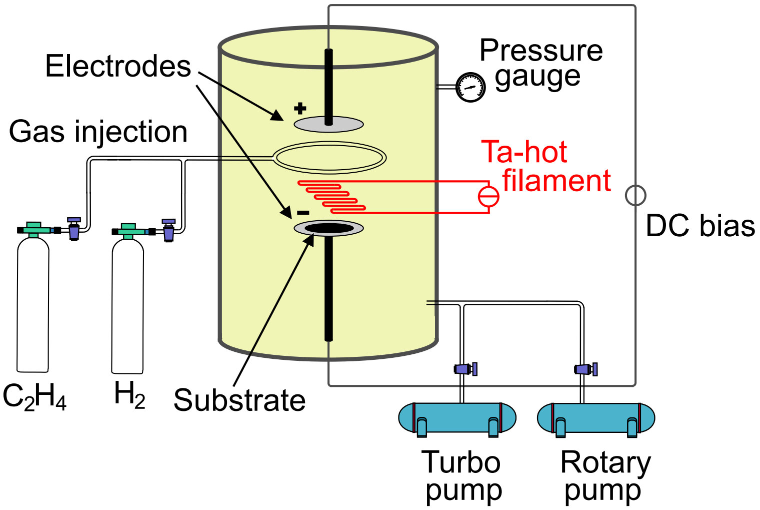

Figure 3.3: Setup for plasma enhanced CVD.

Figure 3.3 illustrates the direct current PE-CVD reactor utilized during this study. It is equipped with a tantalum hot filament positioned 1.5 cm above the substrate electrode. Before the experiments, the system is evacuated to a base pressure of $1 \cdot 10^{-5}$ mbar to provide clean starting conditions. The samples are then subjected to an initial thermal treatment for 5 min at 700°C under a constant flow of Ar (500 sccm) which is followed by a H_2 plasma pre-treatment (25 mA, 242 V, 500 sccm) at 900°C - 950°C for 2 min with additional heating from the Ta hot filament. DC power is applied between the substrate electrode and an upper electrode. After the plasma pre-treatment, 5 sccm of C_2H_4 are added as carbon source to the H_2 background gas flow in the reactor and the discharge is run at a DC current of 500 mA (481 V). CNT are grown for 30 min. The pressure is kept constant at $p = 10$ mbar during the whole experiment. Gas-phase prepared and wet-chemically prepared FePt nanoparticles as well as Fe-Pt multilayer thin films are used as catalysts. The FePt nanoparticles are provided by M. Dudek (IFW) and prepared following the preparational recipe of Sun et al. [112]. For the CNT synthesis these wet-chemically prepared nanoparticles are spin coated onto thermally oxidized silicon substrates. The Fe-Pt multilayer thin films are obtained from the IFW thin film group (R. Kaltofen) and deposited onto thermally oxidized silicon substrates by means of DC sputtering at a pressure of $1{\cdot}10^{-3}$ mbar and a power of 20 W in Ar. In order to magnetically functionalize the CNT at their tip, the PE-CVD conditions are optimized towards the growth of well aligned CNT with the magnetic catalyst particle residing at the tip of each CNT.

3.3 Catalytic hydrogenation of graphite

In order to investigate the catalytic hydrogenation of graphite, monodisperse gas-phase prepared cobalt nanoparticles with a mean diameter of $d_P = 5\,\mathrm{nm}$ are utilized as catalyst. Research grade polycrystalline graphite blocks (*Goodfellow*, 99.95% purity) are sectioned into 5 mm × 5 mm × 1 mm pieces and used as particle support. After the deposition of the catalyst particles these substrates are placed in a horizontal CVD reactor (cf. Figure 3.2 b) which is then evacuated to a pressure of $2{\cdot}10^{-5}$ mbar. Initially, the reactor furnace is pre-heated to the desired reaction temperature (400°C - 900°C), and the reactor is flooded with 60 mbar of hydrogen. Only then is the furnace positioned over the graphite substrate which adopts the preset temperature within approx. 30 s. Dynamic H_2 treatments are carried out at continuous H_2 flows of 40 sccm for either 5 min or 30 min. The generated CH_4 vapor and the hydrogen are then rapidly evacuated from the system, the oven is moved away from the reaction zone, and water is flushed over the reaction zone of the quartz tube to provide a well-defined and rapid stop of the reaction. In some cases additional heat treatments in vacuum are carried out for 5 min .

3.4 Characterization methods

In the following chapter, the methods applied for morphological and structural characterization of the catalyst material as well as of the produced or modified carbon nanomaterials are briefly introduced.

3.4.1 Electron microscopy

Transmission electron microscopy

In transmission electron microscopy (TEM), the wave nature of electrons is exploited to examine nanostructures at the atomistic level. Briefly, in a TEM electrons are emitted from an electron gun by thermionic or field emission under ultra-high vacuum conditions, injected into the microscope column by virtue of accelerating voltages between 80 and 300 kV, and directed through a double or triple electromagnetic condenser lense system to illuminate the specimen. When the electrons pass the sample, they are scattered by the electrostatic potentials of the atoms within the sample. After passing the object the electron beam is focussed in the first intermediate image plane by the lower objective lense. The following projector lense system magnifies the image (or the diffraction pattern) onto a fluorescent viewing screen. A digital image can then be collected using a CCD camera.

Depending on the structure of the nanometer thin sample, amplitude and phase of the incoming plane electron wave are modified. Image contrast arises from incoherent electron scattering as well as from (coherent) electron diffraction. The electrons are scattered under specific angles, depending on the sample thickness and the atomic number, and thus fail to reach the viewing screen or CCD camera. Additional diffraction contrast arises from coherent superposition of scattered waves in a crystalline sample. Here, sample areas which fulfill Bragg's law scatter the electrons stronger and thus appear darker. In high resolution transmission electron microscopy (HRTEM), an interference of the scattered and unscattered waves leads to the formation of an image of the crystal lattice. In conventional HRTEM, structures with lateral distances of 1-2 Å can be resolved.

Throughout this study, characterization of the as-prepared nanoparticles on witness plates as well as morphological analysis of the synthesized CNT (i.e. determination of CNT diameter and CNT number of walls) is carried out using a *FEI Tecnai G^2 20*

TEM equipped with a LaB_6 cathode operating at 200 kV as well as a *FEI Tecnai F30* HRTEM equipped with a field emission gun operating at 300 kV. Both microscopes are further equipped with an *EDAX* energy dispersive X-ray (EDX) spectroscopy system for analysis of the elemental composition of the samples.

In order to characterize the starting/catalyst material by means of TEM, the catalyst particles are deposited onto carbon coated copper grids (witness plates) that are mounted directly next to the CVD substrates during particle deposition. The CNT samples for the HRTEM investigation are prepared by gently sliding a standard copper TEM grid over the as-processed CVD sample.

New generation aberration corrected electron microscopes allow for delocalization-free imaging and reach sub-Å resolution. Further, the emergence of aberration corrected electron microscopes makes it possible to examine samples that are sensitive to knock-on damage (i.e. graphite) at a lower acceleration voltage where knock-on damage is significantly reduced at a still very high resolution. Therefore, this method is of great advantage for the examination of carbon based nanomaterials.

A detailed structural and morphological characterization of the CNT, the nanoparticles at the CNT as well as of the etch tracks evolved from catalytic hydrogenation is achieved via aberration corrected low voltage high resolution transmission electron microscopy (LV-HRTEM). Within this study a *FEI Titan*^{3} *80-300* operating at 80 kV is employed. This state-of-the-art microscope is equipped with a field emission gun, a monochromator and an image C_S corrector to correct for spherical aberrations (C_S) in the imaging system.

Scanning electron microscopy

Scanning electron microscopy (SEM) is one of the most frequently used methods in sample characterization due to the combination of high magnification, large depth of focus, good resolution, and ease of applicability. Similar to a TEM, an electron beam is generated in ultra-high vacuum, accelerated by an anode cascade, and collimated by electromagnetic condenser lenses. The electron beam is then focussed to a small probe by the objective lense and scanned across the surface of the sample by electromagnetic deflection coils. The interaction of the primary electrons with the sample results in the generation of secondary electrons from the sample which are predominantly collected for image formation giving a three-dimensional impression of the sample's surface topography. In contrast to TEM, the resolution in a SEM is limited by the diameter of the electron probe and the probe's interaction volume within the sample. State-of-the-art SEM can resolve structural details with lateral distances in the sub-nm-regime.

Within this study, SEM is in particular used to investigate the arrangement and the alignment of the as-grown CNT networks on the CVD substrates complimenting the TEM analysis. The SEM micrographs presented in this thesis are obtained from a FEI Nova NanoSem and a Leo Gemini 1530 microscope. Both microscopes are equipped with field-emission guns and are operated at an accelerating voltage of 5 kV .

3.4.2 Raman spectroscopy

Raman spectroscopy is a method widely used to characterize CNT due to the ease with which bonding information of molecular nanostructures can be obtained in a non-invasive manner. Raman spectroscopy involves inelastic scattering of light in molecules. It is particularly sensitive to specific vibrational modes which are excited by a laser. Also, optical phonons, optical magnons or plasmon excitations can give rise to Raman scattering [134].

In this study, the CNT are analyzed with multifrequency resonant Raman spectroscopy directly after each CVD experiment in order to check, whether CNT have been successfully produced or not. The analyses are conducted on a *Bruker IFS100* Fourier Transform (FT) Raman spectrometer equipped with a Nd:YAG laser (1064 nm excitation). All spectra are recorded at ambient conditions. Raman spectroscopy is particularly suited to detect the presence of few-walled CNT and to provide information on the CNT yield, the diameter of SWCNT, and the CNT quality (i.e. the presence of defects).

3.4.3 Vibrating sample magnetometry

Magnetic characterization of the hard-magnetically terminated CNT grown via PE-CVD is carried out using vibrating sample magnetometry (VSM). This method is used to determine the magnetic properties as a function of an external magnetic field and of the temperature. The samples are placed and periodically moved within a homogeneous magnetic field. The temporal variation of the magnetic flux induces a voltage in the detection coil system that is proportional to the magnetic moment of the sample.

A *Quantum Design* PPMS vibrating sample magnetometer is used for the magnetic characterization. For VSM sample preparation, a CVD substrate with as-grown CNT is glued face down onto a VSM sample holder that is covered with scotch tape. The substrate is then lifted off the tape so that only CNT material remains on the tape for characterization. This reduces the complexity of the VSM signal correction, since there is no diamagnetic contribution of the substrate. Also, ferromagnetic signals of FePt material that may have remained on the CVD substrate during CNT growth can be excluded this way.

4 Carbon nanotube synthesis from conventional catalysts

In this chapter, the experimental results on the controlled CNT growth from conventional catalysts via thermal CVD are presented. On the whole, transition metals are utilized as catalysts. Here, CNT growth control is achieved using predefined gas-phase prepared Fe and Co nanoparticles deposited onto Al_2O_3-coated Si/SiO_2 supports. Conclusions will be drawn from the obtained results to further our understanding of CNT nucleation and growth mechanisms.

4.1 Controlled growth of carbon nanotubes

The gas phase route allows for the preparation of very clean and well defined individual catalyst particles with a narrow size distribution. Figure 4.1 a shows a typical TEM micrograph of as prepared pristine Fe catalyst particles. The particle size is determined by statistical analysis of over 200 particles from a series of TEM micrographs. A histogram representing the observed particle diameter distribution is shown in Figure 4.1 b. A median particle diameter d_P of 6.4 nm with a geometrical standard deviation σ_G of 1.2 (this corresponds to a standard deviation of $\sigma = 1.2$ nm in case of a Gaussian distribution) is derived from a fit of a log-normal distribution function to the experimental data. Figure 4.1 c shows a typical TEM overview of CNT grown from these particles which were gently lifted off the Al_2O_3-coated Si/SiO_2 substrate. Detailed HRTEM studies show that the obtained CNT are MWCNT with 4 to 12 walls. A statistical analysis of the TEM data reveals a log-normal distribution of the outer diameter for the CNT d_{CNT} with a median of 6.9 nm and a geometrical standard deviation σ_G of 1.2 (corresponding to a Gaussian $\sigma = 1.5$ nm). The good agreement between the catalyst diameters and the CNT diameters implies that the catalyst diameter templates the CNT diameter [72].

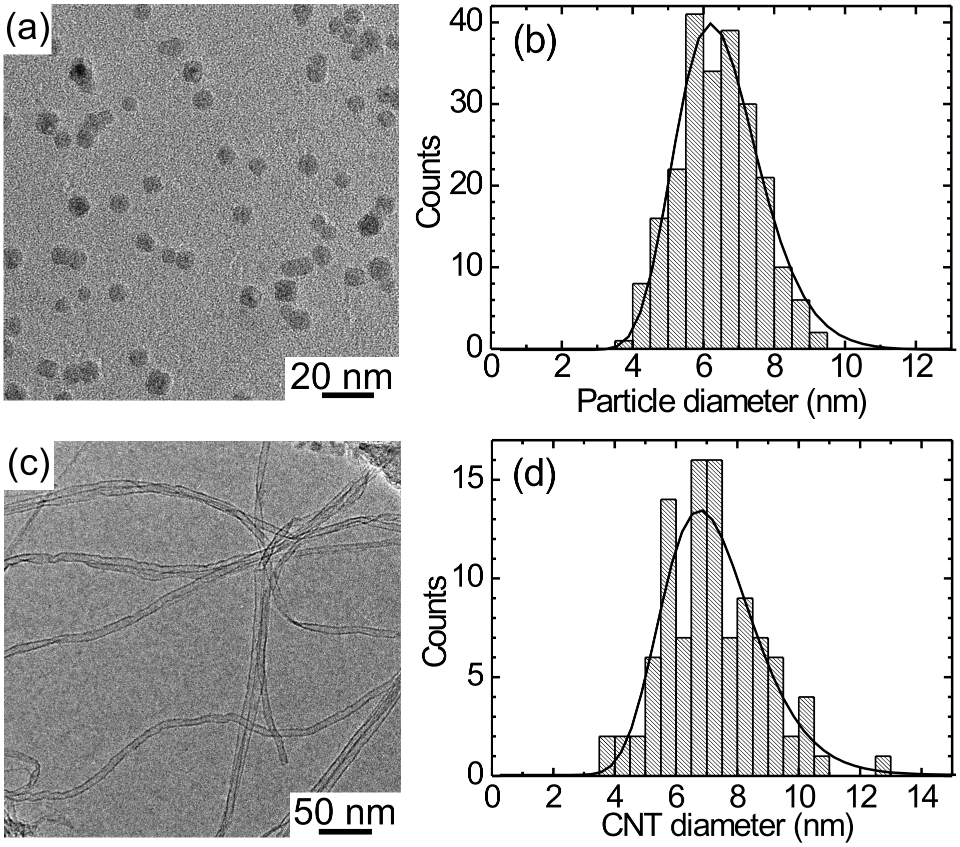

Figure 4.1: a) TEM micrograph of typical Fe catalyst particles as deposited onto witness plates. b) Corresponding particle diameter distribution and a lognormal fit obtained from statistical analysis of a set of TEM micrographs. The median particle diameter d_P is 6.4 nm. c) TEM overview of the CNT network as-grown from these particles. d) CNT diameter distribution with a median nanotube diameter d_{CNT} of 6.9 nm.

The separate generation of the catalyst particles holds the potential to independently vary both the catalyst size and density and facilitates their comprehensive characterization prior to the CVD process. This cannot be so conveniently accomplished in more conventional CVD methods using thin film catalysts where the catalyst particles form *in-situ* [42; 58]. Due to the ease with which detailed information on the catalysts' size distribution and dispersion can be accessed, the technique provides improved insight into the CVD process. In the present study, this is highlighted by a direct relationship between particle and CNT densities as well as between the sizes of the catalyst particles and of the resultant CNT diameters, respectively. Also, a clear link between the number of walls of the CNT and the catalyst size is established.

4.1.1 Density control

In a gas phase particle preparation process, the particle density on a CVD substrate can be easily adjusted by varying the deposition time. Figures 4.2 a-c show (oxidized) Fe nanoparticles deposited with different areal densities. Along with the particle density, the mean particle diameter is varied in these samples ($d_P = 5\,\text{nm}$, $d_P = 7\,\text{nm}$, $d_P = 10\,\text{nm}$ in Figures 4.2 a-c, respectively). These particles serve as individual catalytic nucleation sites for CNT growth in the subsequent CVD process. The corresponding SEM images (Figures 4.2 d-f) illustrate that low particle densities lead to isolated CNT (Figure 4.2 d) and medium particle densities result in a coverage of the CVD substrate with rather interwoven CNT (Figure 4.2 e), whereas high particle densities lead to the formation of dense CNT mats (Figure 4.2 f).

Figure 4.3 shows typical resonant FT Raman spectra of the as-produced CNT depicted in Figures 4.2 d-f. Raman lines originating from the silicon substrate (labelled "Si") and those originating from the CNT, namely, the graphite mode ("G"), the defect mode ("D"), and the radial breathing modes ("RBMs"), are visible. The G mode at around $1590\,\text{cm}^{-1}$ becomes apparent in sp^2 hybridized carbon systems, e.g. graphite or carbon nanotubes. In addition, at around $1300\,\text{cm}^{-1}$, the disorder induced D line is observed. This mode arises from second order Raman scattering at defects [135; 136]. Thus, the relative intensity ratio of the G to the D mode (I_G/I_D) is a measure of the quality of few-wall CNT. A unique feature of single- or double-wall CNT is the presence of RBMs between $160\,\text{cm}^{-1}$ and $350\,\text{cm}^{-1}$ in the Raman spectra. For a low particle density (and size), the Raman spectrum (Figure 4.3 a) shows a very weak CNT signal as compared

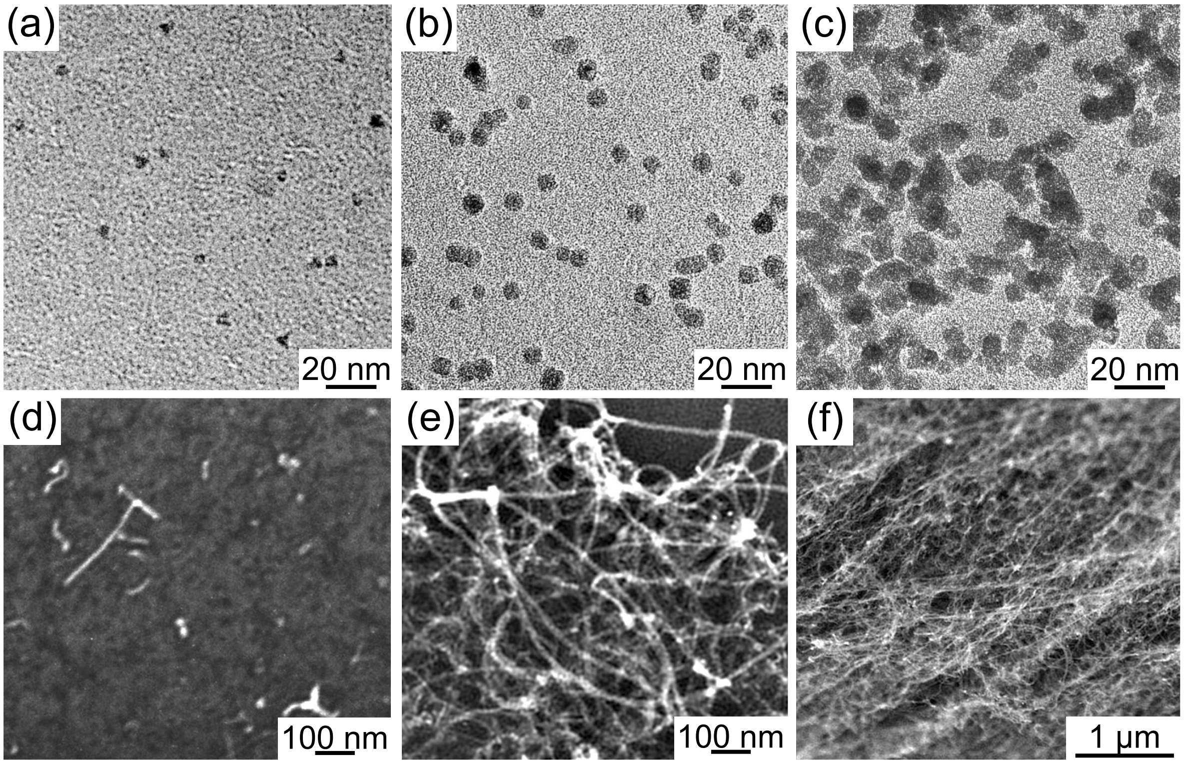

Figure 4.2: Density control: a-c) TEM micrographs of (oxidized) Fe nanoparticles of varying diameter and density deposited onto amorphous carbon films. d-f) Corresponding SEM images of CNT grown from such particles on Al_2O_3-coated Si/SiO_2 substrates via thermal CVD.

to the silicon signal of the underlying substrate. Medium particle densities, as in the sample displayed in Figure 4.2 b, lead to stronger G and D modes, and weak RBMs become visible (Figure 4.3 b). For high particle densities (Figure 4.2 f), the Raman response of the Si substrate is no longer detectable, whereas the RBMs from single-wall and possibly double-wall CNT are more distinct, although their intensity remains weak relative to the G mode (Figure 4.3 c). These changes in the Raman spectra confirm the intimate correlation between the density of the catalyst particles and the density of the CNT as seen from the TEM and SEM images. For all CNT grown from Al_2O_3/Si/SiO_2-supported Fe nanoparticles, the Raman spectra show rather weak D lines with intensity ratios of the G and the D lines in the range $11 \leq I_G/I_D \leq 17$ which point to clean

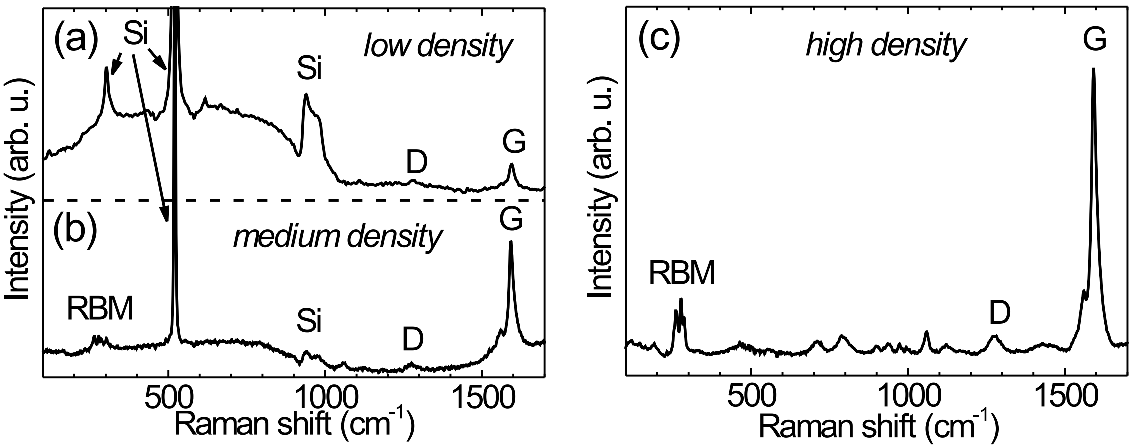

Figure 4.3: FT-Raman spectra (1064 nm) of the CNT samples displayed in Figures 4.2 d-f.

CNT with few defects. This demonstrates both the constantly high quality of the CNT samples and the homogeneity of the CVD process [73].

4.1.2 Size control

The effect of the catalyst particle size on the diameter of the resulting CNT is investigated with TEM. One result is that amorphous carbon contamination was never observed in any TEM studies of the CNT samples grown from Fe or Co catalysts in thermal CVD which again confirms the high purity of the obtained CNT material.

Figure 4.4 shows TEM micrographs of catalyst particles with a median particle diameter d_P of 5 nm and 10 nm (Figs. 4.4 a and 4.4 c) together with micrographs of the corresponding CNT samples (Figs. 4.4 b and 4.4 d). The particle size and the CNT diameter distributions, as measured in high-magnification TEM micrographs, are shown as insets in the micrographs. As expected, all size distributions follow lognormal distribution functions [137]. The median diameters of the CNT are determined to be $d_{CNT} = 5\,\text{nm}$ and $d_{CNT} = 9\,\text{nm}$, respectively, i.e., the particle diameters are in excellent agreement with the diameters of the obtained CNT. This indicates that the diameter of the catalyst particles dictates that of the resultant CNT which is similar to findings by others

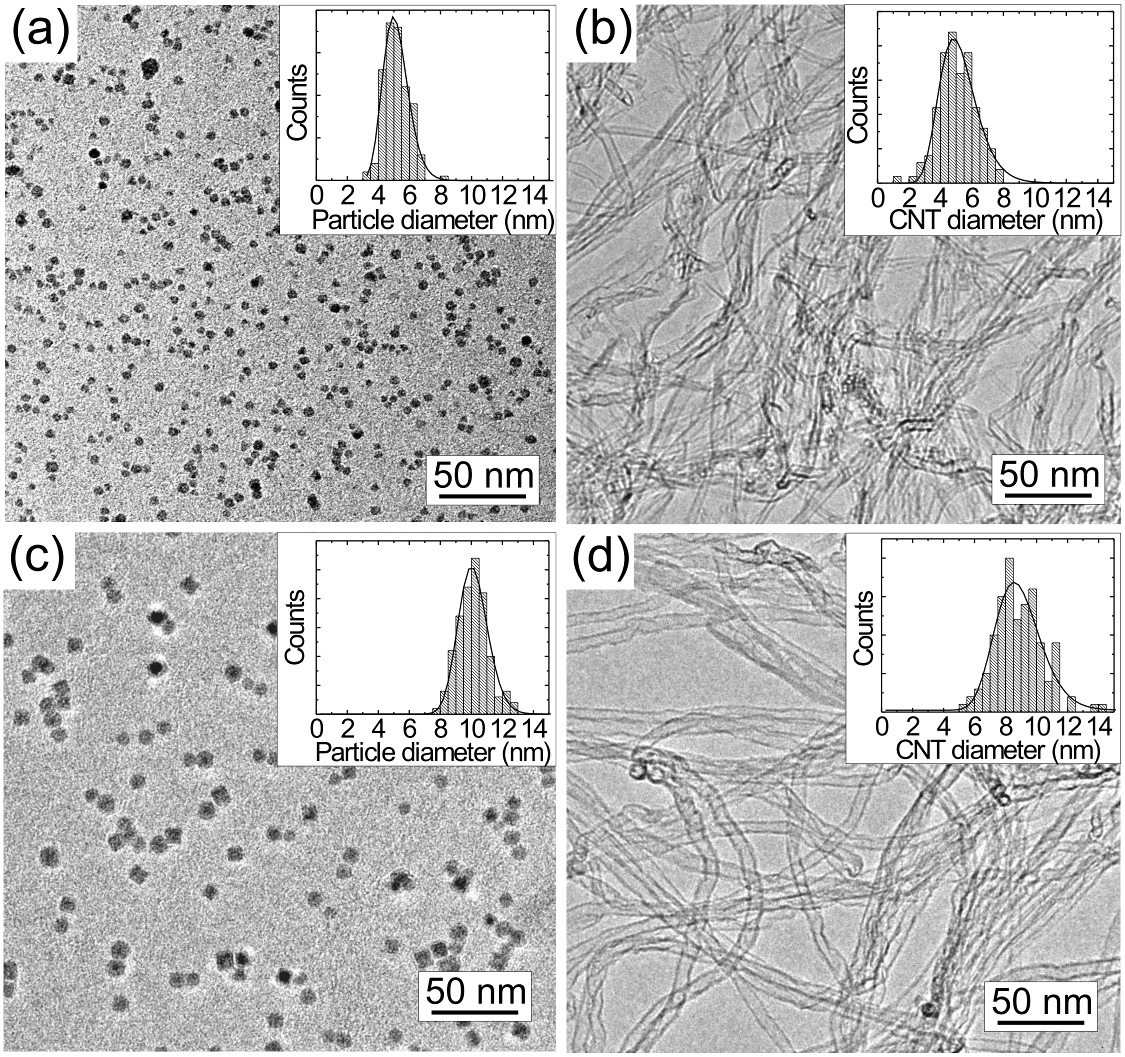

Figure 4.4: Size control: a, c) TEM micrographs of (oxidized) Fe nanoparticles with median diameters of 5 and 10 nm, respectively. b, d) Corresponding TEM micrographs of CNT grown from these particles. The particle and CNT diameter distributions are shown as insets.

[63; 71; 138] and has been discussed for substrate-based CVD for some time [139]. Further statistical analyses reveal that the distributions of the CNT diameters are slightly broader than those of the particle diameters. The additional broadening arises mainly from CNT with diameters smaller than those of the particles. This finding is attributed to the size reduction of the catalyst particles during the hydrogen treatment prior to the CNT growth step. The complete reduction of a thoroughly oxidized particle upon the H_2 treatment would lead to a maximum shrinkage of the particle diameter by about 32 % which is a reasonable upper limit for the observed effect and may well explain the observed shift of the median CNT diameter [73].

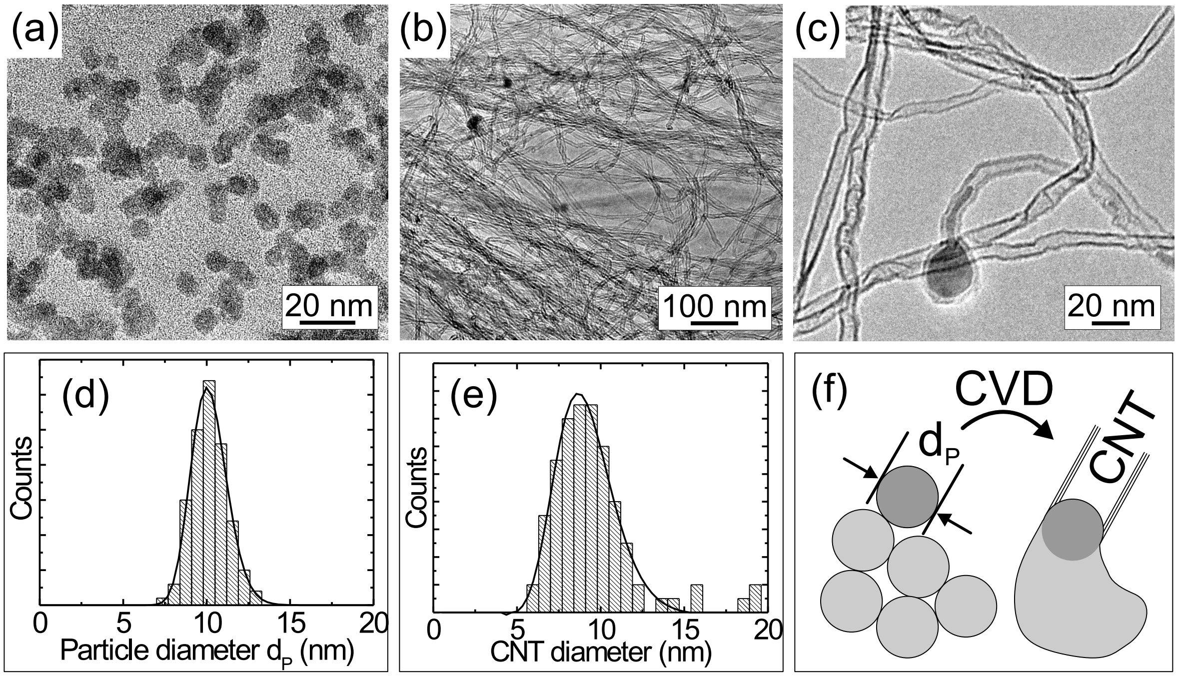

Figure 4.5: TEM micrographs of a) dense Fe catalyst particles and b, c) CNT grown from them. d, e) Corresponding particle size and CNT diameter distributions. f) Schematic illustration of the CNT growth from a particle agglomerate.

At higher particle densities, an increase of the catalyst particle size due to coalescence is expected. However, investigations of samples with very high particle densities show that this has almost no effect on the diameters of the obtained CNT. Figures 4.5 a-b show the starting Fe catalyst particles and resultant CNT from a substrate with a very high particle density where most particles are touching other particles. The corresponding distributions of both the primary particle diameter and the CNT diameter are displayed in Figures 4.5 d-e. Despite the obvious potential for particle coalescence at these densities, the median diameter of the obtained CNT ($d_{CNT} = 9\,\text{nm}$) is in remarkably good agreement with the median primary particle diameter ($d_P = 10\,\text{nm}$). Figure 4.5 c shows a CNT with a diameter corresponding to the size of a single primary particle which is attached to a much larger coalesced agglomerate. This points to a scenario where the nucleation of the CNT sets in prior to particle coalescence: The coalescence of metal nanoparticles occurs largely via surface diffusion [140]. As soon as the catalytic growth of a CNT and hence the formation of a carbon layer around the primary catalyst particle are initiated, the surface diffusion on this particle is impeded or at least modified, and, as a result, it may morphologically survive the ongoing coalescence of the particle agglomerate it belongs to (cf. Figure 4.5 f). Thus, controlling the size of the catalyst particles provides an effective control over the diameters of the resultant CNT.

In addition to this templating nature of the catalyst, a clear correlation between the catalyst particle size and the number of walls in the obtained CNT is observed [73]. Figure 4.6 shows TEM micrographs of Fe catalyst particles with a median particle diameter of $d_P = 3\,\text{nm}$ (Fig. 4.6 a) and $d_P = 10\,\text{nm}$ (Fig. 4.6 b) together with high resolution TEM micrographs of the corresponding CNT (Figs. 4.6 c-d). A statistical analysis of the number of walls has shown that the CVD processing of particles with a median diameter d_P of 3 nm nucleates the growth of CNT with predominantly two or three walls (Fig. 4.6 c), whereas particles with a median diameter d_P of 10 nm yield MWCNT with 5-11 walls (Fig. 4.6 d). The respective histograms for particle diameter and CNT number of walls are depicted as insets in each figure. The statistics are derived from analyses of 100 - 200 particles or CNT, respectively. This correlation between the number of walls of a CNT and the catalyst particle size is in good agreement with other studies where a correlation of the catalyst film thickness and both the obtained diameter and number of walls of the CNT was shown; the authors had attributed this

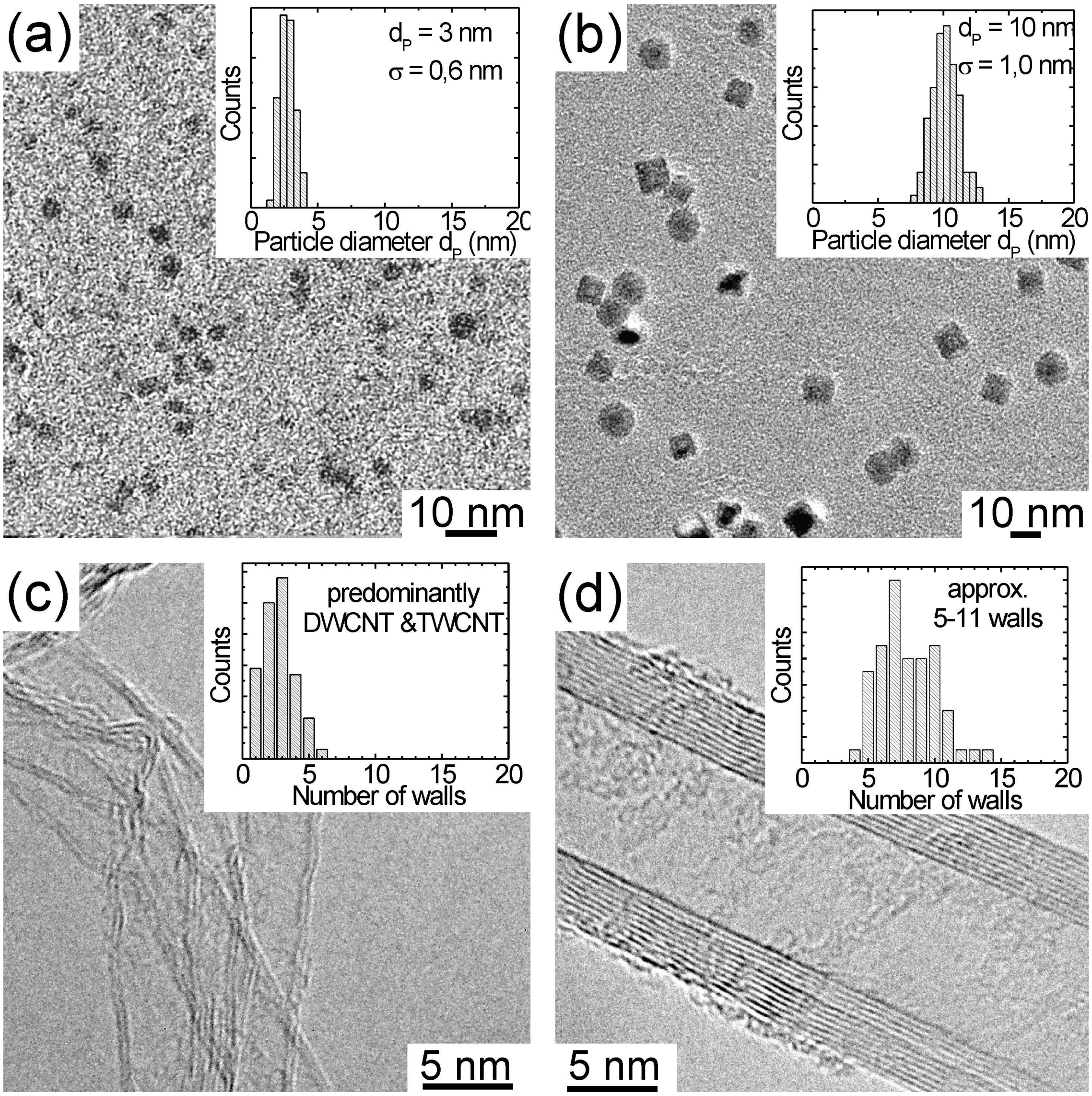

Figure 4.6: Typical TEM micrographs for two samples with a median Fe particle size of a) $d_P = 3\,\text{nm}$ and b) $d_P = 10\,\text{nm}$. c, d) HRTEM images of the corresponding CNT. Histograms derived from the statistical analyses of the particle diameter d_P and number of walls are shown as insets. The standard deviations σ as determined from Gaussian fits are also quoted.

finding to changes in the catalyst particle size [60]. The separate preparation of the catalyst particles in the approach used in this study makes it possible to reveal a clear link between the catalyst size on one side and the CNT diameter as well as the number of walls for a given set of CVD reaction parameters on the other side.

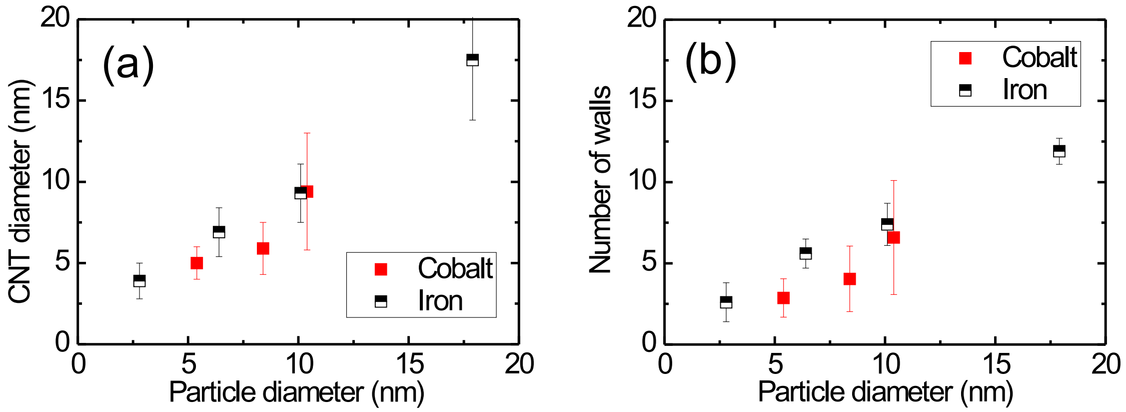

Figure 4.7: Summary of the statistical analyses obtained from CNT grown from both Fe and Co particles: a) Dependence of the outer CNT diameter on the catalyst particle diameter. b) Relationship between the catalyst particle diameter and the number of walls of the resulting CNT.

Figure 4.7 summarizes statistical analyses obtained from samples utilizing gas phase prepared Fe or Co particles of different mean diameters as deposited onto Al_2O_3-coated Si/SiO_2 supports. The clear links between the particle size and the CNT diameter as well as between the particle size and the CNT number of walls are confirmed for both catalyst materials. Figure 4.7 a shows a linear dependence of the particle and outer CNT diameters. For Fe nanoparticles, the particle diameter matches that of the CNT. In addition, the number of walls increases linearly with the catalyst particle diameter (Fig. 4.7 b). In the case of Co particles the CNT diameters as well as the mean number of graphitic walls appear to be slightly smaller as compared to Fe catalysts. This may be attributed to a reduced carbon solubility in Co as compared to Fe [116].

Figure 4.7 also indicates that these predefined catalyst particles will in principle be applicable for growing smaller diameter CNT such as SWCNT or double-wall CNT (DWCNT). Thus far, the smallest iron particles prepared by this method had a mean particle diameter d_P of 3 nm (Figs. 4.6 a and 4.7). The resulting CNT sample consists of only very thin walled CNT, mainly DWCNT and triple-wall CNT (TWCNT). Future research should involve the optimization of the particle preparation towards the growth of thin walled CNT with fully tailored diameters. In addition, the diameter distribution can be further tailored by means of quadrupole mass filtering. Such a mass filter can be integrated into the nanoparticle deposition system between the nucleation chamber and the deposition chamber (cf. chapter 3.1).

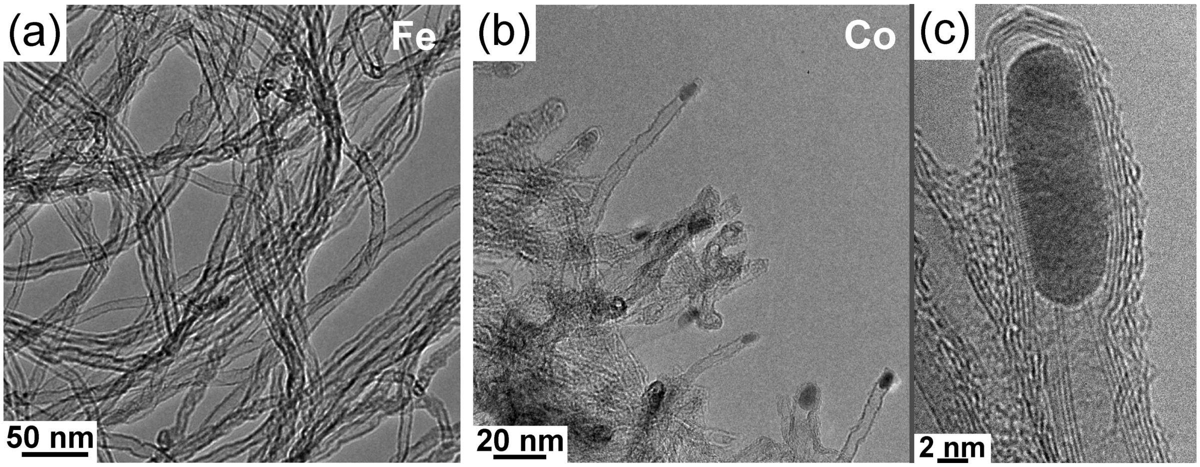

Figure 4.8: TEM micrographs of CNT grown from a) Fe and b, c) Co nanoparticles.

Although the results from statistical analysis are very similar for Fe and Co catalyst particles, the appearance of the CNT product strongly differs. In Figure 4.8 TEM micrographs of CNT grown from Fe (Fig. 4.8 a) and from Co (Figs. 4.8 b-c) are depicted. At first glance, it becomes obvious that CNT grown from Fe hardly contain any catalyst material thereby implying a base growth mechanism with the catalyst residing at the substrate, while the CNT is emerging (cf. Fig. 2.9 b). In contrast, CNT grown from Co particles include a lot of catalyst material. Catalyst particles residing along the length of the CNT core, often very close to the capped ends of the CNT, are generally observed in experiments utilizing Co catalyst particles (Fig. 4.8 b). Figure 4.8 c demonstrates that the catalyst material is fully encapsulated by the same number of graphitic sheets as form the nanotube wall indicating that the Co particle resides within the CNT's graphitic walls during growth. This points to a CNT base growth mode with the catalyst particle lifting off the substrate due to a weaker particle-substrate interaction as sketched in Figure 2.9 c.

In order to obtain CNT with few catalyst impurities a substrate-catalyst combination should be chosen, where the strong interaction impedes the catalyst to be lifted off as in the case of Fe particles on Al_2O_3. However, to produce tip-functionalized CNT, a growth mode comparable to what is obtained for Co particles on Al_2O_3 is aspired.

4.1.3 Effect of different substrates on CNT growth

In order to investigate the influence of the support on the CNT growth, comparative studies were carried out utilizing TiN and graphite as substrates. The use of these non-oxide supports leads to very different nanotube formations. Figure 4.9 compares CNT as grown from the standard Al_2O_3-coated Si/SiO_2 substrates (Figs. 4.9 a-c) with CNT grown from TiN substrates (Figs. 4.9 d-e) and graphite substrates (Figs. 4.9 f-g).

The nanotubes grown on alumina, in general, comprise of parallel walls almost entirely along their length with little structural disorder, particularly when using Fe as the catalyst (Figs. 4.9 a-c) in comparison to Co (Fig. 4.8 b). However, the use of non-oxide supports results in the formation of non-uniform structures. Here few, if any, tubes with parallel walls are obtained. Instead, the structures contain many pockets, that are stacked upon each other (similar to bamboo-like CNT). Often an elongated catalyst material is observed to reside within various places along the tube length.

While the tube diameters and diameter distributions show a direct correlation with that of the pristine catalyst particles for both Fe and Co catalysts when Al_2O_3-coated Si/SiO_2 substrates are used (Fig. 4.7 a), the CNT grown under identical CVD conditions on TiN and graphite have diameters which show no correlation with the pristine catalyst particles. These disordered structures exhibit mean diameters and diameter distributions which are significantly larger than those from the starting catalyst particles (Figs. 4.9 d-g). While the catalyst diameter ranges from 4 to 12 nm, the CNT diameters on TiN

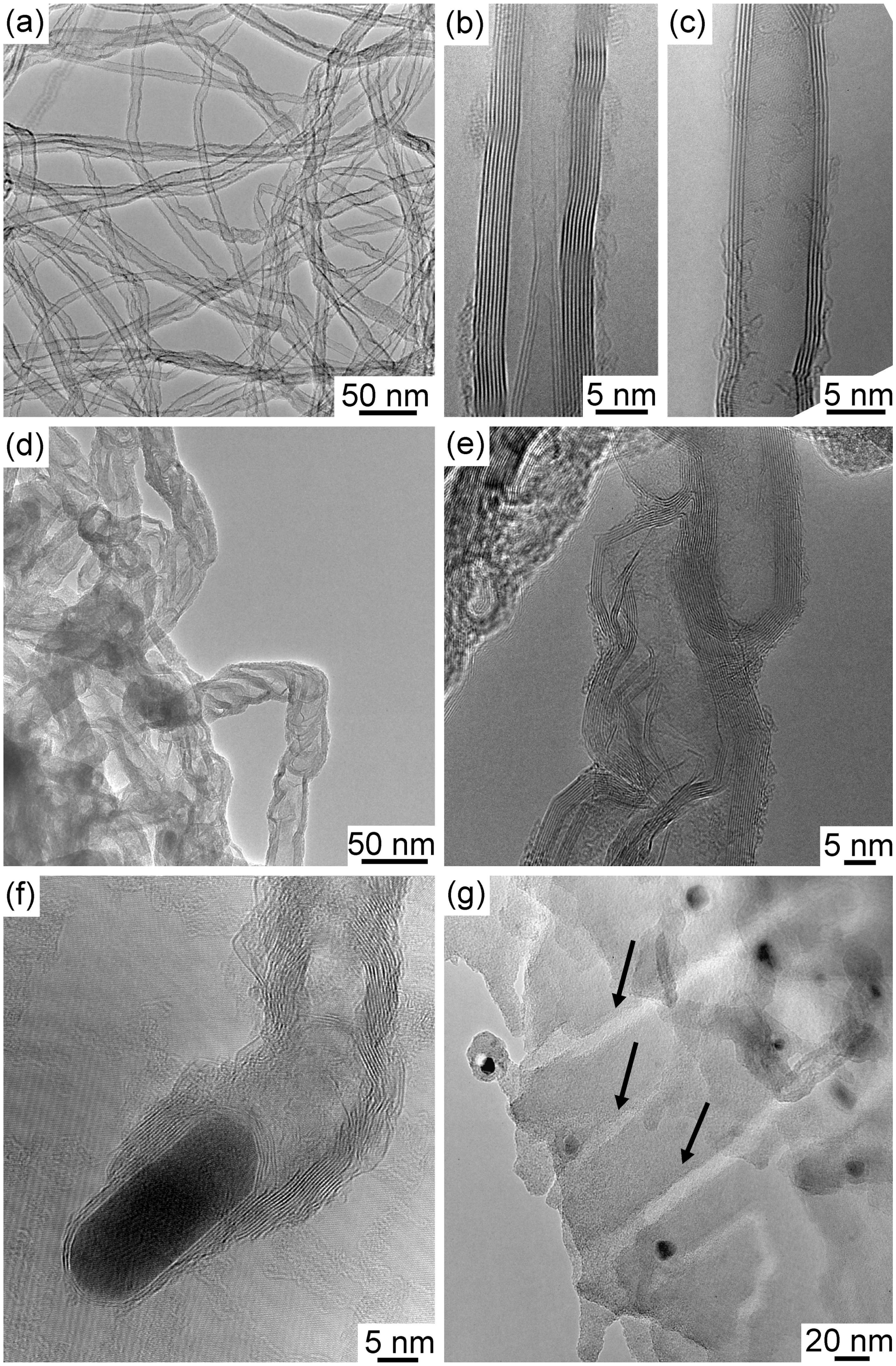

Figure 4.9: TEM micrographs providing a comparison of the morphology of CNT grown on different substrates: a-c) Al_2O_3-coated Si/SiO_2; d, e) TiN; f) graphite. g) TEM micrograph demonstrating the formation of etch tracks (marked with arrows) during CNT synthesis using graphite substrates.

range from 10 to 140 nm, and CNT diameters on graphite reach 10 to 80 nm. This indicates that the particle-substrate interaction is weaker for these non-oxide supports which results in particle coalescence during the CVD process. The use of graphite as a support leads to the formation of disordered carbon nanostructures in agreement with studies by José-Yacamán et al. [10]. Figure 4.9 f shows a bamboo-like carbon nanotube. The bamboo-structure is clearly observed to have been formed by the stacking of cap structures.

In addition, while investigating these carbon nanostructures, etch channels in the graphite substrate originating from catalyst particles were observed frequently (Fig. 4.9 g). This was attributed to catalytic hydrogenation occurring during the standard hydrogen catalyst pretreatment in the CVD process. Catalytic hydrogenation can be considered as the effective reverse to the CNT formation and is a highly relevant technique for the controlled fabrication of graphene nanoribbons (cf. chapter 2.3). Therefore this effect has been investigated in greater detail and the corresponding results will be discussed in chapter 4.3.

4.2 Carbon nanotube nucleation and growth

As demonstrated in the previous chapter the separate preparation of the catalyst independently from the CNT growth and the use of witness plates for comprehensive analysis in TEM prior to the CVD process reveal a clear link between the diameter of the catalyst particle, the diameter of the CNT and the number of walls of the CNT when standard Al_2O_3-coated Si/SiO_2 substrates are used. Further, this approach provides vital insight into CNT nucleation and growth mechanisms. In this chapter these mechanisms are discussed on the basis of the reported findings.

4.2.1 Catalyst size constraints during CNT nucleation

CNT nucleation can be defined as the process of the formation of the initial graphitic caps. This may occur via carbon dissolution into the nanoparticle and subsequent carbon precipitation when the carbon solubility limit is reached as, e.g., described in the VLS model [79]. As shown in section 4.1.2, a linear dependence of both the outer CNT diameter and the number of walls on the size of the starting catalyst is found. This finding is attributed to an increase of the catalyst volume-to-surface ratio with increasing particle size, since the availability of carbon at the point of nucleation is determined by the catalyst volume, whilst the amount of carbon required to form a cap depends on the surface area of the catalyst particle. As the volume-to-surface ratio goes up, the amount of available carbon which can precipitate from the particle during cap nucleation increases. Therefore the number of nucleation caps (hence, the number of walls) of the emerging CNT increases. This process is illustrated in Figure 4.10.

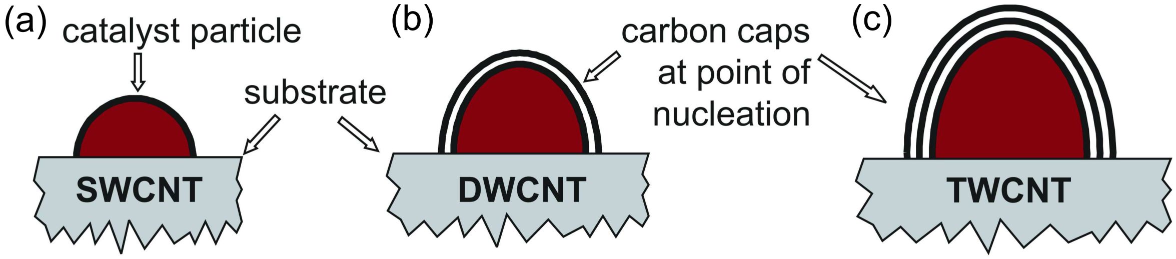

Figure 4.10: Schematic illustration of the cap nucleation: The catalyst particle diameter increases from a) to c) and so does the number of caps that nucleate. This is attributed to the change in the volume-to-surface area ratio.

The proposed model based on the volume-to-surface ratio was developed from studies on CNT synthesized via floating catalysts (i.e. catalysts residing in free space) [52]. In the case of such floating catalysts the model discusses that when the carbon saturated catalyst particle cools, the dissolved carbon precipitates and little sp^2 carbon islands form at several places on the catalyst surface. Further, there is a well-defined CNT "nucleation window", where catalyst particles of only a certain size (volume-to-surface ratio) can precipitate the amount of carbon required to form a stable hemisphere to nucleate CNT.

If the catalyst particles are too small, they cannot provide enough carbon to form a stable cap. In the case of particles that are too large, multiple sp^2 carbon islands will form which are likely to coalesce leading to the encapsulation of the catalyst. This again does not result in nanotube growth. Even larger particles will form multiple carbon shells. The concept of the catalyst's volume-to-surface ratio can also be applied to the case of substrate-based CVD [52; 141]. The outer cap nucleates first. In substrate-based CVD, carbon encapsulation of the catalyst particle is then prevented by the particle-substrate interaction and once the first nucleation cap (stable hemisphere) has been formed any excess carbon would be released *within* the first cap to form subsequent caps. The volume-to-surface ratio model as applied to substrate-based CVD then predicts that the catalyst particle size not only defines the CNT outer diameter, but also the number of walls forming the CNT. This is fully consistent with the experimental findings obtained from substrate-based CVD (section 4.1.2) and thus clearly supports the volume-to-surface ratio CNT nucleation model as applied to substrate-based CVD.

4.2.2 CNT growth from an active substrate

After CNT nucleation, i.e. the formation of the graphitic cap(s) through carbon dissolution and its subsequent precipitation, CNT growth sets it. As pointed out in chapter 2.2.3, conventional CNT growth models are insufficient in that they can not explain many of the recent experimental results, e.g. CNT growth from novel catalysts like Cu, Au, Ag, Si, Ge etc. or "catalyst-free" CNT synthesis [45; 87–94; 96; 97]. Further, within the research field of CNT growth it is generally argued that the CNT walls stem from atomic steps at the catalyst which are the points of carbon incorporation as is illustrated in Figure 4.11 a. This is highlighted by a large amount of theoretical work (e.g. [142–144]) and was also recently supported by studies using environmental TEM setups (e.g. [86; 145]). For example, Yoshida et al. reported on CNT growth to stem from Fe_3C nanoparticles during Fe catalyzed CVD as depicted in the TEM micrographs in Figure

4.11 b [145]. Hofmann et al. describe carbon nanofiber (CNF) growth using Ni catalysts and show that the carbon layers may stem from a stepped Ni surface (Fig. 4.11 c) [85].

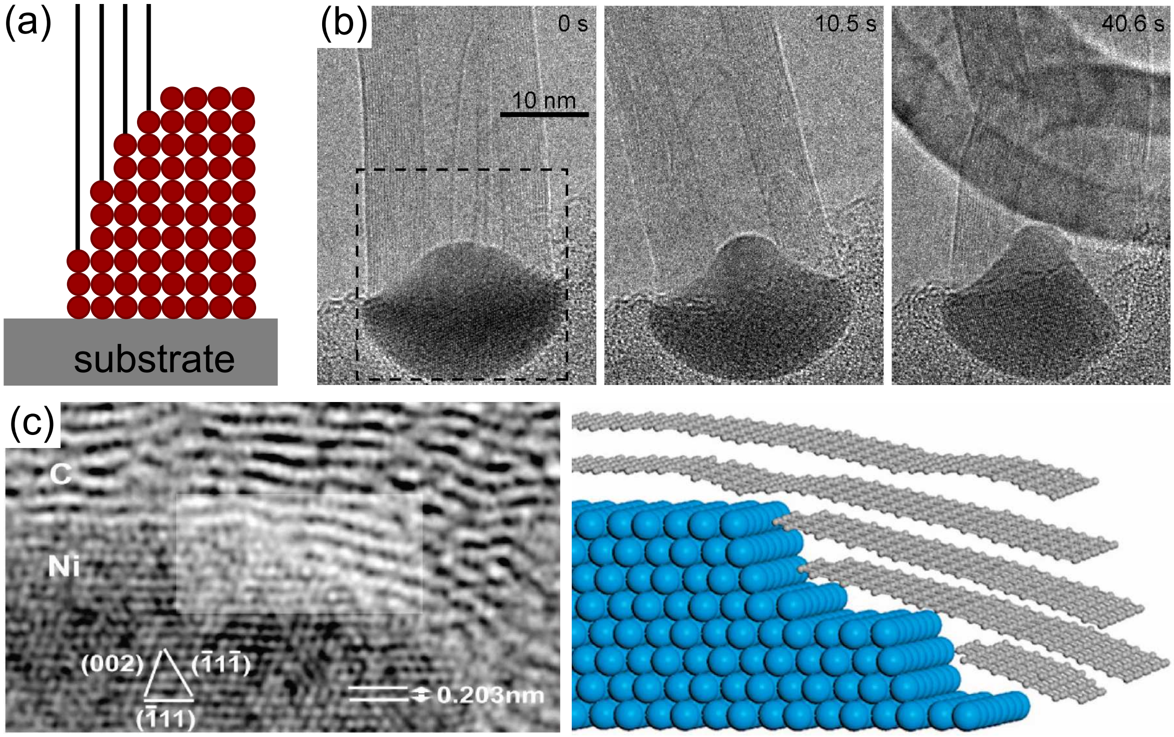

Figure 4.11: a) Schematic illustration of CNT walls rooting at atomic steps of the catalyst particle. b) Time sequence of *in-situ* CNT growth in an environmental TEM demonstrating that CNT walls can stem from Fe_3C nanoparticles during Fe catalyzed CVD (from [145]). c) TEM studies of Ni catalyzed CNF growth showing that graphitic layers terminate at the stepped Ni surface (from [85]).

Within the present study, a detailed HRTEM characterization of CNT grown from Fe nanoparticles is carried out to investigate the mutual interplay between the catalyst particle, the substrate, and the emerging graphitic carbon. The findings from these experiments are summarized in Figure 4.12. CNT which are peeled off the substrate confirm the presence of capped ends (Fig. 4.12 a). A post synthesis cleaving of substrates via focussed ion beam (FIB) in which a coverage layer (Pt or polymer binder) is formed over the as grown CNT was also performed. The tips of the CNT appear to be exclusively capped [99]. These findings are instructive in that they imply a base growth mechanism

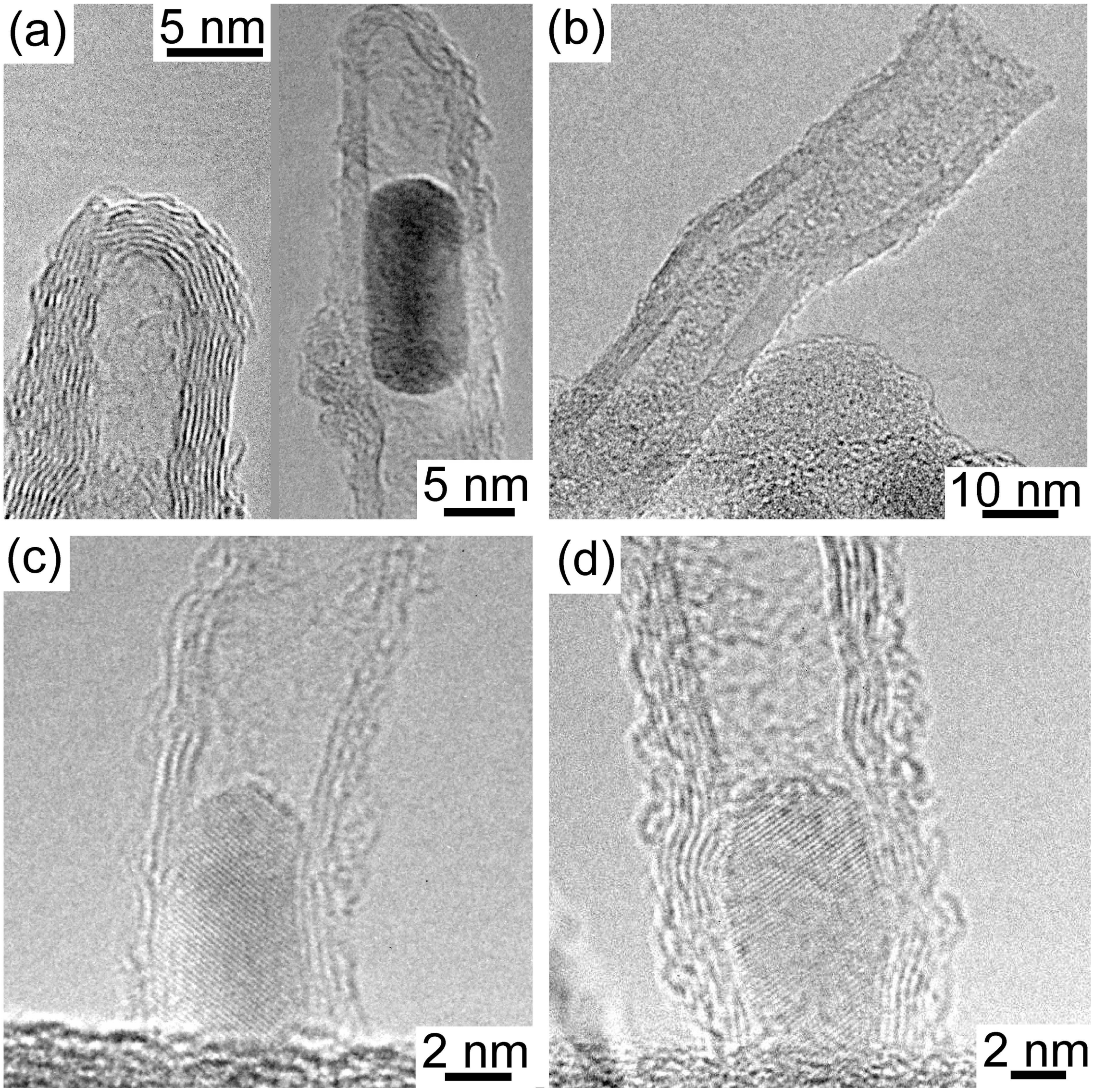

Figure 4.12: TEM micrographs of CNT ends: a) Capped CNT ends with and without encapsulated (elongated) Fe catalyst particle. b) Open CNT end without catalyst. c, d) Roots of CNT on the substrate with elongated catalyst particle in the tube core.

in agreement with previous conclusions on these samples (cf. section 4.1.2). HRTEM examinations of the peeled CNT samples reveal catalyst particles residing within the CNT cores at basically any position along the length of the CNT, sometimes even close to their capped ends (Fig. 4.12 a). Open ends with or without (elongated) catalyst material residing in the CNT core were also often observed (Fig. 4.12 b). HRTEM investigations of mechanically cleaved samples, as e.g. displayed in Figure 4.12 c-d, show open CNT with elongated catalyst particles at the interface with the substrate (Al_2O_3-coated Si/SiO_2) confirming base growth. Despite persistent HRTEM investigations, *no* CNT roots were ever observed *on* catalyst particles. Instead, elongated catalyst particles in the CNT core are frequently observed at an open end or further up the tube suggesting growth (i.e. carbon incorporation into the CNT wall) to occur on the substrate itself.

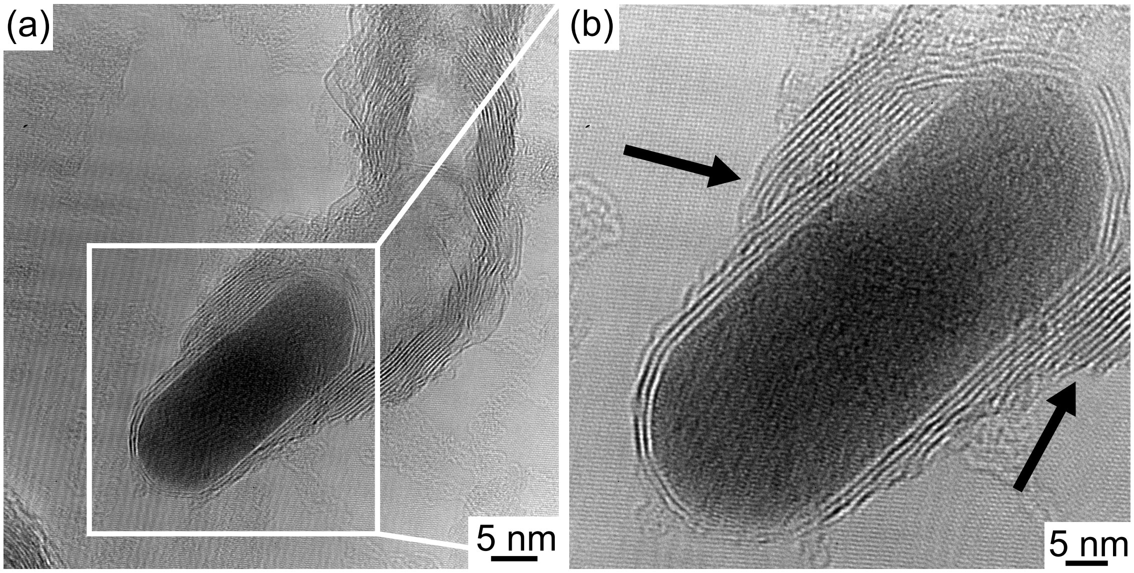

Figure 4.13: TEM micrographs of CNT grown on graphite supports highlighting CNT caps lying outside the catalyst particle (marked with arrows).

In order to obtain CNT with parallel walls a stable platform for carbon incorporation is required. As shown in chapter 4.1.3, the use of non-oxide supports results in the formation of non-uniform structures. Figure 4.13 again shows a CNT with a bamboo-type structure grown from a graphite substrate. The ends of the cap-like structures forming the tube clearly lie outside the catalyst particle (Fig. 4.13 b). The carbon layers do not terminate on the catalyst particle and easily lift off the graphite support during growth, indicating a weak interaction with the substrate.

As discussed in chapter 2.2.3, existing growth models are incomplete in that they do not explain, e.g., how CNT synthesis can be accomplished with non-metal catalysts or even "catalyst-free" [87–91; 96; 97]. As pointed out, in many cases oxygen seems to play a key role in catalyst activation as is known for CNT synthesis using laser ablation [45; 92]. In CNT growth from SiC substrates oxygen has been shown to exist at the surface of the SiC where the sp^2 carbon layers anchor on the crystal [87]. It is also known that oxides typically used as catalyst supports in CNT based CVD synthesis can themselves form graphitic carbon layers and thus provide an interface for ordered sp^2 carbon formation [98]. On the basis of this study's experimental findings for oxide supports it cannot be exclusively decided, if carbon preferentially binds at oxygen sites of the substrate or not. However, it can be assumed a nucleated cap may link to an oxygen site stabilizing the growth position and resulting into the growth of CNT with parallel walls. The argument for oxygen as a binding site is compelling since oxygen is known to enhance graphitization and activate catalysts in CNT formation [45; 89]. Further, much of the important interfacial chemistry on oxide surfaces occurs at surface defect sites [146].

In the present case of catalysts residing on an oxide support the following growth model is proposed in order to explain the experimental results: It is suggested that the line where the particle surface touches the substrate surface - that is the circumferential line around the particle *on* the substrate - serves as a circular defect site, which could then promote the growth of cylindrical graphene, i.e. the growth of a CNT. On the basis of the volume-to-surface ratio nucleation model, the CNT growth from such an "active" substrate is illustrated in Figure 4.14 for a catalyst particle with a diameter suitable for DWCNT growth. As already suggested in substrate-based CVD, the outer CNT cap nucleates first and carbon encapsulation of the catalyst is impeded by the particle-substrate interaction (Fig. 4.14 a). Since further excess carbon will form new hemispherical caps, each within the previously formed cap, the inward consecutive formation of concentric graphene caps inherently constricts the catalyst particle, thus, elongating it (Fig. 4.14 b) as observed from HRTEM investigations (Fig. 4.12). Figures 4.14 c and 4.14 d also demonstrate how a catalyst particle can reside anywhere within the core of the CNT since the particle itself plays no active role in its growth. The catalysts role is to simply provide the nucleation caps of the CNT.

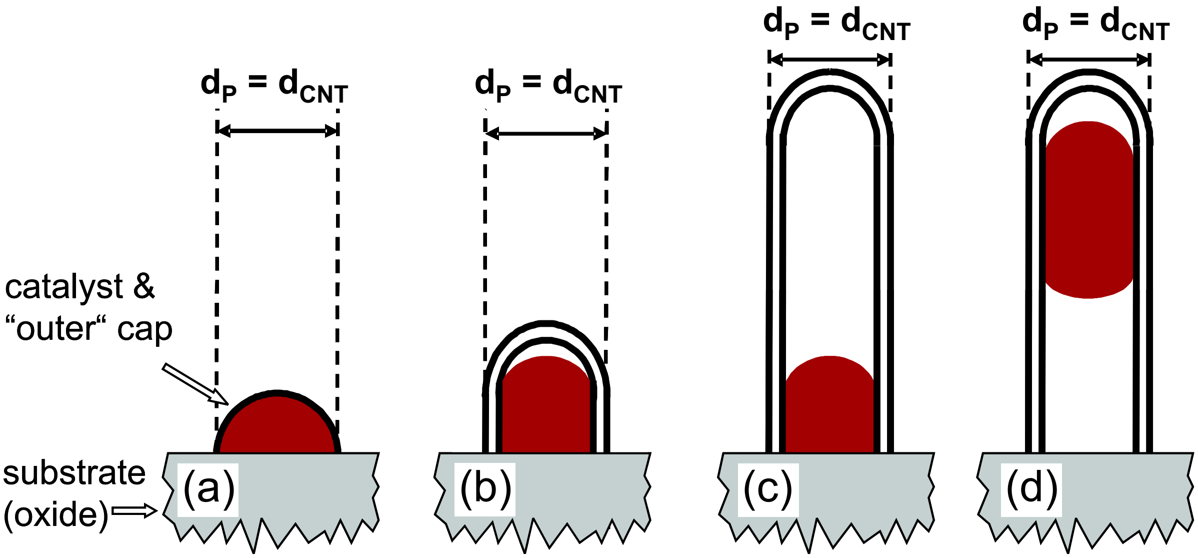

Figure 4.14: Growth of a DWCNT from an "active" oxide substrate: a) Nucleation of an outer cap from a particle with a size suitable for DWCNT growth. b) Second cap precipitates within first cap which results in particle elongation. c, d) Continued growth: The particle can reside anywhere within the CNT core.

This concept is radically different to that in which the catalyst both nucleates and grows CNT and in which the support's role is limited to merely stabilizing the catalyst particle. A catalytically active role by the support in the growth of CNT can also explain the success of oxidizers (H_2O or O_2) in enhancing the growth of substrate-based CVD synthesis of CNT (so called "super-growth") [42; 147]. Generally, it is argued that growth enhancement is due to the etching of amorphous carbon species via OH radicals, which helps prevent poisoning of the catalyst particles. Thus if the oxygen species at the surface of the support are directly involved in the growth of the CNT, it becomes crucial to maintain oxygen surface species which will be depleted by hydrogen in the CVD reaction. Inclusion of a supplementary oxidizer in the CVD reaction effectively prevents passivation of the catalytically active oxide (support) surface by re-supplying oxygen. The importance of surface hydroxide groups and surface oxygen in heterogeneous catalysis is well known [148], as is the catalytic graphitization of carbon by oxides [98; 149].

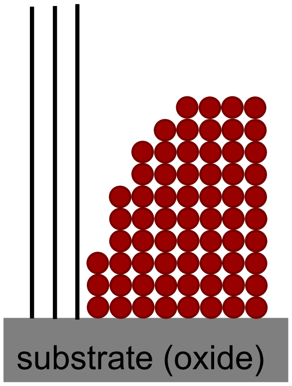

Figure 4.15: Schematic illustration of CNT walls rooting at the oxidic substrate.

Thus, the general picture of the CNT wall stemming from atomic steps on the catalyst (Fig. 4 a) should be revisited. The presented results clearly demonstrate, that the oxidic substrate enables sp^2 carbon formation. CNT walls can also originate from the substrate which is illustrated in Figure 4.15. These findings highlight the need for broader studies on the role of oxides in CNT formation.

4.3 Crystallographic etching of graphite via catalytic hydrogenation

The catalytic hydrogenation of graphite that goes along with its crystallographic etching can be considered the reverse process to the catalytic CNT growth. Recent studies by Campos et al. reveal that CNT may even be synthesized during catalytic hydrogenation [26]. Therefore a comparative study of the mutual interplay between metal catalyst particle, carbon, and hydrogen in both types of reactions is of interest in order to improve our understanding of the underlying mechanisms.

Systematic investigations on the Co-catalyzed hydrogenation of graphite using predefined Co nanoparticles are conducted during this PhD project. Aberration-corrected HRTEM provides an excellent means to investigate the structural properties of catalytic hydrogenation, viz. to resolve the atomic structure of the graphite and the catalyst particles to elucidate the etching process. The emergence of aberration-corrected electron microscopes allows to examine samples which are sensitive to knock-on damage (e.g. graphite) with a lower acceleration voltage, where knock-on damage is significantly reduced, at still very high resolution. In the first part of this chapter, the results of a thorough morphological and structural characterization of the Co catalyst particles are presented, and conclusions on the underlying hydrogenation mechanism are drawn. The second part then focuses on the anisotropic formation of etch tracks.

4.3.1 Morphological and structural characterization of the Co catalyst particles

Systematic HRTEM studies on the morphology and structure of the Co catalyst particles before and after the hydrogenation process are performed. The samples used for HRTEM investigations are prepared by gently sliding a standard copper TEM grid over the as-processed graphite block thus lifting off the topmost layers of graphene together with the Co nanoparticles.

Figure 4.16 summarizes the investigations on nanoparticles as-deposited on amorphous carbon (Fig. 4.16 a) and graphite (Fig. 4.16 b) as well as the particles deposited on graphite and subsequently heat treated in different atmospheres (Fig. 4.16 c-f). The as-deposited Co nanoparticles are found to be polycrystalline oxides (Figs. 4.16 a-b). For example, the particle in Figure 4.16 b is polycrystalline Cobalt-II-Oxide, as indicated from the lattice spacings of 0.262 nm and 0.227 nm, which correspond to the {111} and {200} planes of CoO. The particles most likely oxidize when exposed to ambient air during transfer from the nanoparticle deposition system.

Figures 4.16 c and 4.16 d show the catalyst particles after a heat treatment at 775°C in vacuum. Figure 4.16 d reveals a lattice spacing of 0.262 nm corresponding to the spacing of {111} planes in CoO. A comparison of Figure 4.16 a and 4.16 c shows that a heat treatment in vacuum only leads to coalescence of the particles, but not to the formation of etch tracks. Particles which are in contact after deposition sinter to form larger particles at elevated temperatures. The observation of large depleted areas, where no particles reside after the heat treatment (marked yellow in Fig. 4.16 c), adjacent to remarkably large particles (yellow arrow) suggests that the particles are mobile on the graphite support. A strong particle coalescence is also observed after a heat treatment in argon (Fig. 4.16 e) which is in agreement with work by Baker et al. who have investigated the particle mobility on graphite supports in different atmospheres [150; 151].

H_2 treatments at temperatures at or below 500°C did *not* lead to track formation (Fig. 4.16 f). However, the inspection of the TEM images reveals a pronounced core-shell structure of the particles with hexagonally close packed (hcp) Co cores surrounded by oxide shells, suggesting that the particles were reduced to hcp Co during the H_2 treatment and partly re-oxidized upon breaking the vacuum during sample transfer. Short etching channels upon H_2 treatment are firstly observed at 600°C (Fig. 4.17). This onset temperature for the Co-catalyzed etch track formation is in agreement with studies by Konishi et al. [100]. From Figure 4.17 one can also see that the etch tracks

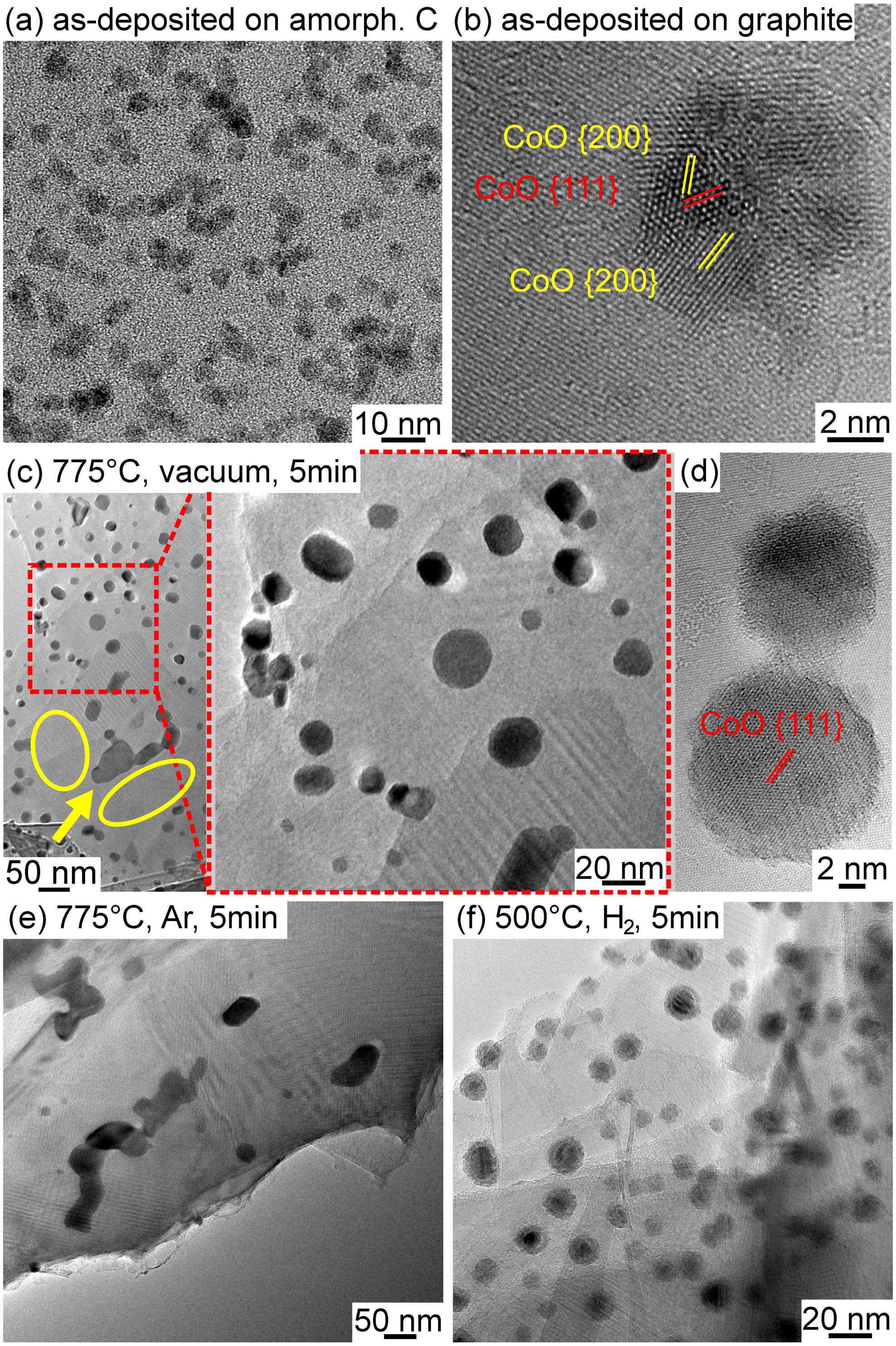

Figure 4.16: a, b) As-deposited Co nanoparticles are oxidized (mainly Cobalt-II-Oxide, CoO) and polycrystalline after deposition and transfer through air. c, d) Heat treatment in vacuum leads to a coalescence of the oxidized particles, but not to track formation. e) Argon treatment also leads to particle coalescence. f) H_2 treatment at 500°C: The reduced particles are partly re-oxidized which leads to the formation of core-shell particles.

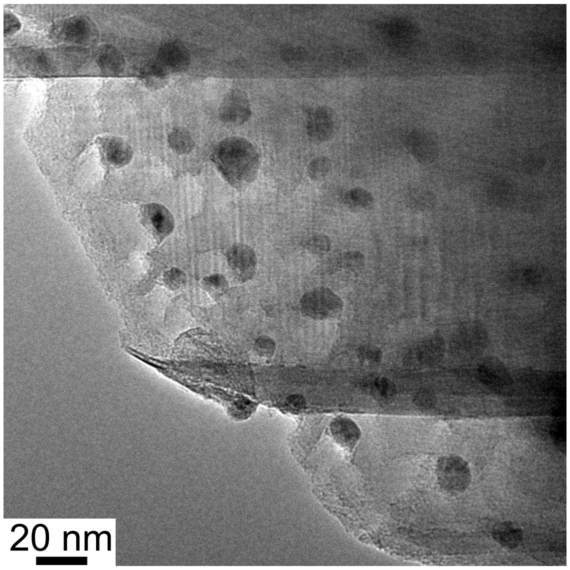

Figure 4.17: Onset of Co-catalyzed etch track formation during H_2 treatment (5 min) at 600°C.

always start at an exposed graphite edge and generally are terminated with a catalyst particle at the track front, as previously reported [22].

While the as-deposited catalyst particles as well as particles heat treated in Ar or vacuum always form polycrystalline oxides, the particle structure after the H_2 treatment at 600°C or above is more diverse. Two scenarios can occur during H_2 treatment depending on the particle placement with respect to a graphite edge: Co particles which are deposited close to an exposed graphite edge do etch carbon through the hydrogenation reaction and thus form etch channels. In contrast, Co particles resting on the flat basal graphite plane are argued to remain catalytically inactive and do not form etch channels [22]. Catalyst particles near the edge of a graphene layer interact with the dangling bonds at that edge. This interaction is stronger than that with the graphene sheet underneath. Once in the presence of H_2, the catalytic hydrogenation reaction commences. As the nanoparticle erodes the graphite sheet during this reaction, it moves maintaining maximum contact with the step edge as this is energetically favored [100; 152]. The driving force for the particle motion is the removal of carbon atoms at the leading catalyst-graphite interface, similar to the motion of metal particles encapsulated in a CNT [153].

Figure 4.18 shows three HRTEM micrographs of particles that have created etch channels originating at graphite edges. With few exceptions the particle "head" at the leading particle-graphite interface was identified to be single crystalline or polycrystalline hcp Co. The hcp Co {100} and {101} planes with lattice spacings of 0.216 nm and 0.191 nm, respectively, are marked in each figure (Figs. 4.18 a-c). At their tail ends, however, the particles are always oxidized. A closer inspection of the TEM micrographs reveal the lattice planes of CoO (Figs. 4.18 a-c) and Co_3O_4 (Fig. 4.18 c). For CoO, the lattice spacings are determined to be 0.262 nm, 0.227 nm and 0.161 nm, corresponding to the {111}, {200} and {220} planes, respectively. An even larger lattice spacing of 0.286 nm is also found, which is assigned to the Co_3O_4 {220} planes. The oxide on the track end of the Co nanoparticles most certainly originates from re-oxidation after sample removal from the reactor. In contrast, the particle heads in general seem to be protected from oxidation. This may be due to carbon (partially) dissolved in the particle close to its surface. An enrichment of carbon in the surface of a metal particle may protect the particle from re-oxidation[1]. In a similar way, catalyst particles at CNT grown via tip-growth are protected from oxidation by carbon layers that form around the catalyst particles at the end of the CNT growth process. Such particles terminating a CNT are generally found to be encapsulated by a few graphitic shells that form when the CVD reaction is stopped and the remnant dissolved carbon precipitates [154].

The HRTEM investigations further show that the front sections of the Co nanoparticles, where graphite is actively etched, is faceted and relatively coarse grained, whereas the back side of the particle, i.e. the side opposite to the etch front, is rough

---

[1] Presumably, a small amount of volatile carbon is available at the particle-graphite interface during the whole hydrogenation reaction, due to the presence of the catalyst which changes the strength of the carbon binding with the graphene sheet. As long as H_2 is present and dissociated at the particle surface, atomic hydrogen is assumed to permeate the particle due to its higher permeation rate as compared to carbon [23]. This prevents carbon from dissolving in the particle. Once H_2 is removed from the reactor, hydrogen permeation stops, and the volatile carbon atoms may diffuse into the catalyst particle, providing a protective carbon enrichment at the particle surface.

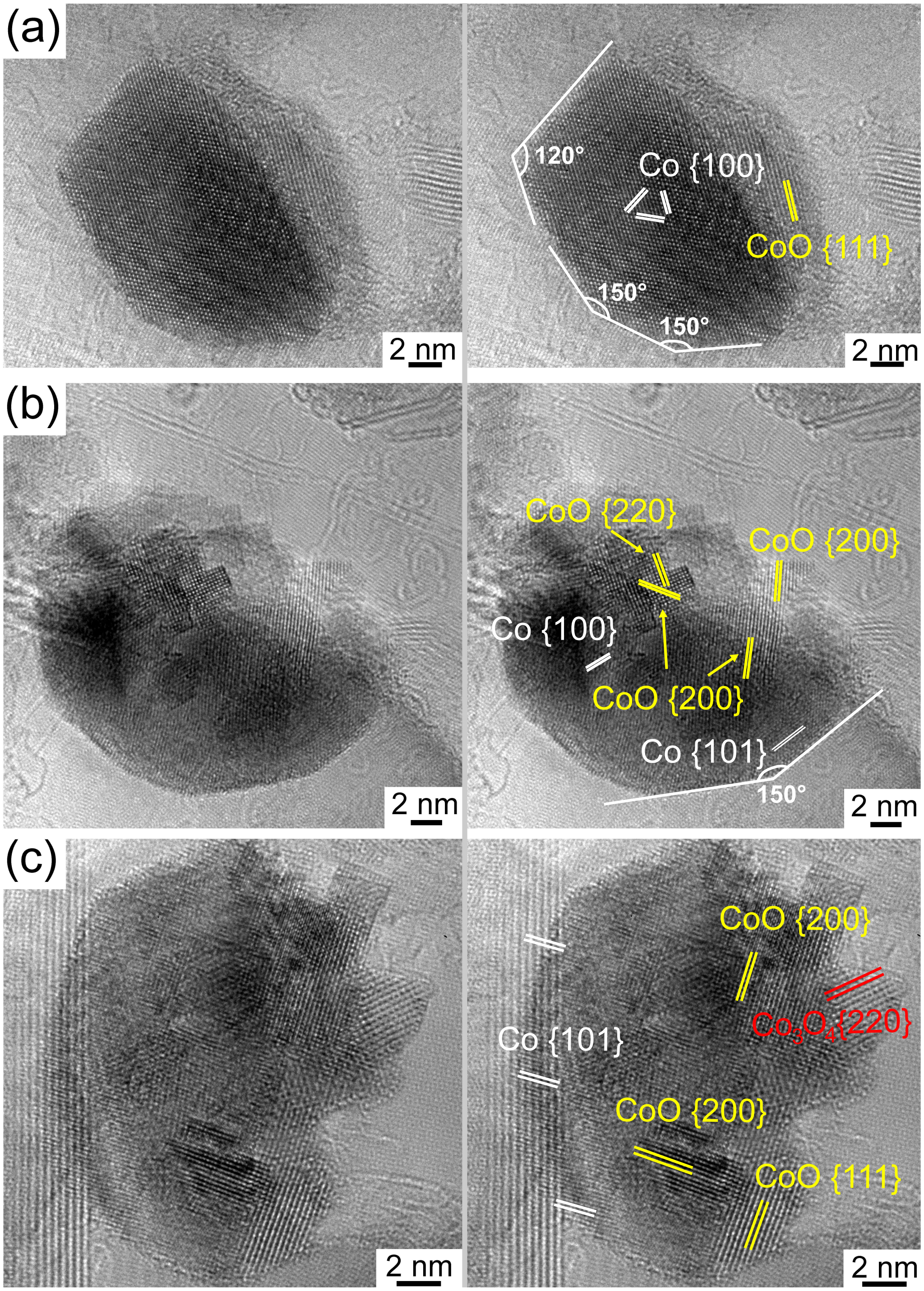

Figure 4.18: TEM micrographs of Co particles at the front of an etch track: The particles are hcp Co, however the tail end is usually re-oxidized. Particles tend to have a "half-moon" shape. The Co particles are facetted at the graphite-particle interface.

and consists of finer grains. Previous studies show that the facets of etching particles are frequently commensurate with the graphite lattice and orientated parallel to the $\langle 11\bar{2}0 \rangle$ directions of graphite [23; 101]. In the hexagonal graphite lattice these six equivalent directions always include an angle of 60°. However, in the present study the angles between the facets often appear to be multiples of 30° (Figs. 4.18 a-b). In some cases the particles are hardly faceted and show an asymmetric hemispherical shape. In general, the occurrence of facets depends on the temperature, the thermodynamic equilibrium shape of the particle, and the kinetic situation, respectively. At temperatures below the so-called roughening temperature, the formation of facets on a (free) nanoparticle is energetically favored over rough surfaces owing to a gain in surface free energy. The preferred shape of a particle is determined from a minimization of the surface free energy which varies with the type of facet. The resulting equilibrium shape is generally derived by means of the Wulff construction [155]. In case of matrix-embedded or supported particles, however, the interface energy is to be considered rather than the surface free energy. In addition, the formation kinetics of facets may be substantially affected by any type of chemical activity at the particle surface. The present case of graphite-etching Co particles represents a highly non-equilibrium situation. The chemical activity at the etching front provides additional enthalpies to overcome kinetic barriers towards the assumption of the thermodynamic equilibrium shape. Hence, the formation of facets (i.e. the equilibration of the particle) should be much easier on the etch front than on the "back side" of the particle which is in very good agreement with the experimental observation. This finding is further corroborated by the fact that a more coarse grained structure is observed on the front of the particles as compared to their back side, indicating a more advanced recrystallization at the particle front where it is kinetically promoted. The observation of facetting angles which are not necessarily multiples of 60° and are thus incommensurate with the graphite lattice may be easily attributed to the peculiarities of the present etching kinetics.

Further studies are carried out in which the samples are exposed to H_2 and subsequently post-annealed in vacuum. As described above, during the H_2 treatment, etch tracks are formed by particles residing at an exposed graphite edge. In the same way, etch track formation is observed after H_2 and post-annealing in vacuum. However, the "inactive" particles (those particles residing on the basal graphite planes that do *not* etch tracks upon H_2 treatment) show a different appearance after post-annealing in vacuum as compared to those merely subjected to a H_2 treatment. Figure 4.19 shows HRTEM micrographs of different types of etch-inactive particles after H_2 treatment and post-annealing for comparison. Figures 4.19 a-b show particles on flat basal graphite planes which were subjected to a H_2 treatment only. Depending on their size, the particles either completely re-oxidize (Fig. 4.19 a) or show a core-shell-type structure consisting of a hcp Co core and an oxide shell (Fig. 4.19 b). In Figures 4.19 c-d, particles which were treated in H_2 and subsequently left in vacuum for 5 min at 775°C are shown. Many of these Co particles are found to be encapsulated by graphitic shells. Figures 4.19 c-d show examples of such encapsulated particles, where the lattice fringes of the {100}, {002}, and {101} planes of hcp Co with lattice spacings of 0.216 nm, 0.202 nm and 0.191 nm, respectively, are indicated. The number of graphene shells surrounding the Co particle varies. A closer inspection of the HRTEM images reveals that the graphene shells originate at the Co particle surface as indicated by an arrow in Figure 4.19 d.

Carbon encapsulated nanoparticles frequently form as "side products" during CNT growth. Similar to the growth process described within the VLS model, encapsulation occurs via the precipitation of carbon from the catalyst particle, as discussed in chapter 2.2.3. Since the graphitic shells are observed around etch-inactive particles, the etching of graphite can be ruled out as a possible process for providing the necessary carbon. Most likely, spurious amorphous carbon on the graphite surface serves as the required carbon source. Apparently, the graphite surface is not entirely clean as often concluded from HRTEM studies of carbon nanomaterials [156]. In addition, CH_4 as produced in the hydrogenation process may act as an additional carbon source. However, the

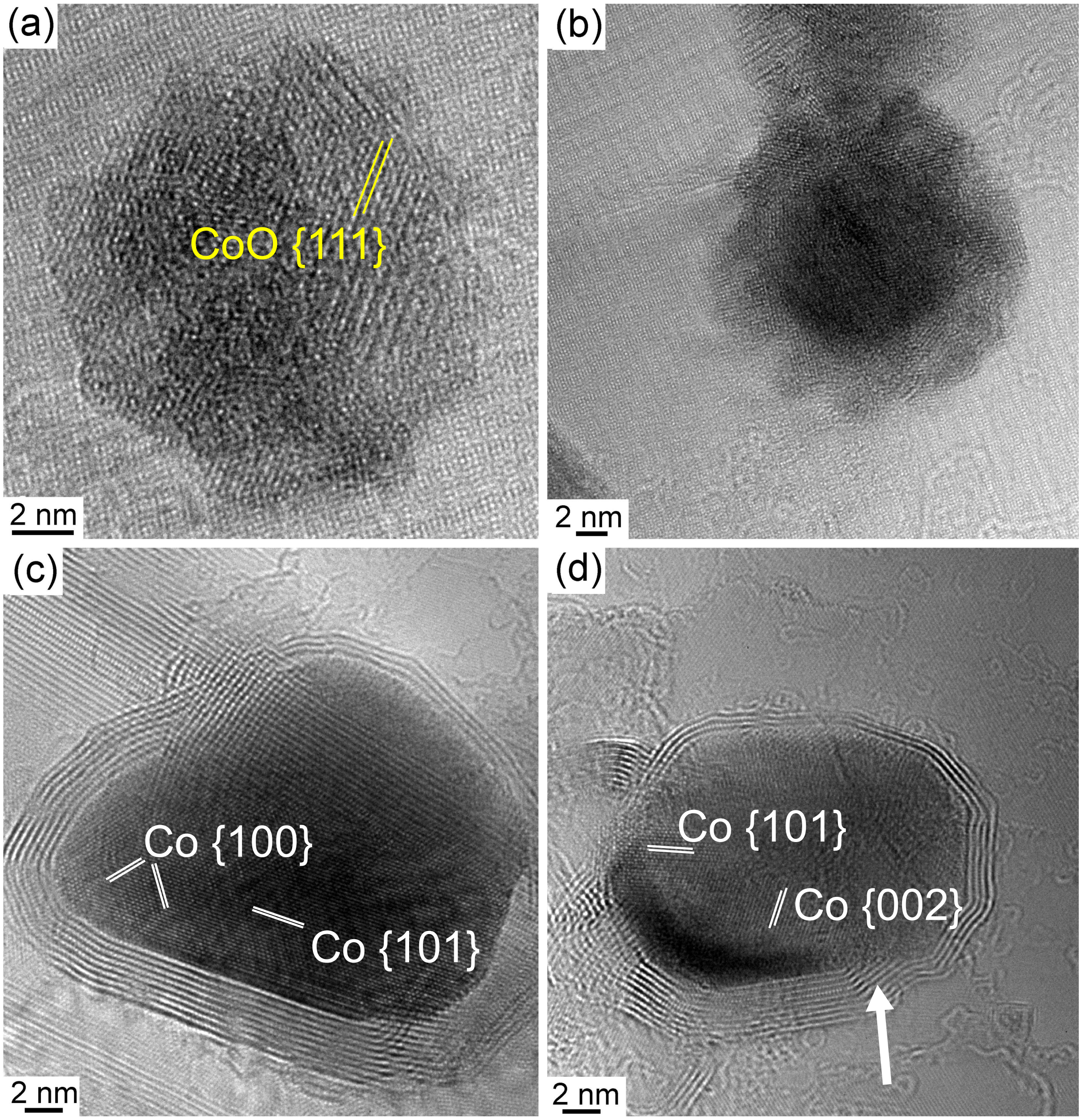

Figure 4.19: a, b) H_2 treatment at 775°C: Co particles re-oxidize completely or form core-shell particles. c-d) H_2 treatment plus additional 5 min in vacuum at 775°C: Many pure hcp Co particles are encapsulated in graphitic shells that stem from the Co particle.

amount of CH_4 that is still present when stopping the reaction is extremely low (cf. chapter 2.3). It is therefore assumed that the mobile etch-inactive particles absorb the amorphous carbon they come into contact with on the graphite surface. Upon cooling the carbon then precipitates from the particle forming graphitic shells which protect these etch-inactive catalyst particles from re-oxidation upon breaking the vacuum.

This encapsulation of the etch-inactive particles also provides information regarding the hydrogenation mechanism. As described in chapter 2.3 there are still two mechanisms disputed [25; 100]. In the first and most accepted interfacial hydrogen mechanism, it is postulated that hydrogen is adsorbed at the catalyst surface where upon it dissociates into atoms. These hydrogen atoms can then diffuse via bulk and/or surface diffusion to the graphite-particle interface at the head of a channel where they react to CH_4 [23; 101]. In the competing carbon dissolution model, dissolved carbon is assumed to diffuse to the outer particle surface where it reacts with hydrogen to form CH_4 [23].

Figure 4.20 discusses the experimental findings, schematically summarizing the observations. In the present study, the hydrogenation reaction was brought to a rapid stop at the end of each run. If the catalyst particles contained carbon during this rapid cooling process it would be expected to precipitate, as illustrated in figure 4.20 a[2]. In this instance, the formation of graphitic encapsulations as observed in samples that were post-annealed in vacuum therefore suggests bulk diffusion of carbon in the particles. Here, the 5 min of heat treatment in vacuum provided enough time for carbon diffusion towards the particle or for the mobile particle to pick up spurious carbon, respectively. The varying number of precipitated graphene shells surrounding the Co particle may therefore be attributed to a different amount of carbon available in different regions of the graphite surface.

The etch-inactive particles after *only* undergoing the hydrogenation reaction (i.e. a mere H_2 treatment) are *not* protected from re-oxidation, i.e. do *not* form graphitic

---

[2] Cobalt carbides are thought to be difficult to form thermodynamically [116]. Metastable cobalt carbides have been synthesized via co-sputtering, mechanical alloying or ion implantation [157–159]. In the present study cobalt carbide phases were never observed in any of the analyzed particles.

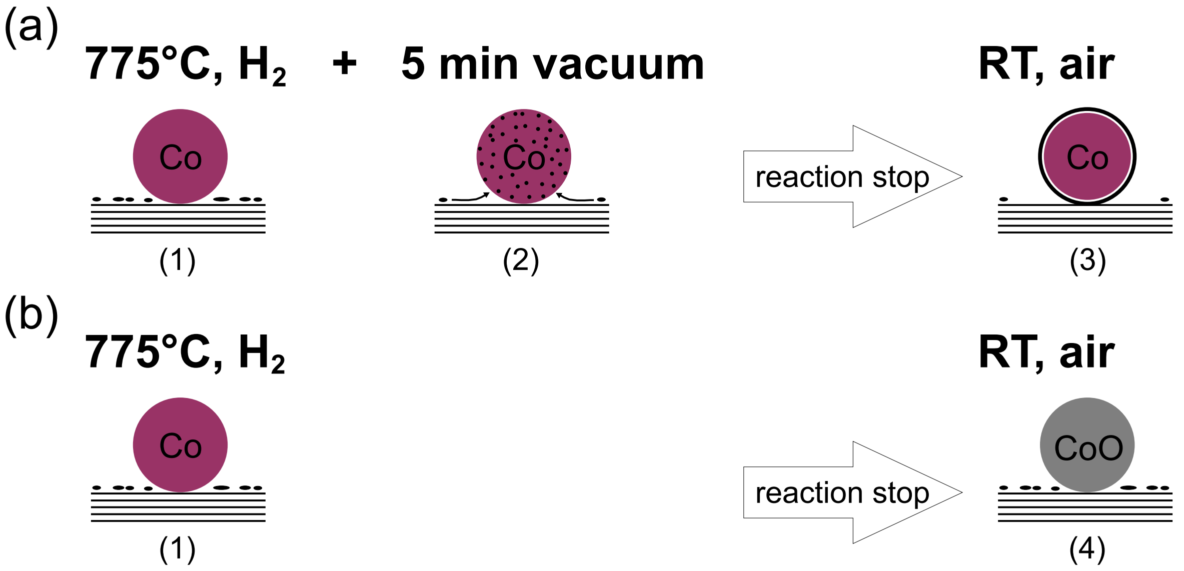

Figure 4.20: a) H_2 treatment and additional heat treatment in vacuum at 775°C before stopping the reaction: (1) As long as H_2 is present, it prevents carbon from diffusing into the catalyst particle. (2) During the vacuum treatment carbon has time to diffuse towards the particle *or* the particle itself moves and picks up spurious carbon. (3) Upon cooling to room temperature (RT), dissolved carbon precipitates, forming graphitic shell(s) which protect the particle from re-oxidation in ambient air. b) H_2 treatment at 775°C and rapid stop of the reaction: (1) As long as H_2 is present, it prevents carbon from diffusing into the catalyst particle. (4) Due to the rapid stop of the reaction, carbon has no time to be dissolved in the particle. Therefore the particles are not protected from re-oxidation when breaking the vacuum.

shells when the reaction is stopped (Fig. 4.20 b). Due to the rapid stop of the reaction in this case, there is not enough time for either spurious carbon to diffuse towards and be dissolved in the particle or for the mobile particle to collect enough carbon, respectively, to form protecting graphite shells upon cooling. It is known that the bulk hydrogen permeation rate is much higher than that for carbon (e.g. two orders of magnitude in Ni at 975 K) [23]. Thus, as long as H_2 is present in the reactor it effectively penetrates the particle and therefore prevents carbon from diffusing into the catalyst particle. Hence, since no shells are observed on particles after a mere hydrogenation reaction, the present data point against the carbon dissolution mechanism. Thus the data support the interfacial hydrogen mechanism. This is further corroborated by earlier findings by Keep et al. who reported that the rate of carbon gasification, i.e. the etching rate, is proportional to the external surface area of the channeling particle and not to the leading graphite-particle interface (cf. chapter 2.3, [23]).

4.3.2 Anisotropic etching of graphite

As already indicated above, catalytic hydrogenation produces patterns of anisotropically etched channels on the graphite surface. Figure 4.21 shows such patterns etched from Co nanoparticles at different H_2 treatment temperatures. In these experiments, the lowest temperature at which etch tracks are observed, i.e. the onset temperature for Co catalyzed hydrogenation, is 600°C (Fig. 4.21 a-b). This temperature is significantly lower than the one reported for Ni (700°C) and Fe (900°C) [24; 25], indicating a higher catalytic activity of Co. As compared to the very short tracks formed during the H_2 treatment at 600°C (Fig. 4.21 a-b), the etch channels observed at 775°C are much longer (Fig. 4.21 c-d), indicating an increasing track length (increasing catalyst activity) with increasing temperature. Also an extended H_2 treatment time results in the formation of longer tracks, as confirmed by hydrogenation treatments with 30 min reaction time (not shown here).

At 775°C, alterations of the etch direction (Fig. 4.21 c-d) are also frequently observed. When the etch direction changes, the bending angles between adjacent etch directions are found to be predominantly multiples of 60°, commensurate with the graphite lattice which highlights the anisotropy of graphite etching (Figs. 4.21 b-d). Some bending angles of 30° can also be found. If carbon atoms are removed from an armchair edge, channels terminated with zigzag edges are formed. It is known that the removal of a carbon atom from an armchair edge costs less energy than its removal from a zigzag edge [25]. Thus, zigzag channels, i.e. channels along the $\langle 11\bar{2}0\rangle$ directions, should be favored which is experimentally indeed observed in most cases [22–24]. Typical bending angles of 60° and 120° are to be expected. 30° bends are observed less frequently, since they involve a change from a $\langle 11\bar{2}0\rangle$ to a $\langle 10\bar{1}0\rangle$ direction or vice versa.

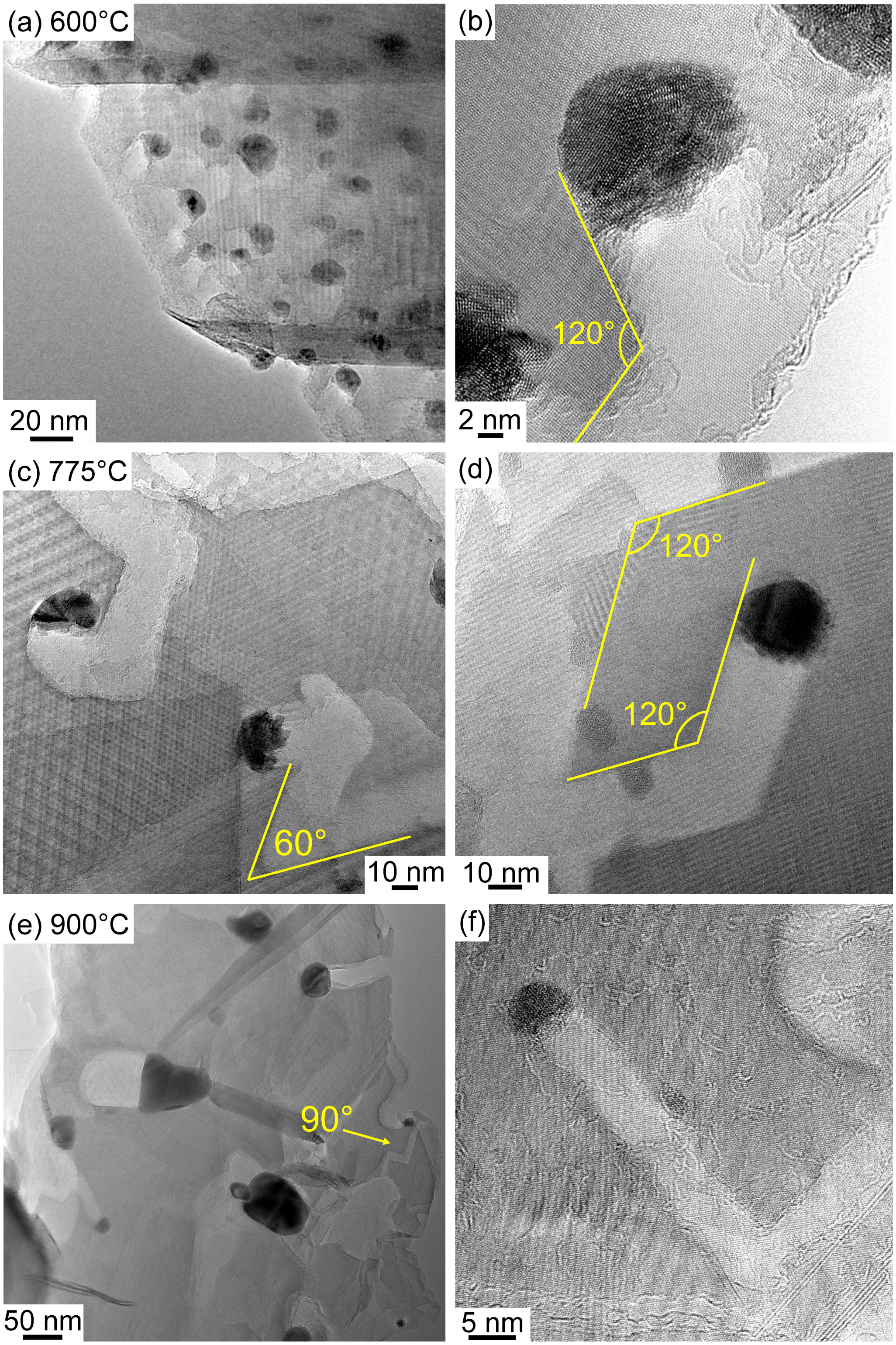

Figure 4.21: Graphite flakes as lifted off the graphite substrate showing etch tracks formed by Co nanoparticles in H_2 at different process temperatures.

At moderate process temperatures (600°C - 775°C), channels with widths as narrow as 8 nm are observed. This is slightly larger than the mean particle diameter of 5 nm prior to the reaction. This increase of the track width over the mean primary particle size is attributed to the coalescence of catalyst particles during the hydrogenation and the asymmetrical reshaping of the particle to keep maximum surface contact with the graphite step edge. Nonetheless will the track width be the larger, the larger the mean diameter of the primary catalyst particles is, thereby providing a way to tailor the track width by choosing a particular primary particle size. At higher process temperatures (e.g. 900°C) the channel width distribution becomes very broad, ranging from 4 nm narrow channels to channels with widths larger than 50 nm (Figs. 4.21 e-f). The reduced diameter particles arise from particle splitting similar to catalyst particle formation from thin films [58], whilst the enlarged catalyst particles are attributed to strong particle coalescence.

Figure 4.22 a shows a low voltage HRTEM micrograph of etch tracks formed by Co particles at 600°C. Fourier enhancement of the micrograph allows to identify the graphite structure and to determine the etch direction to be along armchair edges, i.e. along a $\langle 10\bar{1}0 \rangle$ direction (Figs. 4.22 b-c). Figure 4.22 d shows a magnified image of the area marked blue in Figure 4.22 b to illustrate the graphite structure. The graphite unit cell (green rhombus) and the main crystallographic directions of graphite, i.e. zigzag and armchair edges, are highlighted in yellow and orange, respectively. Using this analysis method, the $[10\bar{1}0]$ direction (along armchair edges) was identified as the etching direction in five other cases, whereas the $[11\bar{2}0]$ direction (along zigzag edges) was observed only once.

Upon etching with Ni nanoparticles, the etching directions are most frequently observed to lie along the zigzag edges [23; 25]. According to Tomita et al., the ratio of the number of channels along the $\langle 11\bar{2}0 \rangle$ and $\langle 10\bar{1}0 \rangle$ directions is significantly higher for Ni than for Co [22]. However, very small Ni particles (< 10 nm) seem to preferentially etch

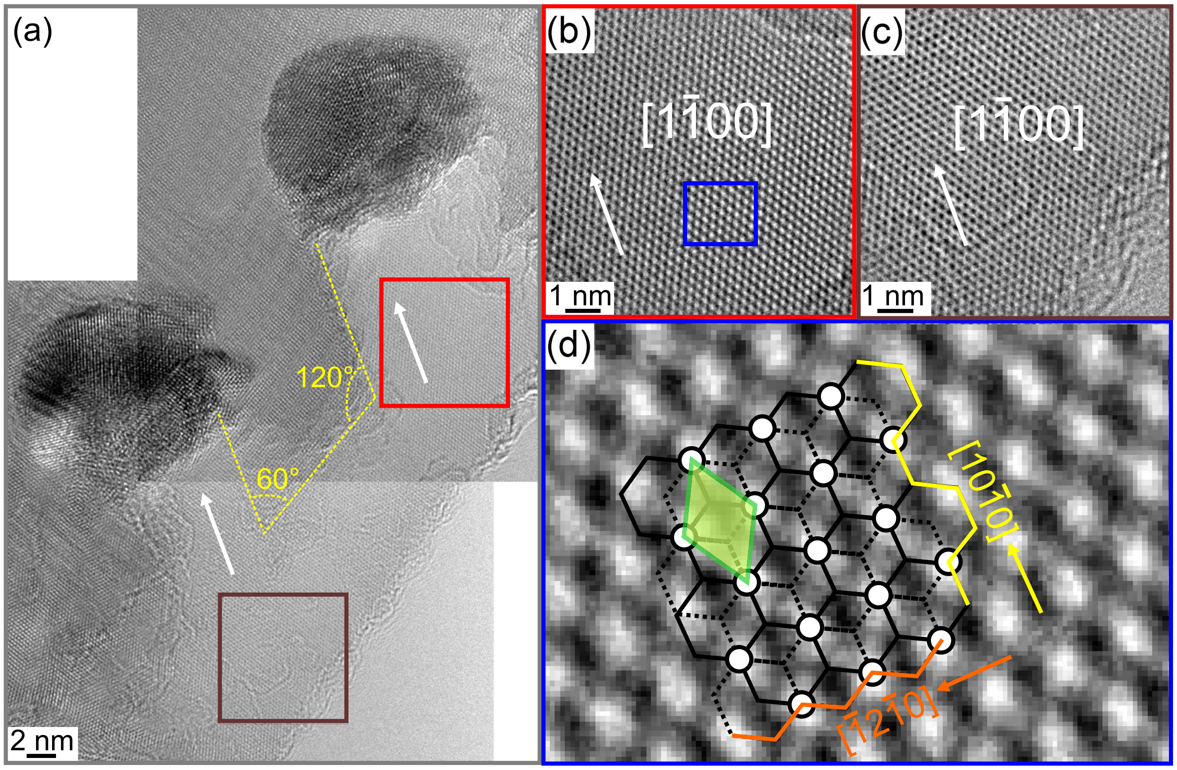

Figure 4.22: a) HRTEM micrograph of Co nanoparticles etching graphite. b, c) Fourier enhanced micrographs of the marked areas in a) revealing the graphite structure and etching direction. d) Magnified image of the marked area in b) and illustration of the graphite structure including unit cell (green rhombus) and the main crystallographic directions.

along the $\langle 10\bar{1}0\rangle$ directions potentially allowing to tailor graphene nanostructures with specific zigzag or armchair edges [25].

Hence, the choice of both the catalyst material and the particle size provides a means to control the etching direction which suggests that engineering the edge termination of graphene nanostructures could indeed be possible. Such a tailored fabrication of armchair or zigzag nanoribbons would in turn allow to effectively control their electronic properties [160; 161].

5 Nanomagnet - carbon nanotube hybrid structures

The advancement in CNT technology includes significant interest in their functionalization so as to modify or improve their chemical and physical properties. In particular, the selective functionalization of the CNT ends opens exciting opportunities to design nanoscale architectures and networks. Owing to their remarkable magnetic properties FePt alloy particles have attracted extensive attention. In particular, the ordered tetragonal $L1_0$ phase of FePt exhibits a large magneto-crystalline anisotropy [28]. This allows for a reduction of the nanoparticle size to below 4 nm at room temperature while still retaining the stability of the magnetization against thermal fluctuations [29]. Hence, a combination of this material with CNT is of strong interest in future ferromagnetic nanoelectronics.

It is therefore an objective within this study to investigate if the use of FePt catalysts facilitates the hard-magnetic functionalization of CNT tips. As opposed to other approaches where magnetic particles are post-deposited after the CNT synthesis [162] or CNT are chemically functionalized with particles [163], the present work aims at preparing hard-magnetic CNT hybrids in a single step. Here, the CVD process itself is supposed to provide the necessary thermal energy to form the desired hard-magnetic $L1_0$ phase. For this purpose both, thermal and plasma enhanced CVD are investigated. While the experiments using thermal CVD were carried out in collaboration with C. Schünemann within the framework of his Diploma thesis, the PE-CVD experiments were conducted in close cooperation with C. Täschner (IFF, IFW Dresden).

5.1 CNT from predefined FePt nanoparticles via thermal CVD

Following the successful fabrication of CNT from predefined gas phase prepared Fe and Co nanoparticles and the hereby achieved growth control, CNT are grown by thermal CVD from binary FePt catalyst nanoparticles using cyclohexane as carbon feedstock. So far, FePt is rarely utilized as catalyst for CNT synthesis [114; 164; 165].

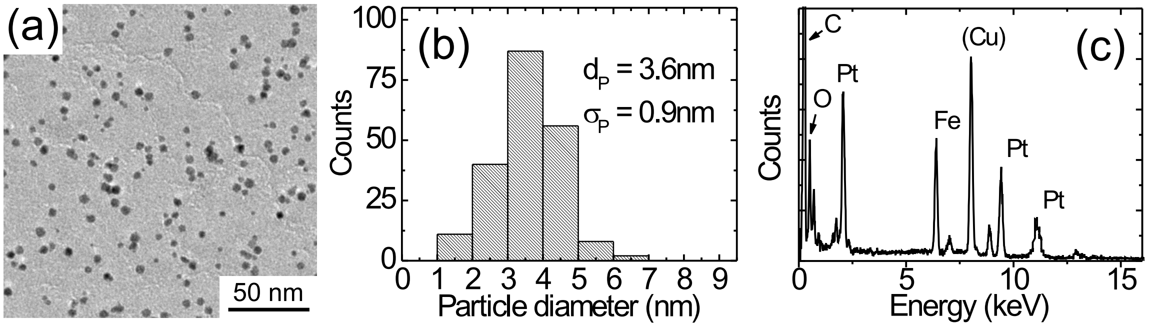

Figure 5.1: Characterization of the FePt catalyst material: a) TEM micrograph of the as-prepared FePt catalyst nanoparticles. b) Corresponding particle diameter distribution. c) Typical EDX spectrum.

Figure 5.1 provides detailed information on the as-prepared FePt catalyst particles. The TEM overview (witness plate) in Figure 5.1 a shows that the particles have a uniform morphology with a mean particle diameter d_P of 3.6 ± 0.9 nm and a narrow particle diameter distribution (Fig. 5.1 b). From quantitative analysis of various EDX spectra it was determined that the catalyst particles contain 50 ± 2 at-% Fe and 50 $\mp$ 2 at-% Pt, respectively, thus matching the target composition very well (Fig. 5.1 c). Since the FePt nanoparticles were deposited onto a carbon coated Cu-TEM-grid and exposed to air prior to examination, C, O, and Cu signals are also present in the spectrum.

Systematic studies were carried out to explore the growth of CNT via FePt-catalyzed thermal CVD across a broad range of temperatures. The investigations show strong changes in the CNT structure, diameter and their density on the CVD substrate depending on the CVD furnace temperature (560 °C to 830 °C). Figure 5.2 shows the dependence of the outer CNT diameter with increasing CVD furnace temperature as

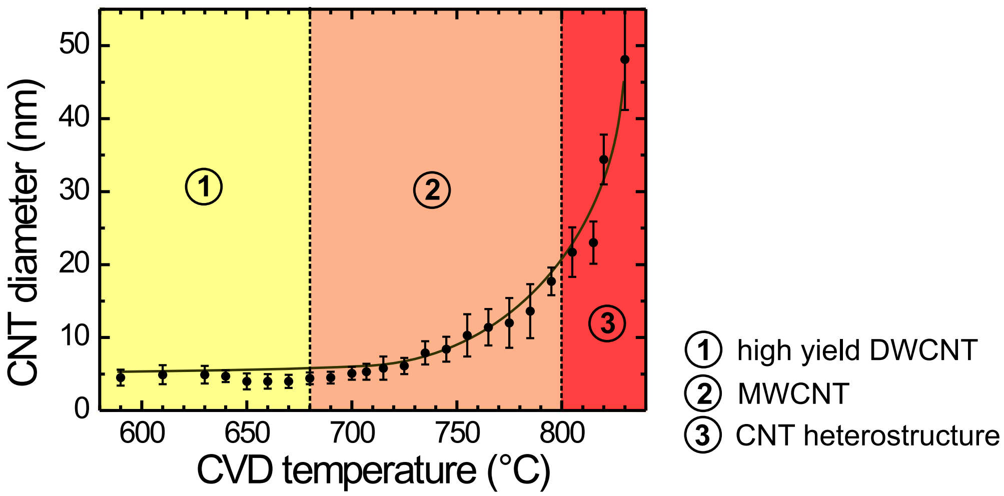

Figure 5.2: Evolution of the outer CNT diameter with CVD temperature (the line is a guide to the eye) [166].

determined from TEM analysis of at least 200 CNT at each temperature [166]. As will be shortly summarized in the following, the investigated temperature range can be roughly divided into three temperature regions highlighted in Figure 5.2. In region 1 ($590^{\circ}\mathrm{C} \leq \mathrm{T} \leq 680^{\circ}\mathrm{C}$), a high yield of double-wall CNT is obtained. Region 2 ($680^{\circ}\mathrm{C} \leq \mathrm{T} \leq 800^{\circ}\mathrm{C}$) is characterized by the growth of MWCNT with increasing outer diameters. In region 3 ($\mathrm{T} < 800^{\circ}\mathrm{C}$) the morphology of the growth product changes drastically. Here, coaxial CNT heterostructures are obtained.

CNT growth from FePt nanoparticles is first observed at a synthesis temperature of 590 °C which is very low for CNT synthesis via thermally activated CVD. Figure 5.3 shows a SEM and a high resolution TEM micrograph of the obtained CNT, which are thin-walled, mainly double-wall CNT. However the yield is still quite low. The onset temperature in experiments using FePt thus lies significantly below 720°C where the onset of CNT growth was reported by Grüneis et al. for thermal CVD with Fe as a catalyst [133]. It is well-known that the catalyst material plays a vital role in CNT nucleation. The onset of the CNT formation is believed to be determined by the melting point of the catalyst-carbon mixture. Below the eutectic temperature the CNT

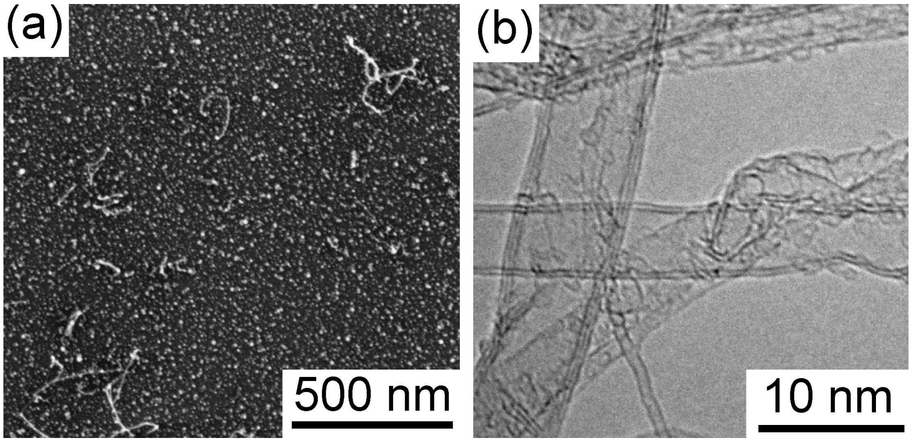

Figure 5.3: Low temperature CNT synthesis from FePt: a) SEM and b) high resolution TEM micrograph of CNT synthesized at 590 °C.

formation dramatically drops [167]. Since in the present experiments the same carbon source as compared to the experiment of Grüneis et al. and a similar experimental setup are used, the lower onset temperature for CNT growth is to be attributed to the FePt catalyst. Here, the presence of Pt which is highly active in the decomposition of the carbon feedstock, may also support the low temperature synthesis [11].

In the temperature range from 590 °C to 680 °C, large amounts of DWCNT are obtained (cf. region 1 in Fig. 5.2) with highest yields at 660 °C. Figure 5.4 shows CNT grown at 660 °C. A comparison of the SEM images from samples prepared at 590 °C (Fig. 5.3 a) and at 660 °C (Fig. 5.4 a) shows the improved substrate coverage (yield) at higher temperatures. TEM investigations indicate that the majority of the grown tubes in region 1 are indeed DWCNT as shown in Figures 5.4 b-c. The mean CNT diameter as determined from in-depth TEM studies is $d_{CNT} = 4.0 \pm 1.1\,\mathrm{nm}$ (Fig. 5.4 d) which is only slightly larger than that of the starting catalyst particles, $d_P = 3.6 \pm 0.9\,\mathrm{nm}$. This again points to the catalyst particles templating the outer CNT diameters, similar to the findings for Fe and Co catalyst particles (cf. chapter 4). A statistical analysis reveals that approximately 60% of tubes are DWCNT (Fig. 5.4 e). The clear signature of the radial breathing modes between 100 and $350\,\mathrm{cm}^{-1}$ in Raman spectra obtained from these samples confirms the presence of SWCNT and/or DWCNT (Fig. 5.4 f). The

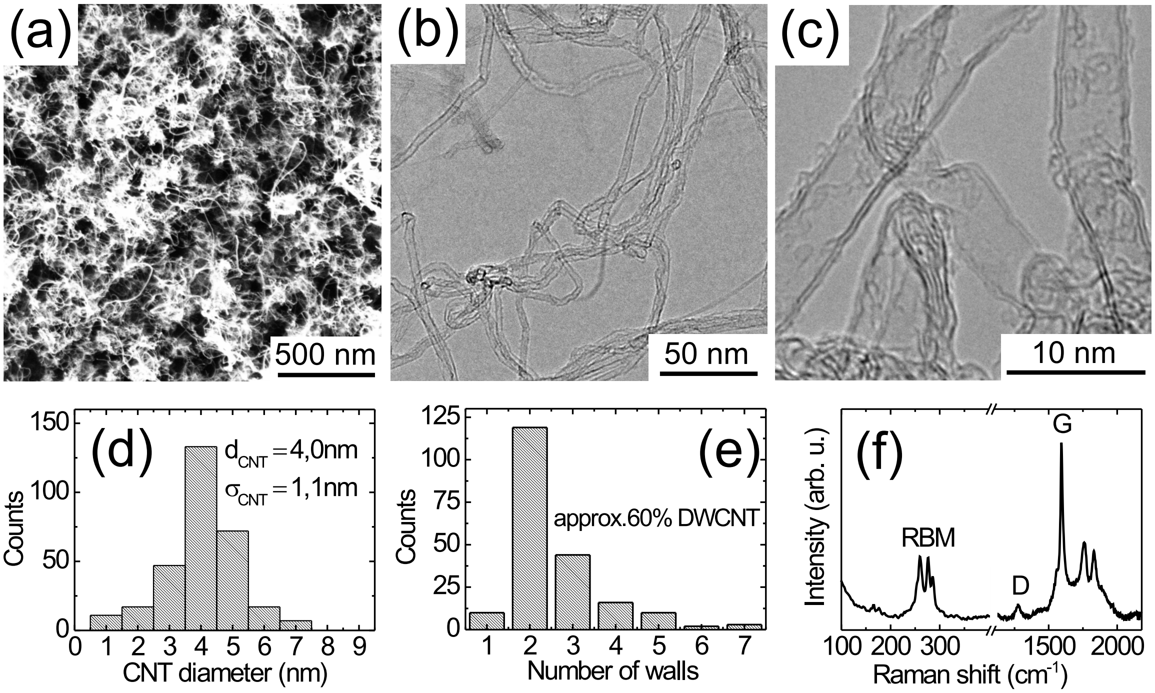

Figure 5.4: CNT grown from FePt at 660 °C with a high yield of DWCNT: a) SEM micrograph. b) TEM overview. c) HRTEM micrograph of double-wall CNT. d) Corresponding CNT diameter distribution. e) Corresponding distribution of the number of walls. f) Typical FT-Raman spectrum (1064 nm).

disorder mode (D) and the graphitic mode (G) at higher wave numbers also provide useful information. The narrow and well-defined G modes are characteristic of SWCNT and DWCNT. Further, the weak D mode indicates that the CNT are of good crystalline quality. The I_G/I_D ratio which is often used as an indicator for the quality of CNT is roughly 10.

From the onset of CNT growth at 590 °C to temperatures of about 680 °C, no significant change of the outer CNT diameter ($d_{CNT} \approx 4 \pm 1$ nm) is observed, thus highlighting the tailoring nature of the catalyst particle ($d_P \approx 3.5 \pm 1$ nm) throughout this wide temperature range. The CNT grown in this temperature range normally consist of 1 to a maximum of 7 walls with a clear preference of 2 walls further demonstrating the templating function of the catalyst particle.

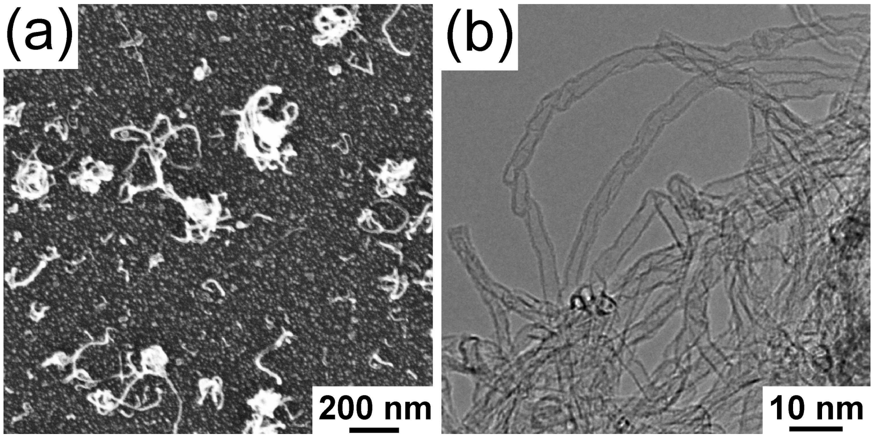

Figure 5.5: Multi-wall CNT: a) SEM micrograph of CNT grown at 745 °C; b) TEM micrograph of CNT grown at 725 °C.

In the second temperature region, 680°C ≤ T ≤ 800°C, the CNT diameter and number of walls are seen to increase non-linearly (cf. Fig. 5.2). Figure 5.5 presents a SEM micrograph and a TEM micrograph. Here, the grown tubes are predominantly MWCNT. Above 800 °C (region 3), however, the growth of very thick carbon nanostructures is observed. Examples of the growth products obtained in the high temperature region 3 are displayed in Figure 5.6. SEM and TEM overview images are shown in Figures 5.6 a-b, respectively. In Figure 5.6 c, the distribution of the diameters of these nanostructures is plotted. High-resolution TEM micrographs reveal structural details of these CNT heterostructures (Figs. 5.6 d-e). They consist of an inner MWCNT embraced by a thick amorphous carbon coating as schematically illustrated in Figure 5.6 f. The thickness of the outer amorphous carbon layer increases with increasing process temperature, hereby offering the inherent potential to tailor these novel MWCNT reinforced carbon fibres to specific needs. The upper temperature limit of CNT growth via thermal CVD from pre-defined FePt nanoparticles is mainly determined by the onset of decomposition of the carbon source. It is widely accepted that thermal decomposition (pyrolysis) of the carbon source leads to a deposition of amorphous carbon species on the sample at high synthesis temperatures. For cyclohexane, pyrolysis sets in at 750 °C and grows massively at 800 °C in a non-oxidizing atmosphere. Ethylene, butadiene, and carbon are

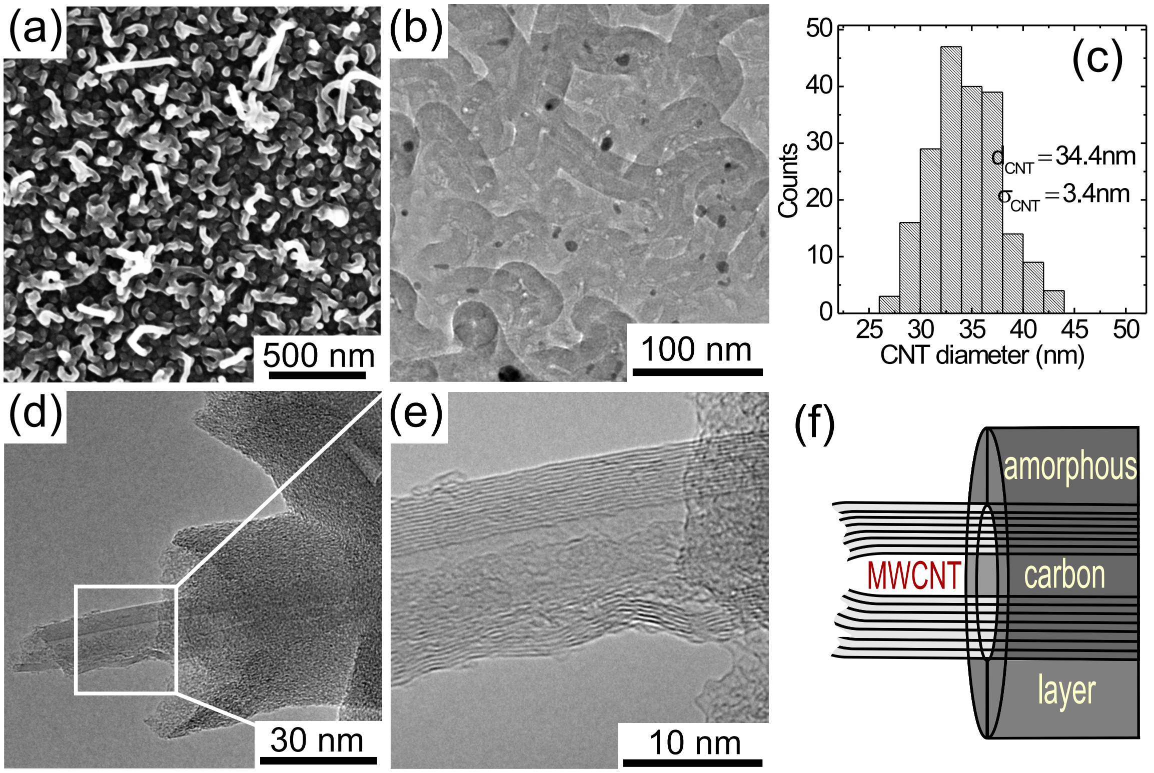

Figure 5.6: Carbon heterostructures grown at 830 °C: a) SEM micrograph. b) TEM overview. c) Corresponding outer diameter distribution. d, e) HRTEM micrographs revealing the structure of the CNT heterostructures. f) Schematic illustration of these nanostructures

the main decomposition products [168]. This explains the formation of this novel type of nanostructures at temperatures above 800 °C consisting of a MWCNT with a thick amorphous carbon coating. This temperature thus represents the upper limit for the synthesis of "clean" MWCNT in this approach.

Although FePt has rarely been studied for CNT catalysis, these experiments clearly demonstrate the versatility of FePt-catalyzed thermal CVD. The detailed data on the CNT morphologies, and the dependence of the CNT diameters and numbers of walls on the process temperature is very instructive. For temperatures below 680 °C (region 1) the mean CNT diameter is stable due to the catalyst particles templating the CNT diameter in a base growth mechanism. However, above 680 °C the mean diameter increases rapidly. The latter is attributed to the carbon feed-rate: At higher temperatures, the decomposition of the carbon feedstock is more efficient thus boosting the availability of free carbon, i.e. the carbon feed-rate to the catalyst is enhanced. As a consequence, the number of caps forming during nucleation increases and so does the number of walls as observed in temperature region 2. The presented data further validate the volume-to-surface ratio model for CNT nucleation [52]. As demonstrated in chapter 4.2.1 this model can be translated to supported catalyst CVD in that the catalyst particle templates the outer diameter of the CNT and that the number of caps formed depends on the volume-to-surface area ratio. From the model, as proposed for floating catalysts, it is also predicted that the number of caps (hence the number of walls) formed at nucleation also depends on the carbon feed rate [52]. It is also possible that particle coalescence increases at higher temperatures, however the microscopy data from particles formed at temperatures above 800 °C suggest that this is not the dominant process [166]. The formation of the MWCNT reinforced carbon fibres (region 3) is simply a consequence of the carbon feed-rate increasing beyond that which a catalyst particle can sustain such that the excess carbon deposits and grows on the surface of the MWCNT.

Within the present studies, very few FePt catalyst particles are found to reside at the ends of the CNT which implies that they grow via base growth similar to the pre-defined Fe particles (cf. Fig. 2.9 b). Hence, in order to facilitate the fabrication of CNT with hard-magnetic particles at their tips the CVD method itself was changed hereon. Since plasma-enhanced CVD inherently yields tip-grown CNT the latter is most promising for the realization of hard-magnetically terminated CNT.

5.2 Hard-magnetically terminated CNT from PE-CVD

For CNT synthesis via PE-CVD, three different types of FePt catalysts were utilized, namely gas phase prepared FePt nanoparticles, Fe/Pt multilayer thin films, and wet-chemically prepared stoichiometric FePt nanoparticles.

The attempt to grow CNT from pre-defined gas-phase prepared FePt nanoparticles resulted in the growth of irregular structures of very short CNT. Pyramidal columns with lengths of approx. 150 nm which most likely are Si/SiO$_2$-columns that form during the plasma treatment can be seen in the SEM micrograph (Fig. 5.7 a). Apparently the CVD substrate is etched during the PE-CVD process with the ensemble of catalyst particles acting as etching mask. CNT could only be recognized using HRTEM as depicted in Figures 5.7 b-c. The CNT are strongly entangled and are never observed to be longer than 50 nm. The FePt nanoparticles appear to reside at the CNT tip (Figs. 5.7 a-c). Some nanoparticles show characteristic lattice fringes of the hard-magnetic $L1_0$ phase. As an example the {110} lattice planes of $L1_0$-FePt are marked in Figure 5.7 c.

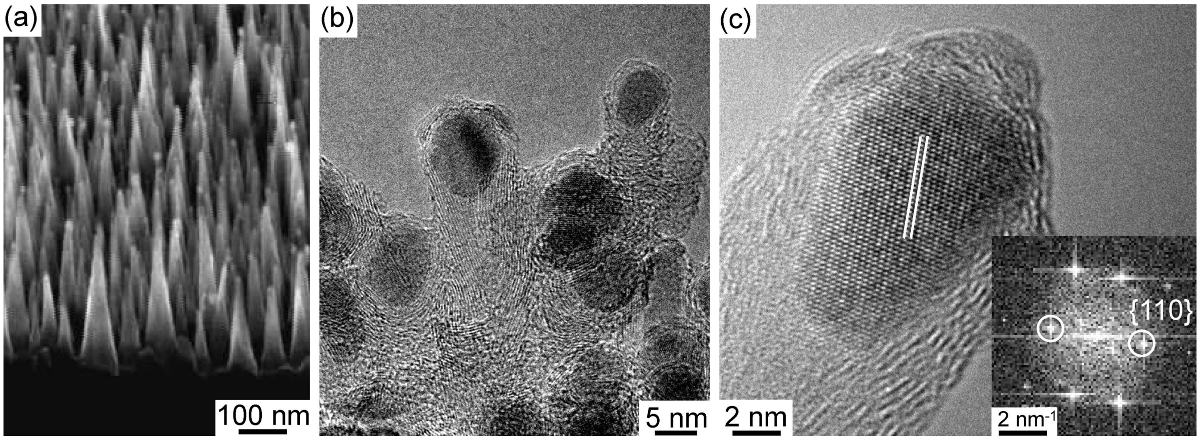

Figure 5.7: SEM and TEM micrographs of CNT grown from gas-phase prepared FePt nanoparticles via PE-CVD.

Parallel to the CNT growth via PE-CVD from gas-phase prepared nanoparticles, the use of both Fe/Pt multilayer thin films and wet-chemically prepared FePt nanoparticles as catalysts was examined. With these alternative catalysts an optimization of the PE-CVD conditions results in the growth of well-aligned CNT with the catalyst particle residing at the tip of the CNT. Figure 5.8 a shows a typical SEM micrograph as obtained from CNT grown via PE-CVD from Fe/Pt multilayer films. The CNT product is highly homogeneous, and the CNT are well-aligned perpendicular to the CVD substrate. Figure 5.8 b shows the material contrast of the identical sample area as obtained from

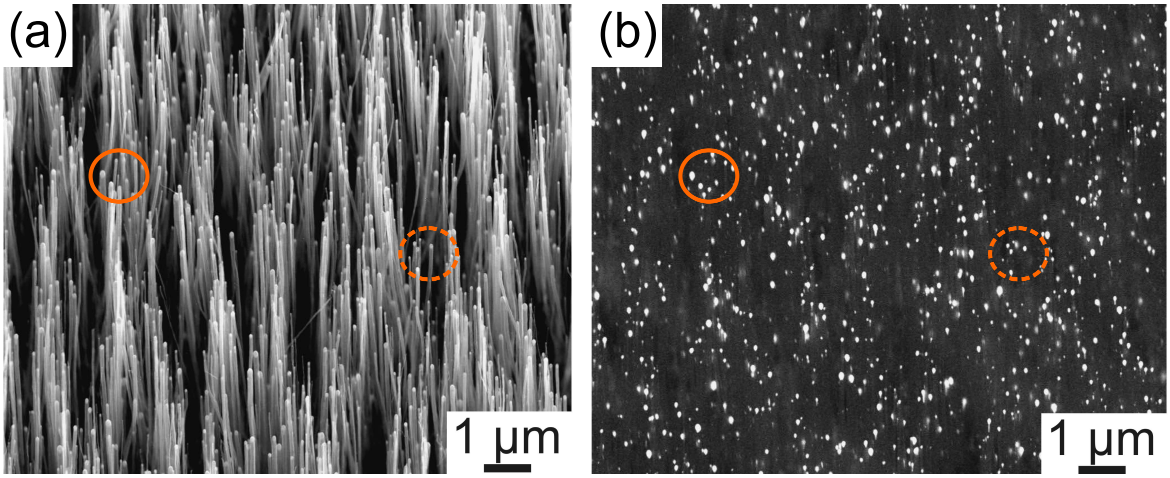

Figure 5.8: SEM micrographs of FePt-terminated CNT: a) Topography image. b) Materials contrast.

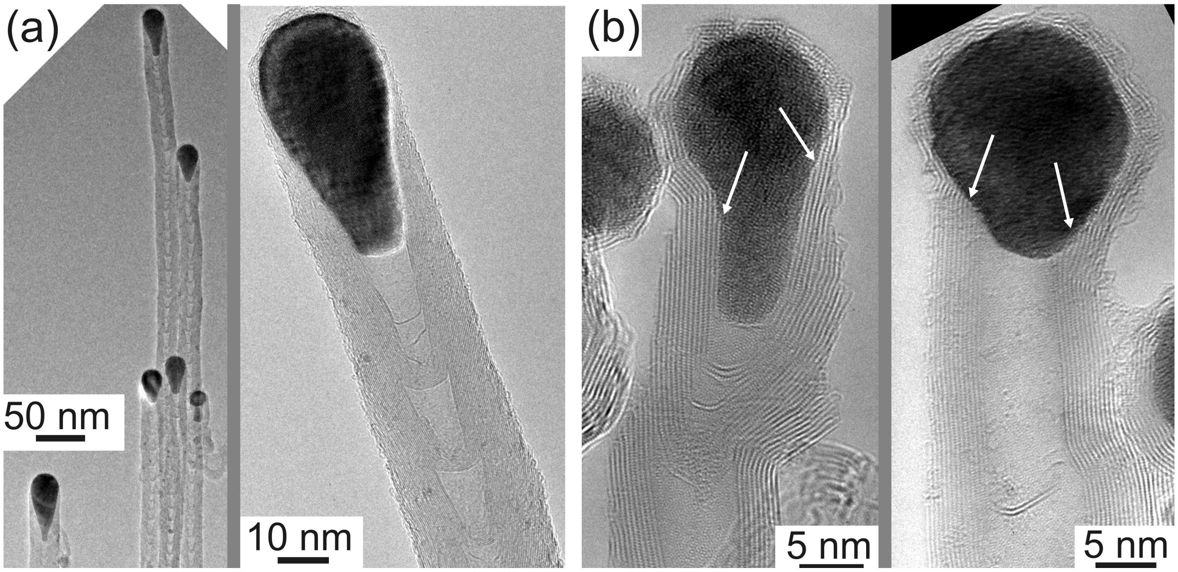

Figure 5.9: TEM micrographs of FePt-terminated CNT: a) CNT grown from wet-chemically prepared FePt nanoparticles. b) CNT grown from a 1 nm Fe/0.5 nm Pt multilayer thin film.

imaging with back scattered electrons only. The brighter the image, the higher is the atomic number of the material in that part of the sample. Two areas are highlighted in both images, clearly demonstrating that each CNT is terminated with a single FePt nanoparticle.

Figure 5.9 shows typical TEM micrographs of the as-produced CNT grown from wet-chemically prepared FePt nanoparticles (Fig. 5.9 a) as well as from Fe-Pt multilayer thin films (Fig. 5.9 b). The CNT obtained from both catalyst types exhibit similar bamboo-like, sometimes almost tubular structures with a varying number of bamboo segments typical for PE-CVD grown CNT [169]. The FePt nanoparticles always reside at the tip of the CNT. The graphitic CNT walls originate at the catalyst particle (marked by arrows in Fig. 5.9 b) thus indicating that the carbon incorporation occurs at the CNT tip due to tip growth (cf. Fig. 2.9 a).

Low voltage high resolution transmission electron microscopy (LV-HRTEM) was carried out to confirm the presence of the hard-magnetic $L1_0$ phase in the FePt nanoparticles. Figures 5.10 a-b show typical FePt nanoparticles terminating the CNT as grown from a 1 nm Fe / 0.5 nm Pt thin film catalyst. The FePt crystal structure was determined from fast Fourier transforms (FFT) of selected areas within the catalyst particles in the HRTEM images (see marked areas in Figs. 5.10 a-b). The FFTs depicted in Figures 5.10 a'-b' clearly reveal that the particles are in the $L1_0$ phase. The reflexes marked by squares are the so-called superstructure reflexes belonging to the $\{001\}$, $\{110\}$ and $\{201\}$ lattice fringes, that only appear in chemically ordered $L1_0$-FePt. The reflexes marked by circles belong to the $\{200\}$ and $\{202\}$ planes, that appear in ordered as well as disordered stoichiometric FePt. A large amount of FePt nanoparticles revealed the $L1_0$ superstructure reflexes. This clearly demonstrates the successful fabrication of hard-magnetically terminated CNT. Further, it has been found that there is no preferred orientation of the [001] easy axis of magnetization of $L1_0$-FePt with respect to the CNT growth direction. In the particle depicted in Figure 5.10 a, the [001] direction lies per-

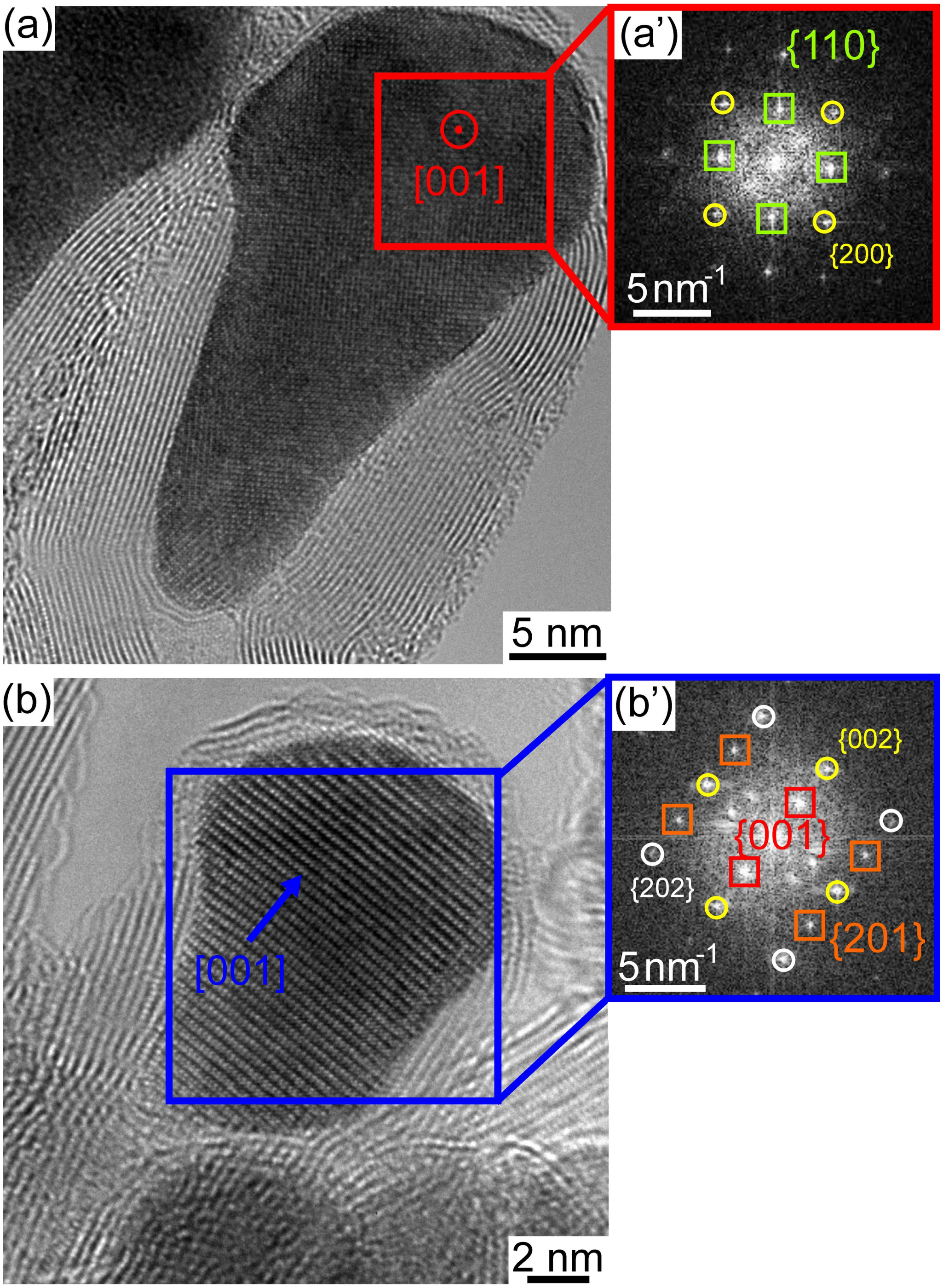

Figure 5.10: Hard-magnetically terminated CNT as grown from a 1 nm Fe / 0.5 nm Pt thin film: a, b) High resolution TEM micrographs of two exemplary FePt nanoparticles at the CNT tip. The corresponding fast Fourier transforms (a', b') reveal that the particles are in the $L1_0$ phase. The $L1_0$ superstructure reflexes belonging to the {001}, {110} and {201} lattice fringes are marked with squares. The reflexes marked with circles belong to the {002} and {202} planes and appear in both ordered ($L1_0$) as well as disordered ($A1$) stoichiometric FePt.

pendicular to the image plane, whereas in the particle shown in Figure 5.10 b, the [001] direction is parallel to the CNT growth direction [154].

The observation of $L1_0$-FePt nanoparticles in these experiments is remarkable in that the film thickness ratio of 2 Fe : 1 Pt as used here provides a strongly over-stoichiometric Fe content within the starting catalyst material (approx. 72 at-% Fe). However, from a quantitative analysis of various EDX spectra, the elemental composition of the FePt nanoparticles at the CNT tips was determined to be 50 ± 4 at-% Fe or Pt, i.e. close to the stoichiometric composition and thus always lay well within the stability range of the FePt-$L1_0$ phase, i.e. 35 to 55 at-% Pt. The compositional readjustment towards stoichiometric FePt, as observed from EDX, most likely results from a preferential evaporation of Fe during the PE-CVD process. During the thermal treatment of the FePt thin films at temperatures above 800°C, the preferential evaporation of Fe is known to become an important effect that cannot be neglected for FePt phase formation [170]. Since Fe is the first layer deposited onto the thermally oxidized Si substrate, it is also possible that some Fe dissolves into the substrate during the PE-CVD process, possibly even leading to iron silicide formation [171; 172].

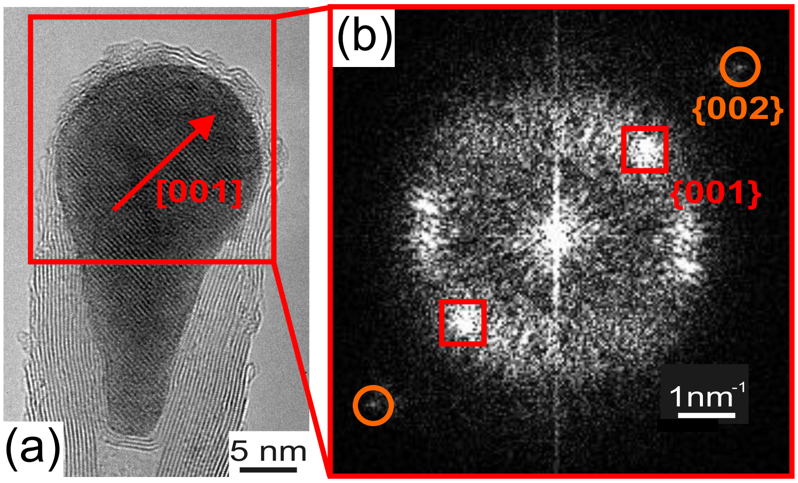

Figure 5.11: a) HRTEM micrograph of a hard-magnetically terminated CNT as grown from wet-chemically prepared FePt nanoparticles. b) Corresponding FFT revealing that the particle exhibits the $L1_0$ superstructure.

Figure 5.11 a shows a FePt-terminated CNT as grown from wet-chemically prepared FePt nanoparticles. The corresponding FFT is depicted in Figure 5.11 b and reveals superstructure reflexes belonging to the {001} lattice fringes which only appear in the ordered $L1_0$ phase. In samples grown from wet-chemically prepared FePt nanoparticles, only a small number of particles terminating the CNT was found to be in the $L1_0$ phase, thereby confirming that the previously suggested scenario of a preferential Fe evaporation during CNT growth.

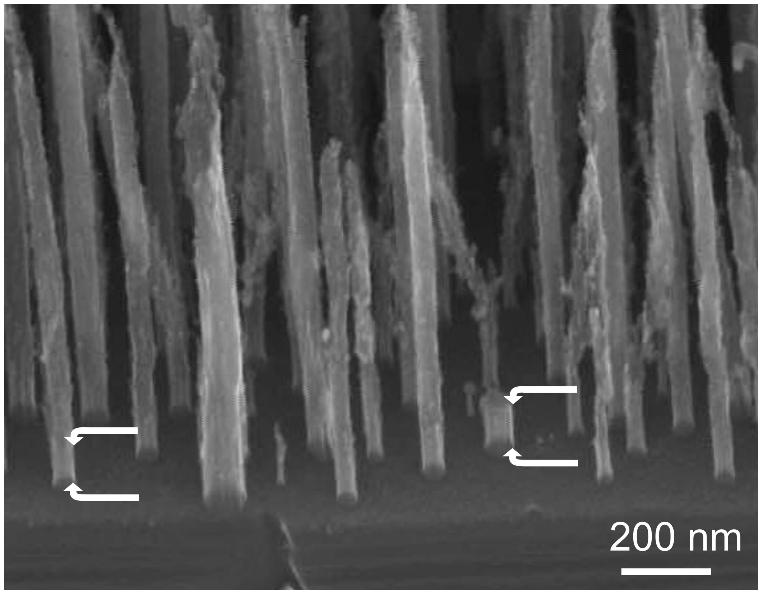

Figure 5.12: SEM micrograph of CNT roots at the substrate showing that no catalyst material remains at the substrate during CNT growth.

Since HRTEM allows for the analysis of a very small sample volume only, an additional magnetic characterization of the bulk sample is carried out through vibrating sample magnetometry (VSM). In order to make sure that the measured magnetic signal stems from the catalyst material at the CNT tip and *not* from any residual catalyst material on the substrate, the CNT have been lifted off the substrate and glued to the VSM sample holder prior to the VSM measurement (see chapter 3.4.3 for details of the preparation procedure). Further, the CNT often root on Si/SiO_2 columns that form during the H_2-plasma pre-treatment as reported by Täschner et al. [59]. Also in the present SEM images it is often observed that the substrate surface around the catalyst is sputtered away during plasma treatment and that the CNT themselves seem to root on more rigid Si/SiO$_2$ columns. In Figure 5.12 two of these columns are marked with arrows. An analysis using back scattered electrons also proves that no catalyst material remains at the substrate surface.

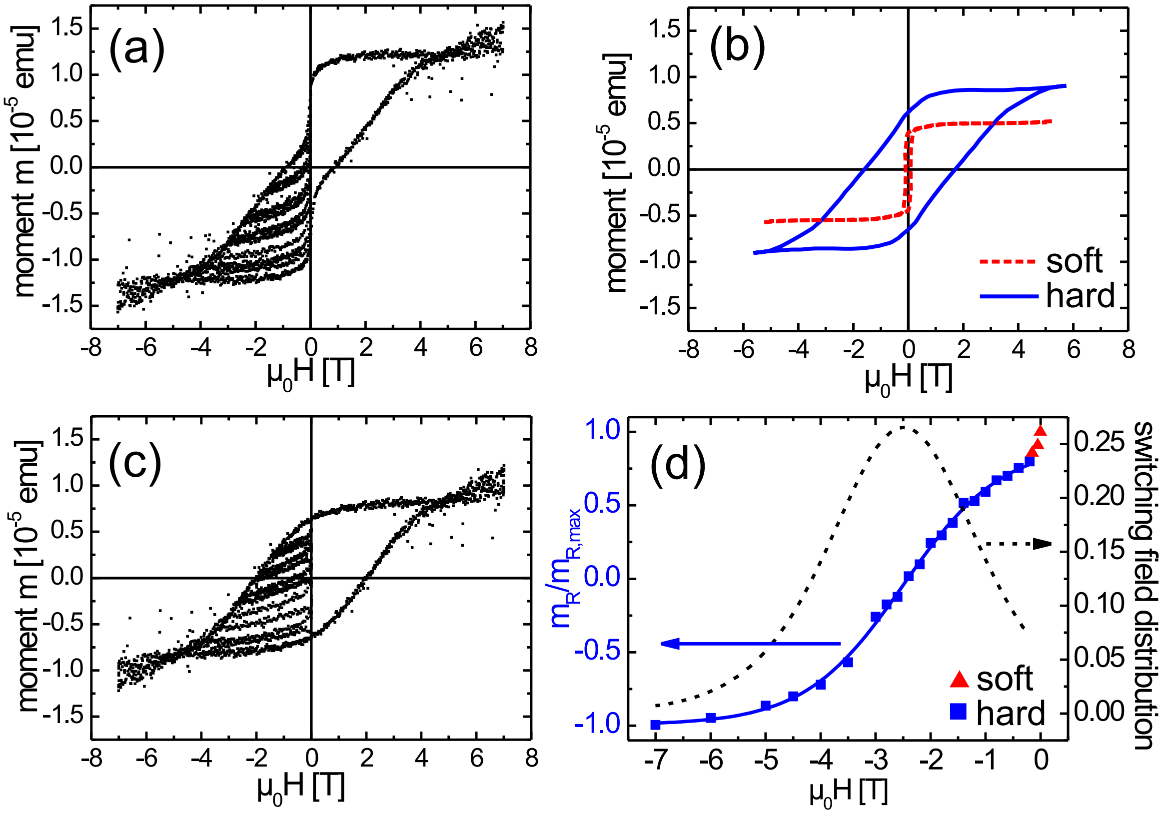

Figure 5.13: a) RT magnetization curve and selected recoil loops of the hard-magnetically terminated CNT as grown from a 1 nm Fe / 0.5 nm Pt thin film. b) The magnetic signal consists of a hard-magnetic (blue full line) and a soft magnetic contribution (red dashed line). c) Magnetization curve after correction for the soft magnetic contribution. d) Remanence analysis and switching field distribution for the hard-magnetically terminated CNT. (The red triangular data points are ascribed to the soft magnetic part of the signal and are not accounted for in the determination of the switching field distribution.)

Figure 5.13 a shows the full magnetization curve of the FePt-terminated CNT grown from the 1 nm Fe / 0.5 nm Pt thin film catalyst as measured at room temperature (RT) together with selected recoil loops. The measured ferromagnetic signal is comprised of hard and soft magnetic subsignals as schematically highlighted in Figure 5.13 b. The hysteresis loop indicates that a significant amount of the FePt particles terminating the CNT is in the hard magnetic $L1_0$ phase after the CNT growth via PE-CVD. However, some FePt nanoparticles are magnetically soft and are thus to be assumed to exhibit the $A1$-FePt phase. In Figure 5.13 c, the RT magnetization curve has been corrected for this soft magnetic contribution such that only the hard magnetic part remains. The coercivity of the ensemble of hard magnetic particles is determined to be $\mu_0 H_C = 2\,\mathrm{T}$. Figure 5.13 d summarizes the normalized remanent moments $m_R/m_{R,max}$ of this hard magnetic contribution as function of the previously applied demagnetizing field (blue squares). Here, $m_{R,max}$ denotes the maximum remanent moment of the hard-magnetic contribution remaining after saturation. The triangular red data points have not been included in the later switching field analysis, as they are to be ascribed to the soft-magnetic contribution. The switching field distribution (dashed line) as derived from the derivative of the normalized remanent moment with respect to the field

$$\frac{1}{2} \cdot \frac{\partial (m_R/m_{R,max})}{\partial H} \tag{5.1}$$

is slightly asymmetric with a most prevalent switching field of $\mu_0 H = 2.5\,\mathrm{T}$ in good agreement with the coercivity of the hard magnetic particle ensemble.

These high switching fields are a direct consequence of the large uniaxial anisotropy that goes along with the good chemical $L1_0$ order in these nanomagnets. They ensure that the magnetization of the FePt nanoparticles is stable, for example during scanning a likewise hard magnetically terminated CNT in magnetic force microscopy and under an applied external field. The broad magnetic hysteresis is further proof that the FePt-CNT hybrid material contains a large amount of hard magnetically terminated CNT [154].

For comparison, the corrected RT magnetization curve of the FePt-terminated CNT grown from wet-chemically prepared FePt nanoparticles is shown in Figure 5.14 a together with selected recoil loops. Also here the original raw data contain a soft-magnetic contribution which is again substracted. The coercivity of the ensemble of hard-magnetic particles is determined to be $\mu_0 H_C = 1.2\,\mathrm{T}$. The normalized remanent moments of the hard-magnetic contribution are shown as function of the previously applied demagnetizing field in Figure 5.14 b. The most prevalent switching field of this sample is $\mu_0 H = 1.2\,\mathrm{T}$ and is again in agreement with the coercive field. This somewhat lower switching field as compared to that of the CNT grown from Fe/Pt multilayer catalyst thin films is consistent with the TEM analysis which had revealed a lower number of $L1_0$-ordered particles at CNT grown from wet-chemically prepared FePt nanoparticles.

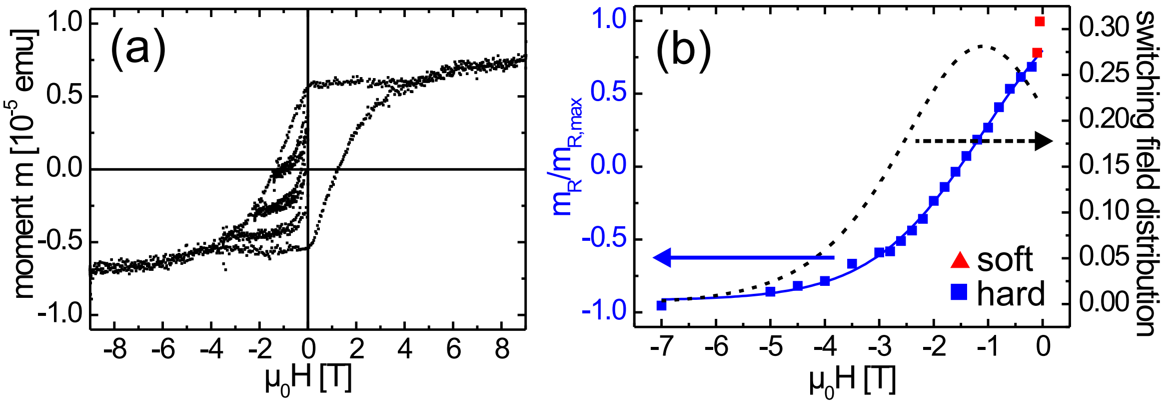

Figure 5.14: a) RT magnetization curve and selected recoil loops of the hard magnetically terminated CNT from wet chemically prepared FePt nanoparticles after correction for the soft magnetic contribution. b) Remanence analysis and switching field distribution for the hard magnetically terminated CNT.

To summarize, the fabrication of hard-magnetically terminated CNT is demonstrated using Fe/Pt thin film catalysts as well as wet-chemically prepared FePt nanoparticles in a plasma-enhanced CVD process. The CNT are aligned perpendicular to the substrate, and each CNT is terminated with a FePt nanomagnet.

6 Summary and outlook

The main objective of the present thesis is to deepen the understanding of the mechanisms involved in catalytic CNT growth and related processes such as, e.g., the catalytic hydrogenation, and to use this knowledge to optimize the experimental approaches in order to gain better control in the synthesis and modification of carbon nanomaterials.

The majority of CNT synthesis experiments herein utilize *pre-defined gas-phase prepared catalyst particles.* The gas phase route allows for the preparation of very clean and well defined individual catalyst particles with a narrow size distribution and holds the potential to independently vary both the catalyst size *and* density. These particles then serve as individual catalytic nucleation sites for CNT growth in a subsequent CVD process. The separate generation of nanoparticles and their simultaneous deposition on TEM witness grids facilitates their comprehensive characterization *prior* to the CVD process and is highly advantageous over thin film catalysts where the "catalyst particles" form *in-situ.* Due to the ease with which detailed information on the catalysts' size distribution and dispersion can be accessed, the technique provides improved insight into the CNT growth via CVD.

For conventional Fe and Co nanoparticles which are deposited onto Al_2O_3-coated Si/SiO_2 supports, direct correlations between the particle and the CNT densities as well as between the sizes of the catalyst particles and of the resultant CNT diameters are demonstrated. The latter is shown to go along with a clear correlation between the number of walls of the CVD-synthesized CNT and the primary catalyst size. For Fe nanoparticles, the CNT diameter almost precisely matches that of the catalyst particle. In the case of the Co particles, the CNT diameters as well as the mean number of graphitic walls are slightly smaller as compared to CNT grown from Fe catalysts which is attributed to the reduced solubility of carbon in Co as compared to Fe.

Future research should involve the optimization of the particle preparation towards the growth of *thin*-walled CNT with fully tailored diameters. Thus far, the smallest Fe particles prepared by the gas-phase preparation route had a mean particle diameter d_P of 3 nm, resulting in the predominant growth of DWCNT and TWCNT. Smaller catalyst particles should in principle allow for the growth of smaller diameter SWCNT and DWCNT. In addition, the particle diameter distribution may be further tailored by means of quadrupole mass filtering, possibly allowing to synthesize CNT of one type, i.e. SWCNT or DWCNT.

Although the mean particle diameter and the diameter distributions are comparable for Fe and Co catalyst particles used in this study, the structure and morphology of the CNT products vary significantly. CNT grown from Fe hardly contain any catalyst material after detachment from the substrate thereby implying a base growth mechanism with the catalyst residing at the substrate during the CNT growth. In contrast, CNT grown from Co particles include a lot of catalyst material. Here, the catalyst particles reside at basically any position in the CNT cores, often very close to their capped ends. In general, the Co catalyst material is fully encapsulated by the same number of graphitic walls the nanotube is composed of indicating that the Co particle resides within the CNT's graphitic walls throughout the entire growth process. Like in the case of Fe catalyst particles this points to the CNT base growth mode, however, with the catalyst particle lifting off the substrate due to a weaker particle-substrate interaction as compared to Fe.

The experimentally derived correlations between the particle diameter on one hand and the CNT diameter and the CNT number of walls on the other hand are attributed to an increase of the catalyst's volume-to-surface area ratio with increasing particle size: while the availability of carbon dissolved within the catalyst at the point of nucleation is determined by the catalyst volume, the amount of carbon required to form a cap depends on the surface area of the catalyst particle. The present findings thus support the *volume-to-surface area nucleation model* which was originally developed for CNT synthesized in laser ablation [52].

Further, conventional CNT growth models are insufficient in that they can not explain many of the recent experimental results as for example the "catalyst-free" CNT synthesis. However, in many of these studies, oxygen tends to play a significant role in the success of these growth experiments. Within the present thesis, thorough HRTEM investigations of CNT grown from Fe nanoparticles are carried out to characterize the catalyst/substrate/carbon interfaces. These investigations reveal that the CNT walls are anchored to the oxide substrate. This is remarkable in that it is generally argued that the CNT walls stem from atomic steps at the catalyst which are the points of carbon incorporation. Based on the present experimental findings, however, it is assumed that after nucleation, the CNT links to an oxygen site thereby stabilizing the growth position which finally leads to the growth of CNT with parallel walls. Here, the substrate itself provides a catalytic functionality towards the stimulation of ongoing CNT growth, whereas the catalytic activity of the metal particle is more restricted to the nucleation process. The catalytic graphitization of carbon by oxides is well known [149]. On the basis of these findings a novel, *substrate-driven growth* concept is introduced. Here, the interface between the catalyst particle surface and the substrate, i.e. the circumferential line around the particle on the substrate, provides a circular defect site, that may then anchor the CNT to the substrate and enable carbon incorporation.

Future studies will however be required to prove this concept, e.g. by virtue of the deliberate creation of defects on oxide substrates. In fact, preliminary CVD experiments conducted by A. Bachmatiuk (IFW Dresden) without metal catalyst, utilizing solely SiO_2 substrates which are heat-treated in air or Argon prior to the thermal CVD process, reveal the formation of MWCNT [173]. These MWCNT seem to be more defective as compared to CNT grown from a metal catalyst particle, supporting the above proposed scenario that the metal catalyst actually provides an effective CNT diameter control during cap nucleation.

Comparative studies on the influence of the CVD substrate show that the use of non-oxide supports, i.e. TiN and graphite, leads to a qualitatively different tube formation. While CNT grown on the standard Al_2O_3-coated Si/SiO_2 supports are in general composed of parallel walls almost along their entire length with little structural disorder (particularly when using Fe as the catalyst) the use of non-oxide supports results in the formation of non-uniform structures containing many pockets, that are stacked upon each other (bamboo-like). Also, CNT grown on TiN and graphite have much larger diameters which are not correlated with the size of the pristine catalyst particles. This is due to enhanced particle coalescence during the CVD process on these non-oxide substrates thereby indicating that the particle-substrate interaction is weaker for these supports.

The (hard-)magnetic functionalization of CNT opens exciting opportunities to design novel nanoscale devices with magnetic functionality. Although FePt has hardly been used as catalyst for CNT synthesis it is of great interest due to the large magneto-crystalline anisotropy of the chemically ordered $L1_0$ phase. In order to investigate if the use of FePt catalysts facilitates the hard-magnetic functionalization of CNT tips, FePt catalysts have been utilized in thermal and plasma enhanced CVD experiments.

Systematic studies were carried out to explore the growth of CNT from gas-phase prepared FePt nanoparticles via thermal CVD. These investigations show strong changes in the CNT structure, diameter and their density on the CVD substrate depending on the CVD furnace temperature [166]. The investigated temperature range can be roughly divided into three temperature regions. At low temperatures of $590°C \leq T \leq 680°C$, large amounts of DWCNT are obtained with highest yields at 660°C. The mean outer CNT diameter is slightly larger than that of the starting catalyst particles confirming the templating function of the catalyst particles, similar to the findings for Fe and Co catalyst particles. The second region ($680°C \leq T \leq 800°C$) is characterized by the growth of

MWCNT whose outer diameter increases with increasing temperature. At temperatures above 800°C coaxial CNT heterostructures are obtained, consisting of a MWCNT core embraced by a thick amorphous carbon coating. The formation of the carbon coating is ascribed to thermal decomposition of the carbon feedstock and subsequent re-deposition of amorphous carbon species on the MWCNT.

Within the studies using gas-phase prepared FePt nanoparticles in thermal CVD, only few FePt catalyst particles are found to reside at the ends of the CNT implying a base-growth mechanism similar to the findings from Fe catalyst particles. However, in order to facilitate the fabrication of CNT with hard-magnetic particles at their tips, plasma-enhanced CVD from FePt catalysts is carried out. Indeed, FePt terminated CNT grow from gas-phase prepared FePt nanoparticles, Fe/Pt multilayer thin films, *and* wet-chemically prepared FePt nanoparticles. While the use of gas-phase prepared FePt nanoparticles yields only very short CNT, CNT grown from Fe/Pt thin films and from wet-chemically prepared FePt particles are observed to be longer and well-aligned perpendicular to the PE-CVD substrate, and each CNT is terminated with a single FePt nanoparticle. As observed in HRTEM studies, stoichiometric wet-chemically prepared FePt nanoparticles yield FePt-terminated CNT with only few nanoparticles in the $L1_0$ phase. Yet, Fe/Pt thin films with a strongly over-stoichiometric Fe content in the starting catalyst composition generate CNT with a significantly larger number of particles in the $L1_0$ phase. This is confirmed by ensemble magnetization measurements: the most prevalent switching field of $\mu_0 H = 2.5\,\mathrm{T}$ as obtained from the Fe/Pt thin film samples is substantially higher than that of the samples utilizing stoichiometric nanoparticles ($\mu_0 H = 1.2\,\mathrm{T}$). The elemental composition of the FePt nanoparticles at the CNT grown from over-stoichiometric thin film catalysts is determined to be close to the stoichiometric composition, suggesting that a compositional readjustment towards stoichiometric FePt through preferential iron evaporation occurs during the PE-CVD process. Thus, further experiments with FePt catalyst nanoparticles should utilize particles with an over-stoichiometric Fe content in order to fabricate a nanomagnet-CNT hybrid with comparable hard-magnetic properties.

Future research in this field can now be directed towards the realization of magnetic nanodevices. For example, the direct fabrication of a single hard-magnetically terminated CNT on a cantilever for the use as a tip in magnetic force microscopy should be possible. Therefore a Fe/Pt catalyst thin film can be lithographically structured to obtain a single catalyst dot. When subjected to PE-CVD, a localized growth of a single hard-magnetically terminated CNT on the cantilever may be achieved.

Investigations of the catalytic hydrogenation of graphite in a hydrogen atmosphere using gas-phase prepared Co catalyst particles have been conducted. The general picture, i.e. the anisotropic etching of graphite through catalyst particles residing at an exposed graphite edge, is confirmed in the present investigations. However, in previous studies etching along the $\langle 11\bar{2}0 \rangle$ directions was favored [22]. In the present study, the preferred etching direction is found to be along $\langle 10\bar{1}0 \rangle$. This may provide a means to tailor graphene nanostructures with specific edge termination. Here, future work should include the analysis of the "true" edge structure of these nanostructures in order to understand the potential of catalytic hydrogenation for the precise cutting of graphene and to evaluate the degree of control that can be achieved via this approach.

HRTEM investigations on catalyst particles which rest on flat basal graphite planes, i.e. etch-inactive particles, provide information regarding the hydrogenation mechanism which is, similar to the CNT growth mechanism, still a matter of controversy. The two disputed mechanisms, i.e. the interfacial hydrogen and the carbon dissolution mechanism, basically argue either hydrogen or carbon diffusion through the catalyst particle during the hydrogenation process [23]. The etch-inactive particles are found to be reduced during H_2 treatment and fully or partly re-oxidize during sample transfer in air. Since the bulk hydrogen permeation rate is much higher than that for carbon, hydrogen effectively penetrates the particle and thereby prevents carbon from dissolving within the particles. Therefore, the observation of re-oxidized particles points against the carbon dissolution mechanism and corroborates the interfacial hydrogen mechanism. In contrast, catalyst particles which are treated in H_2 and post-annealed in vacuum for 5 min do not re-oxidize but show graphitic encapsulations. Thus, if carbon is within the reach of the catalyst particle and has enough time to dissolve in the particle, which is provided by the post-annealing step in this case, the particle can be protected against re-oxidation.

List of Figures

Bibliography

[1] R. Saito, G. Dresselhaus, and M. S. Dresselhaus, *Physical Properties of Carbon Nanotubes*. Imperial College Press, London, 1998.

[2] H. W. Kroto, J. R. Heath, S. C. O'Brien, R. F. Curl, and R. E. Smalley, "C_{60}: Buckminster-fullerene," *Nature*, vol. 318, pp. 162–163, 1985.

[3] S. Iijima, "Helical microtubules of graphitic carbon," *Nature*, vol. 354, pp. 56–58, 1991.

[4] L. V. Radushkevich and V. M. Lukyanovich, "O strukture ugleroda, obrazujucegosja pri termiceskom razlozenii okisi ugleroda na zeleznom kontakte," *Zurn. Fisic. Chim.*, vol. 26, pp. 88–95, 1952.

[5] R. Bacon, "Growth, structure, and properties of graphite whiskers," *J. Appl. Phys.*, vol. 31, pp. 283–290, 1960.

[6] A. Oberlin, M. Endo, and T. Koyama, "Filamentous growth of carbon through benzene decomposition," *J. Crystal Growth*, vol. 32, pp. 335–349, 1976.

[7] M. Cadek, J. N. Coleman, V. Barron, K. Hedicke, and W. J. Blau, "Morphological and mechanical properties of carbon-nanotube-reinforced semicrystalline and amorphous polymer composites," *Appl. Phys. Lett.*, vol. 81, pp. 5123–5125, 2002.

[8] E. Dujardin, V. Derycke, M. F. Goffman, R. Lefèvre, and J. P. Bourgoin, "Self-assembled switches based on electroactuated multiwalled nanotubes," *Appl. Phys. Lett.*, vol. 87, 193107, 2005.

[9] M. Zhang, K. R. Atkinson, and R. H. Baughman, "Multifunctional carbon nanotube yarns by downsizing an ancient technology," *Science*, vol. 306, pp. 1358–1361, 2004.

[10] M. José-Yacamán, M. Miki-Yoshida, L. Rendón, and J. G. Santiesteban, "Catalytic growth of carbon microtubules with fullerene structure," *Appl. Phys. Lett.*, vol. 62, pp. 657–659, 1993.

[11] C. J. Lee, J. Park, J. M. Kim, Y. Huh, J. Y. Lee, and K. S. No, "Low-temperature growth of carbon nanotubes by thermal chemical vapor deposition using Pd, Cr, and Pt as co-catalyst," vol. 327, pp. 277–283, 2000.

[12] A. Barreiro, S. Hampel, M. H. Rümmeli, C. Kramberger, A. Grüneis, K. Biedermann, A. Leonhardt, T. Gemming, B. Büchner, A. Bachtold, and T. Pichler, "Thermal decomposition of ferrocene as a method for production of single-walled carbon nanotubes without additional carbon sources," *J. Phys. Chem. B*, vol. 110, pp. 20973–20977, 2006.

[13] W. Z. Li, S. S. Xie, L. X. Qian, B. H. Chang, B. S. Zou, W. Y. Zhou, R. A. Zhao, and G. Wang, "Large-scale synthesis of aligned carbon nanotubes," *Science*, vol. 274, pp. 1701–1703, 1996.

[14] Y.-L. Li, I. A. Kinloch, and A. H. Windle, "Direct spinning of carbon nanotube fibers from chemical vapor deposition synthesis," *Science*, vol. 304, pp. 276–278, 2004.

[15] Z. F. Ren, Z. P. Huang, J. W. Xu, J. H. Wang, P. Bush, M. P. Siegal, and P. N. Provencio, "Synthesis of large arrays of well-aligned carbon nanotubes on glass," *Science*, vol. 282, pp. 1105–1107, 1998.

[16] J. Kong, H. T. Soh, A. M. Cassell, C. F. Quate, and H. Dai, "Synthesis of individual singlewalled carbon nanotubes on patterned siliconwafers," *Nature*, vol. 395, pp. 878–881, 1998.

[17] M. S. Kabir, R. E. Morjan, O. A. Nerushev, P. Lundgren, S. Bengtsson, P. Enoksson, and E. E. B. Campbell, "Fabrication of individual vertically aligned carbon nanofibres on metal substrates from prefabricated catalyst dots," *Nanotechnology*, vol. 17, pp. 790–794, 2006.

[18] D. Grimm, A. Grüneis, C. Kramberger, M. H. Rümmeli, T. Gemming, B. Büchner, A. Barreiro, H. Kuzmany, R. Pfeiffer, and T. Pichler, "Catalytic decomposition of n-heptane for the growth of high quality single wall carbon nanotubes," vol. 428, pp. 416–420, 2006.

[19] J. Gavillet, A. Loiseau, C. Journet, F. Willaime, F. Ducastelle, and J.-C. Charlier, "Root-growth mechanism for single-wall carbon nanotubes," *Phys. Rev. Lett.*, vol. 87, 275504, 2001.

[20] J. W. Mintmire, B. I. Dunlap, and C. T. White, "Are fullerene tubules metallic?," *Phys. Rev. Lett.*, vol. 68, pp. 631–634, 1992.

[21] N. Hamada, S. Sawada, and A. Oshiyama, "New one-dimensional conductors: Graphitic microtubules," *Phys. Rev. Lett.*, vol. 68, pp. 1579–1581, 1992.

[22] A. Tomita and Y. Tamai, "An optical microscopic study on the catalytic hydrogenation of graphite," *J. Phys. Chem.*, vol. 22, pp. 2254–2258, 1974.

[23] C. W. Keep, S. Terry, and M. Wells, "Studies of the nickel-catalyzed hydrogenation of graphite," *J. Catal.*, vol. 66, pp. 451–462, 1980.

[24] S. S. Datta, D. R. Strachan, S. M. Kharnis, and A. T. C. Johnson, "Crystallographic etching of few-layer graphene," *Nano Lett.*, vol. 8, pp. 1912–1915, 2008.

[25] L. Ci, Z. Xu, L. Wang, W. Gao, F. Ding, K. F. Kelly, B. I. Yakobson, and P. M. Ajayan, "Controlled nanocutting of graphene," *Nano Res.*, vol. 1, pp. 116–122, 2008.

[26] L. C. Campos, V. R. Manfrinato, J. D. Sanchez-Yamagishi, J. Kong, and P. Jarillo-Herrero, "Anisotropic etching and nanoribbon formation in single-layer graphene," *Nano Lett.*, vol. 9, pp. 2600–2604, 2009.

[27] R. T. K. Baker, "Catalytic growth of carbon filaments," *Carbon*, vol. 27, pp. 315–323, 1989.

[28] D. Weller, A. Moser, L. Folks, M. E. Best, W. Lee, M. F. Toney, M. Schwickert, J.-U. Thiele, and M. F. Doerner, "High K_U materials approach to 100 Gbits/in^2," *IEEE Trans. Magn.*, vol. 36, no. 1, pp. 10–15, 2000.

[29] S. Sun, E. E. Fullerton, D. Weller, and C. B. Murray, "Compositionally controlled FePt nanoparticles materials," *IEEE Trans. Magn.*, vol. 37, no. 4, pp. 1239–1243, 2001.

[30] U. Müller, *Anorganische Strukturchemie.* B. G. Teubner Verlag, 3rd ed., 1996.

[31] K. S. Novoselov, A. K. Geim, S. V. Morozov, D. Jiang, Y. Zhang, S. V. Dubonos, I. V. Grigorieva, and A. A. Firsov, "Electric field effect in atomically thin carbon films," *Science*, vol. 306, pp. 666–669, 2004.

[32] A. K. Geim and K. S. Novoselov, "The rise of graphene," *Nature Mater.*, vol. 6, pp. 183–191, 2007.

[33] M. I. Katsnelson, "Graphene: carbon in two dimensions," *Materials today*, vol. 10, pp. 20–27, 2007.

[34] K. S. Novoselov, A. K. Geim, S. V. Morozov, D. Jiang, M. I. Katsnelson, I. V. Grigorieva, S. V. Dubonos, and A. A. Firsov, "Two-dimensional gas of massless dirac fermions in graphene," *Nature*, vol. 438, pp. 197–200, 2005.

[35] S. V. Morozov, K. S. Novoselov, M. I. Katsnelson, F. Schedin, D. C. Elias, J. A. Jaszczak, and A. K. Geim, "Giant intrinsic carrier mobilities in graphene and its bilayer," *Phys. Rev. Lett.*, vol. 100, 016602, 2008.

[36] X. Li, X. Wang, L. Zhang, S. Lee, and H. Dai, "Chemically derived, ultrasmooth graphene nanoribbon semiconductors," *Science*, vol. 319, pp. 1229–1232, 2008.

[37] B. Partoens and F. M. Peeters, "From graphene to graphite: Electronic structure around the K point," *Phys. Rev. B*, vol. 74, p. 075404, 2006.

[38] S. V. Morozov, K. S. Novoselov, F. Schedin, D. Jiang, A. A. Firsov, and A. K. Geim, "Two-dimensional electron and hole gases at the surface of graphite," *Phys. Rev. B*, vol. 72, 201401, 2005.

[39] D. S. Bethune, C. H. Kiang, M. S. de Vries, G. Gorman, R. Savoy, J. Vazquez, and R. Beyers, "Cobalt catalysed growth of carbon nanotubes with single-atomic-layer walls," *Nature*, vol. 363, pp. 605–607, 1993.

[40] S. Iijima and T. Ichihashi, "Single-shell carbon nanotubes of 1-nm diameter," *Nature*, vol. 363, pp. 603–605, 1993.

[41] C. Kramberger, *Angle resolved dielectric response in carbon nanotubes.* Dissertation, TU Dresden, 2008.

[42] K. Hata, D. N. Futaba, K. Mizuno, T. Namai, M. Yumura, and S. Iijima, "Water-assisted highly efficient synthesis of impurity-free single-walled carbon nanotubes," *Science*, vol. 306, pp. 1362–1364, 2004.

[43] T. W. Ebbesen, H. J. Lezec, H. Hiura, J. W. Bennett, H. F. Ghaemi, and T. Thio, "Electrical conductivity of individual carbon nanotubes," *Nature*, vol. 382, pp. 54–56, 1996.

[44] T. Guo, P. Nikolaev, A. Thess, D. T. Colbert, and R. E. Smalley, "Catalytic growth of single-walled nanotubes by laser vaporization," vol. 243, pp. 49–54, 1995.

[45] M. H. Rümmeli, E. Borowiak-Palen, T. Gemming, T. Pichler, M. Knupfer, M. Kalbác, L. Dunsch, O. Jost, S. R. P. Silva, W. Pompe, and B. Büchner, "Novel catalysts, room temperature, and the importance of oxygen for the synthesis of single-walled carbon nanotubes," *Nano Lett.*, vol. 5, pp. 1209–1215, 2005.

[46] T. W. Ebbesen and P. M. Ajayan, "Large-scale synthesis of carbon nanotubes," *Nature*, vol. 358, pp. 220–222, 1992.

[47] C. Journet, W. K. Maser, P. Bernier, A. Loiseau, M. Lamy de la Chapelle, S. Lefrant, P. Deniard, R. Lee, and J. E. Fischer, "Large-scale production of single-walled carbon nanotubes by the electric-arc technique," *Nature*, vol. 388, pp. 756–758, 1997.

[48] A. Thess, R. Lee, P. Nikolaev, H. Dai, P. Petit, J. Robert, X. Chunhui, Y. H. Lee, S. G. Kim, A. G. Rinzler, D. T. Colbert, G. E. Scuseria, D. Tománek, J. E. Fischer, and R. E. Smalley, "Crystalline ropes of metallic carbon nanotubes," *Science*, vol. 273, pp. 483–487, 1996.

[49] W. K. Maser, E. Muños, A. M. Benito, M. T. Martínez, G. F. de la Fuente, Y. Maniette, E. Anglaret, and J.-L. Sauvajol, "Production of high-density single-walled nanotube material by a simple laser-ablation method," vol. 292, pp. 587–593, 1998.

[50] M. Yudasaka, R. Yamada, N. Sensui, T. Wilkins, T. Ichihashi, and S. Iijima, "Mechanism of the effect of NiCo, Ni and Co catalysts on the yield of single-wall carbon nanotubes formed by pulsed Nd:YAG laser ablation," *J. Phys. Chem. B*, vol. 103, pp. 6224–6229, 1999.

[51] E. Borowiak-Palen, T. Pichler, X. Liu, M. Knupfer, A. Graff, O. Jost, W. Pompe, R. J. Kalenczuk, and J. Fink, "Reduced diameter distribution of single-wall carbon nanotubes by selective oxidation," vol. 363, pp. 567–572, 2002.

[52] M. H. Rümmeli, C. Kramberger, M. Löffler, O. Jost, M. Bystrzejewski, A. Grüneis, T. Gemming, W. Pompe, B. Büchner, and T. Pichler, "Catalyst volume to surface area constraints for nucleating carbon nanotubes," *J. Phys. Chem. B*, vol. 111, pp. 8234–8241, 2007.

[53] H. Murakami, M. Hirakawa, C. Tanaka, and H. Yamakawa, "Field emission from well-aligned, patterned, carbon nanotube emitters," *Appl. Phys. Lett.*, vol. 76, pp. 1776–1778, 2000.

[54] M. H. Rümmeli, C. Kramberger, M. Löffler, M. Kalbác, H.-W. Hübers, A. Grüneis, A. Barreiro, D. Grimm, P. Ayala, T. Gemming, F. Schäffel, L. Dunsch, B. Büchner, and T. Pichler, "Synthesis of single wall carbon nanotubes with invariant diameters using a modified laser assisted chemical vapour deposition route," *Nanotechnology*, vol. 17, pp. 5469–5473, 2006.

[55] H. L. Cheng, F. Li, G. Su, H. Y. Pan, L. L. He, X. Sun, and M. S. Dresselhaus, "Large-scale and low-cost synthesis of single-walled carbon nanotubes by the catalytic pyrolysis of hydrocarbons," *Appl. Phys. Lett.*, vol. 72, pp. 3282–3284, 1998.

[56] S. Huang, X. Cai, and J. Liu, "Growth of millimeter-long and horizontally aligned single-walled carbon nanotubes on flat substrates," *J. Am. Chem. Soc.*, vol. 125, pp. 5635–5637, 2003.

[57] M. Hofmann, D. Nezich, A. Reina, and J. Kong, "In-situ sample rotation as a tool to understand chemical vapor deposition growth of long carbon nanotubes," *Nano Lett.*, vol. 8, pp. 4122–4127, 2008.

[58] L. Delzeit, C. V. Nguyen, B. Chen, R. Stevens, A. Cassell, J. Han, and M. Meyyappan, "Multiwalled carbon nanotubes by chemical vapor deposition using multilayered metal catalysts," *J. Phys. Chem. B*, vol. 106, pp. 5629–5635, 2002.

[59] C. Täschner, F. Pácal, A. Leonhardt, P. Spatenka, K. Bartsch, A. Graff, and R. Kaltofen, "Synthesis of aligned carbon nanotubes by DC plasma-enhanced hot filament CVD," *Surf. Coat. Tech.*, vol. 174-175, pp. 81–87, 2003.

[60] T. Yamada, T. Namai, K. Hata, D. N. Futaba, K. Mizuno, J. Fan, M. Yudasaka, M. Yumura, and S. Iijima, "Size-selective growth of double-walled carbon nanotube forests from engineered iron catalysts," *Nature Nanotech.*, vol. 1, pp. 131–136, 2006.

[61] S. Fan, M. G. Chapline, N. R. Franklin, T. W. Tombler, A. M. Cassell, and H. Dai, “Self-oriented regular arrays of carbon nanotubes and their field emission properties,” *Science*, vol. 283, pp. 512–514, 1999.

[62] S. Huang, B. Maynor, X. Cai, and J. Liu, “Ultralong, well-aligned single-walled carbon nanotube architectures on surfaces,” *Adv. Mater.*, vol. 15, pp. 1651–1655, 2003.

[63] C. L. Cheung, A. Kurtz, H. Park, and C. M. Lieber, “Diameter-controlled synthesis of carbon nanotubes,” *J. Phys. Chem. B*, vol. 106, pp. 2429–2433, 2002.

[64] Y. Huh, M. L. H. Green, Y. H. Kim, J. Y. Lee, and C. J. Lee, “Control of carbon nanotube growth using cobalt nanoparticles as catalyst,” *Appl. Surf. Sci.*, vol. 249, pp. 145–150, 2005.

[65] H. Ago, T. Komatsu, S. Ohshima, Y. Kuriki, and M. Yumura, “Dispersion of metal nanoparticles for aligned carbon nanotube arrays,” *Appl. Phys. Lett.*, vol. 77, pp. 79–81, 2000.

[66] R. D. Bennett, A. J. Hart, and R. E. Cohen, “Controlling the morphology of carbon nanotube films by varying the areal density of catalyst nanoclusters using block-copolymer micellar thin films,” *Adv. Mater.*, vol. 18, pp. 2274–2279, 2006.

[67] X. Liu, T. P. Bigioni, Y. Xu, A. M. Cassell, and B. A. Cruden, “Vertically aligned dense carbon nanotube growth with diameter control by block copolymer micelle catalyst templates,” *J. Phys. Chem. B*, vol. 110, pp. 20102–20106, 2006.

[68] L. An, J. M. Owens, L. E. McNeil, and J. Liu, “Synthesis of nearly uniform single-walled carbon nanotubes using identical metal-containing molecular nanoclusters as catalysts,” *J. Am. Chem. Soc.*, vol. 124, pp. 13688–13689, 2002.

[69] W. Kim, H. C. Choi, M. Shim, Y. Li, D. Wang, and H. Dai, “Synthesis of ultralong and high percentage of semiconducting single-walled carbon nanotubes,” *Nano Lett.*, vol. 2, pp. 703–708, 2002.

[70] D. Kondo, S. Sato, A. Kawabata, and Y. Awano, “Diameter-controlled growth of multi-walled carbon nanotubes by hot-filament chemical vapor deposition with ferritin as a catalyst on a silicon substrate,” *Jpn. J. Appl. Phys.*, vol. 44, pp. 5292–5295, 2005.

[71] S. Sato, A. Kawabata, M. Nihei, and Y. Awano, “Growth of diameter-controlled carbon nanotubes using monodisperse nickel nanoparticles obtained with a differential mobility analyzer,” vol. 382, pp. 361–366, 2003.

[72] F. Schäffel, C. Kramberger, M. H. Rümmeli, R. Kaltofen, D. Grimm, A. Grüneis, E. Mohn, T. Gemming, T. Pichler, B. Büchner, B. Rellinghaus, and L. Schultz, “Carbon nanotubes grown from individual gas phase prepared iron catalyst particles,” *Phys. Stat. Sol.(a)*, vol. 204, pp. 1786–1790, 2007.

[73] F. Schäffel, C. Kramberger, M. H. Rümmeli, D. Grimm, E. Mohn, T. Gemming, T. Pichler, B. Rellinghaus, B. Büchner, and L. Schultz, “Nanoengineered catalyst particles as a key for tailor-made carbon nanotubes,” *Chem. Mater.*, vol. 19, pp. 5006–5009, 2007.

[74] F. Schäffel, M. H. Rümmeli, C. Kramberger, U. Queitsch, E. Mohn, R. Kaltofen, T. Pichler, B. Büchner, B. Rellinghaus, and L. Schultz, “Tailoring the diameter, density and number of walls of carbon nanotubes through predefined catalyst particles,” *Phys. Stat. Sol.(a)*, vol. 205, pp. 1382–1385, 2008.

[75] R. Krupke, F. Hennrich, H. von Lohneysen, and M. M. Kappes, “Separation of metallic from semiconducting single-walled carbon nanotubes,” *Science*, vol. 301, pp. 344–347, 2003.

[76] M. S. Arnold, A. A. Green, J. F. Hulvat, S. I. Stupp, and M. C. Hersam, “Sorting carbon nanotubes by electronic structure using density differentiation,” *Nature Nanotech.*, vol. 1, pp. 60–65, 2006.

[77] D. Nishide, Y. Miyata, K. Yanagi, T. Tanaka, and H. Kataura, “Effective separation of carbon nanotubes and metal particles from pristine raw soot by ultracentrifugation,” *Jpn. J. Appl. Phys.*, vol. 48, 015004, 2009.

[78] W.-Q. Han, J. Cumings, X. Huang, K. Bradley, and A. Zettl, “Synthesis of aligned $B_xC_yN_z$ nanotubes by a substitution-reaction route,” vol. 346, pp. 368–372, 2001.

[79] R. T. K. Baker, M. A. Barber, P. S. Harris, F. S. Feates, and R. J. Waite, “Nucleation and growth of carbon deposits from the nickel catalyzed decomposition of acetylene,” *J. Catal.*, vol. 26, pp. 51–62, 1972.

[80] S.-Y. Bae, K.-H. Shin, J.-Y. Jeong, and J.-G. Kim, "Feasibility of FePt longitudinal recording media for ultrahigh density recording," *J. Appl. Phys.*, vol. 87, no. 9, pp. 6953–6955, 2000.

[81] H. C. Schniepp, J.-L. Li, M. J. McAllister, H. Saki, M. Herrera-Alonso, D. H. Adamson, R. K. Prudhomme, R. Car, D. A. Saville, and I. A. Aksay, "Functionalized single graphene sheets derived from splitting graphite oxide," *J. Phys. Chem. B*, vol. 110, pp. 8535–8539, 2006.

[82] M. Cantoro, S. Hofmann, S. Pisana, V. Scardaci, A. Parvez, C. Ducati, A. C. Ferrari, A. M. Blackburn, K.-Y. Wang, and J. Robertson, "Catalytic chemical vapor deposition of single-wall carbon nanotubes at low temperatures," *Nano Lett.*, vol. 6, pp. 1107–1112, 2006.

[83] O. A. Louchev, T. Laude, Y. Sato, and H. Kanda, "Diffusion-controlled kinetics of carbon nanotube forest growth by chemical vapor deposition," *J. Chem. Phys.*, vol. 118, pp. 7622–7634, 2003.

[84] S. Hofmann, G. Csányi, A. C. Ferrari, M. C. Payne, and J. Robertson, "Surface diffusion: The low activation energy path for nanotube growth," *Phys. Rev. Lett.*, vol. 95, 036101, 2005.

[85] S. Hofmann, R. Sharma, C. Ducati, G. Du, C. Mattevi, C. Cepek, M. Cantoro, S. Pisana, A. Parvez, F. Cervantes-Sodi, A. C. Ferrari, R. Dunin-Borkowski, S. Lizzit, L. Petaccia, A. Goldoni, and J. Robertson, "In situ observations of catalyst dynamics during surface-bound carbon nanotube nucleation," *Nano Lett.*, vol. 7, pp. 602–608, 2007.

[86] S. Helveg, C. López-Cartes, J. Sehested, P. L. Hansen, B. S. Clausen, J. R. Rostrup-Nielsen, F. Abild-Pedersen, and J. K. Nørskov, "Atomic-scale imaging of carbon nanofibre growth," *Nature*, vol. 427, pp. 426–428, 2004.

[87] M. Kusunoki, T. Suzuki, K. Kaneko, and M. Ito, "Formation of self-aligned carbon nanotube films by surface decomposition of silicon carbide," *Phil. Mag. Lett.*, vol. 79, pp. 153–161, 1999.

[88] M. Kusunoki, T. Suzuki, T. Hirayama, N. Shibata, and K. Kaneko, "A formation mechanism of carbon nanotube films on SiC (0001)," *Appl. Phys. Lett.*, vol. 77, pp. 531–533, 2000.

[89] W. Lu, J. Boeckl, W. C. Mitchel, J. Rigueur, and W. E. Collins, “Role of oxygen in growth of carbon nanotubes on SiC,” *Mater. Sci. Forum*, vol. 527-529, pp. 1575–1578, 2006.

[90] D. Takagi, H. Hibino, S. Suzuki, Y. Kobayashi, and Y. Homma, “Carbon nanotube growth from semiconductor nanoparticles,” *Nano Lett.*, vol. 7, pp. 2272–2275, 2007.

[91] K. Miyake, M. Kusunoki, H. Usami, N. Umehara, and S. Sasaki, “Tribological properties of densely packed vertically aligned carbon nanotube film on SiC formed by surface decomposition,” *Nano Lett.*, vol. 7, pp. 3285–3289, 2007.

[92] M. H. Rümmeli, A. Grüneis, M. Löffler, O. Jost, R. Schönfelder, C. Kramberger, D. Grimm, T. Gemming, A. Barreiro, E. Borowiak-Palen, M. Kalbác, P. Ayala, H.-W. Hübers, B. Büchner, and T. Pichler, “Novel catalysts for low temperature synthesis of single wall carbon nanotubes,” *Phys. Stat. Sol.(b)*, vol. 243, pp. 3101–3105, 2006.

[93] W. Zhou, Z. Han, J. Wang, Y. Zhang, Z. Jin, X. Sun, Y. Zhang, C. Yan, and Y. Li, “Copper catalyzing growth of single-walled carbon nanotubes on substrates,” *Nano Lett.*, vol. 6, pp. 2987–2990, 2006.

[94] D. Takagi, Y. Homma, H. Hibino, S. Suzuki, and Y. Kobayashi, “Single-walled carbon nanotube growth from highly activated metal nanoparticles,” *Nano Lett.*, vol. 6, pp. 2642–2645, 2006.

[95] D. Takagi, Y. Kobayashi, H. Hibino, S. Suzuki, and Y. Homma, “Mechanism of gold-catalyzed carbon material growth,” *Nano Lett.*, vol. 8, pp. 832–835, 2008.

[96] E. J. Bae, W. B. Choi, K. S. Jeong, J. U. Chu, G.-S. Park, S. Song, and K. Yoo, “Selective growth of carbon nanotubes on pre-patterned porous anodic aluminum oxide,” *Adv. Mater.*, vol. 14, pp. 277–279, 2002.

[97] J. J. Schneider, N. I. Maksimova, J. Engstler, R. Joshi, R. Schierholz, and R. Feile, “Catalyst free growth of a carbon nanotube-alumina composite structure,” *Inorg. Chim. Acta*, vol. 361, pp. 1770–1778, 2006.

[98] M. H. Rümmeli, C. Kramberger, A. Grüneis, P. Ayala, T. Gemming, B. Büchner, and T. Pichler, “On the graphitization nature of oxides for the formation of carbon nanostructures,” *Chem. Mater.*, vol. 19, pp. 4105–4107, 2007.

[99] M. H. Rümmeli, F. Schäffel, C. Kramberger, T. Gemming, A. Bachmatiuk, R. J. Kalenczuk, B. Rellinghaus, B. Büchner, and T. Pichler, “Oxide-driven carbon nanotube growth in supported catalyst CVD,” *J. Am. Chem. Soc.*, vol. 129, pp. 15772–15773, 2007.

[100] S. Konishi, W. Sugimoto, Y. Murakami, and Y. Takasu, “Catalytic creation of channels in the surface layers of highly oriented pyrolytic graphite by cobalt nanoparticles,” *Carbon*, vol. 44, pp. 2338–2340, 2004.

[101] P. S. Harris, F. S. Feates, and B. G. Reuben, “Controlled atmosphere electron microscopy studies of graphite gasification - 4. Catalysis of the graphite-O_2 reaction by silver,” *Carbon*, vol. 12, pp. 189–197, 1974.

[102] R. T. Yang and C. Wong, “Catalysis of carbon oxidation by transition metal carbides and oxides,” *J. Catal.*, vol. 85, pp. 154–168, 1984.

[103] P. J. Goethel and R. T. Yang, “Mechanism of catalyzed graphite oxidation by monolayer channeling and monolayer edge recession,” *J. Catal.*, vol. 119, pp. 201–214, 1989.

[104] Z. J. Pan and R. T. Yang, “Catalytic behavior of transition metal oxide in graphite gasification by oxygen, water and carbon dioxide,” *J. Catal.*, vol. 130, pp. 161–172, 1991.

[105] S. G. Chen and R. T. Yang, “Mechanism of alkali and alkaline earth catalyzed gasification of graphite by CO_2 and H_2O studied by electron microscopy,” *J. Catal.*, vol. 138, pp. 12–23, 1992.

[106] H. Y. Huang and R. T. Yang, “Catalyzed carbon-NO reaction studied by scanning tunneling microscopy and *ab initio* molecular orbital calculations,” *J. Catal.*, vol. 185, pp. 286–296, 1999.

[107] A. Tomita and Y. Tamai, “Hydrogenation of carbons catalyzed by transition metals,” *J. Catal.*, vol. 27, pp. 293–300, 1972.

[108] R. T. Rewick, P. R. Wentrcek, and H. Wise, “Carbon gasification in the presence of metal catalysts,” *Fuel*, vol. 53, pp. 274–279, 1974.

[109] P. J. Goethel and R. T. Yang, “Platinum-catalyzed hydrogenation of graphite: Mechanism studied by the rates of monolayer channeling,” *J. Catal.*, vol. 101, pp. 342–351, 1986.

[110] P. J. Goethel and R. T. Yang, “Mechanism of graphite hydrogenation catalyzed by nickel,” *J. Catal.*, vol. 108, pp. 356–363, 1987.

[111] P. J. Goethel and R. T. Yang, “Mechanism of graphite hydrogenation catalyzed by ruthenium particles,” *J. Catal.*, vol. 111, pp. 220–226, 1988.

[112] S. Sun, C. B. Murray, D. Weller, L. Folks, and A. Moser, “Monodisperse FePt nanoparticles and ferromagnetic FePt nanocrystal superlattices,” *Science*, vol. 287, pp. 1989–1992, 2000.

[113] S. Stappert, B. Rellinghaus, M. Acet, and E. F. Wassermann, “Gas-phase preparation of $L1_0$ ordered FePt nanoparticles,” *J. Crystal Growth*, vol. 252, pp. 440–450, 2003.

[114] S. Huang, M. Woodson, R. E. Smalley, and J. Liu, “Growth mechanism of oriented long single walled carbon nanotubes using “fast-heating” chemical vapor deposition process,” *Nano Lett.*, vol. 4, pp. 1025–1028, 2004.

[115] H. Gu, P.-L. Ho, K. W. T. Tsang, L. Wang, and B. Xu, “Using biofunctional magnetic nanoparticles to capture vancomycin-resistant enterococci and other gram-positive bacteria at ultralow concentration,” *J. Am. Chem. Soc.*, vol. 125, pp. 15702–15703, 2003.

[116] T. B. Massalski, J. L. Murray, L. H. Bennet, and H. Baker, *Binary phase diagrams*. ASM International, Materials Park, Ohio, 1986.

[117] M. H. Hong, K. Hono, and M. Watanabe, “Microstructure of FePt/Pt magnetic thin films with high perpendicular coercivity,” *J. Appl. Phys.*, vol. 84, pp. 4403–4409, 1998.

[118] M. R. Visokey and R. Sinclair, “Direct formation of ordered CoPt and FePt compound thin films by sputtering,” *Appl. Phys. Lett.*, vol. 66, pp. 1692–1694, 1995.

[119] J.-U. Thiele, L. Folks, M. F. Toney, and D. K. Weller, “Perpendicular magnetic anisotropy and magnetic domain structure in sputtered epitaxial FePt (001) $L1_0$ films,” *J. Appl. Phys.*, vol. 84, no. 10, pp. 5686–5692, 1998.

[120] A. Cebollada, R. F. C. Farrow, and M. F. Toney, *Magnetic Nanostructures,* pp. 93-122. American Scientific Publisher, California, 2002.

[121] D. J. Sellmyer, M. Yu, and R. D. Kirby, "Nanostructured magnetic films for extremely high density recording," *Nanostruct. Mater.*, vol. 12, pp. 1021–1026, 1999.

[122] Y. K. Takahashi, T. Ohkubo, M. Ohnuma, and K. Hono, "Size effect on the ordering of FePt granular films," *J. Appl. Phys.*, vol. 93, no. 10, pp. 7166–7168, 2003.

[123] B. Yang, M. Asta, O. N. Mryasov, T. J. Klemmer, and R. W. Chantrell, "Equilibrium Monte Carlo simulations of $A1-L1_0$ ordering in FePt nanoparticles," *Scripta Mater.*, vol. 53, pp. 417–422, 2005.

[124] R. Kozubski, M. Kozlowski, V. Pierron-Bohnes, and W. Pfeiler, "Order-order relaxations in intermetallics," *Z. Metallkd.*, vol. 95, no. 10, pp. 880–887, 2004.

[125] P. Haasen, *Physikalische Metallkunde.* Springer Verlag, Berlin, Heidelberg, New York, pp. 133-152, 1994.

[126] Z. R. Dai, S. Sun, and Z. L. Wang, "Phase transformation, coalescence, and twinning of monodisperse FePt nanocrystals," *Nano Lett.*, vol. 1, pp. 443–447, 2001.

[127] J.-M. Qiu and J.-P. Wang, "Monodispersed and highly ordered $L1_0$ FePt nanoparticles prepared in the gas phase," *Appl. Phys. Lett.*, vol. 88, 192505, 2006.

[128] C.-B. Rong, D. Li, V. Nandwana, N. Poudyal, Y. Ding, Z. L. Wang, H. Zeng, and J. P. Liu, "Size-dependent chemical and magnetic ordering in $L1_0$-FePt nanoparticles," *Adv. Mater.*, vol. 18, pp. 2984–2988, 2006.

[129] H. Haberland, M. Mall, M. Moseler, Y. Qiang, T. Reiners, and Y. Thurner, "Filling of micron-sized contact holes with copper by energetic cluster-impact," *J. Vac. Sci. Technol. A*, vol. 12, pp. 2925–2930, 1994.

[130] R. C. Flagan and M. M. Lunden, "Particle structure control in nanoparticle synthesis from the vapor phase," *Mat. Sci. Eng. A*, vol. 204, pp. 112–124, 1995.

[131] F. Schäffel, *Morphologische und kristallographische Charakterisierung von FePt-Nanopartikeln aus einer Gas-Aggregationsquelle.* Diploma thesis, TU Dresden, 2006.

[132] F. Schäffel, C. Schünemann, M. H. Rümmeli, C. Täschner, D. Pohl, C. Kramberger, T. Gemming, A. Leonhardt, T. Pichler, B. Rellinghaus, B. Büchner, and L. Schultz, "Comparative study on thermal and plasma enhanced CVD grown carbon nanotubes from gas phase prepared elemental and binary catalyst particles," *Phys. Stat. Sol.(b)*, vol. 245, pp. 1919–1922, 2008.

[133] A. Grüneis, C. Kramberger, D. Grimm, T. Gemming, M. H. Rümmeli, A. Barreiro, P. Ayala, T. Pichler, C. Schaman, H. Kuzmany, J. Schumann, and B. Büchner, "Eutectic limit for the growth of carbon nanotubes from a thin iron film by chemical vapor deposition of cyclohexane," vol. 425, pp. 301–305, 2006.

[134] H. Kuzmany, *An introduction to solid-state spectroscopy.* Springer, Berlin, Heidelberg, New York, 1998.

[135] F. Tuinstra and J. L. Koenig, "Raman spectrum of graphite," *J. Chem. Phys.*, vol. 53, pp. 1126–1130, 1970.

[136] L. G. Cancado, M. A. Pimenta, B. R. A. Neves, M. S. S. Dantas, and A. Jorio, "Influence of the atomic structure on the raman spectra of graphite edges," *Phys. Rev. Lett.*, vol. 93, 247401, 2004.

[137] C. G. Granqvist and R. A. Buhrman, "Ultrafine metal particles," *J. Appl. Phys.*, vol. 47, no. 5, pp. 2200–2219, 1976.

[138] Y. Li, W. Kim, Y. Zhang, M. Rolandi, D. Wang, and H. Dai, "Growth of single-walled carbon nanotubes from discrete catalytic nanoparticles of various sizes," *J. Phys. Chem. B*, vol. 105, pp. 11424–11431, 2001.

[139] S. B. Sinnott, R. Andrews, D. Qian, A. M. Rao, Z. Mao, E. C. Dickey, and F. Derbyshire, "Model of carbon nanotube growth through chemical vapor deposition," vol. 315, pp. 25–30, 1999.

[140] S. Tsyganov, J. Kästner, B. Rellinghaus, T. Kauffeldt, F. Westerhoff, and D. Wolf, "Analysis of Ni nanoparticle gas phase sintering," *Phys. Rev. B*, vol. 75, 045421, 2007.

[141] M. H. Rümmeli, F. Schäffel, M. Löffler, C. Kramberger, D. Adebimpe, T. Gemming, P. Ayala, B. Rellinghaus, L. Schultz, B. Büchner, and T. Pichler, "Unifying catalyst size dependencies in floating catalyst and supported catalyst carbon nanotube synthesis," *Phys. Stat. Sol.(a)*, vol. 205, pp. 1386–1390, 2008.

[142] Y. Shibuta and S. Maruyama, “Molecular dynamics simulation of formation process of single-walled carbon nanotubes by CCVD method,” vol. 382, pp. 381–386, 2003.

[143] F. Ding, A. Rosén, and K. Bolton, “Molecular dynamics study of the catalyst particle size dependence on carbon nanotube growth,” *J. Chem. Phys.*, vol. 121, pp. 2775–2779, 2004.

[144] J.-Y. Raty, F. Gygi, and G. Galli, “Growth of carbon nanotubes on metal nanoparticles: A microscopic mechanism from *ab initio* molecular dynamics simulations,” *Phys. Rev. Lett.*, vol. 95, 096103, 2005.

[145] H. Yoshida, S. Takeda, T. Uchiyama, H. Kohno, and Y. Homma, “Atomic-scale in-situ observation of carbon nanotube growth from solid state iron carbide nanoparticles,” *Nano Lett.*, vol. 8, pp. 2082–2086, 2008.

[146] G. E. Brown, V. E. Henrich, W. H. Casey, D. L. Clark, C. Eggleston, A. Felmy, D. W. Goodman, M. Grätzel, G. Maciel, M. I. McCarthy, K. H. Nealson, D. A. Sverjensky, M. F. Toney, and J. M. Zachara, “Metal oxide surfaces and their interactions with aqueous solutions and microbial organisms,” *Chem. Rev.*, vol. 99, pp. 77–174, 1999.

[147] G. Zhang, D. Mann, L. Zhang, A. Javey, Y. Li, E. Yenilmez, Q. Wang, J. P. McVittie, Y. Nishi, J. Gibbons, and H. Dai, “Ultra-high-yield growth of vertical single-walled carbon nanotubes: Hidden roles of hydrogen and oxygen,” *Proc. Nat. Acad. Sci.*, vol. 102, pp. 16141–16145, 2005.

[148] M. Shen and F. Zaera, “Thermal chemistry of water adsorbed on clean and oxygen-predosed V(100) single-crystal surfaces,” *J. Phys. Chem. C*, vol. 11, pp. 13570–13578, 2007.

[149] A. Oya and H. Marsh, “Phenomena of catalytic graphitization,” *J. Mater. Sci.*, vol. 17, pp. 309–322, 1982.

[150] R. T. K. Baker, P. S. Harris, and R. B. Thomas, “Direct observation of particle mobility on a surface in gaseous environment,” *Surf. Sci.*, vol. 46, pp. 311–316, 1974.

[151] R. T. K. Baker, "In situ electron microscopy studies of catalyst particle behaviour," *Catal. Rev.-Sci. Eng.*, vol. 19, pp. 161–209, 1979.

[152] N. Severin, S. Kirstein, I. M. Sokolov, and J. P. Rabe, "Rapid trench channeling of graphenes with catalytic silver nanoparticles," *Nano Lett.*, vol. 9, pp. 457–461, 2009.

[153] M. Löffler, *Nanomanipulation and in-situ transport measurements on carbon nanotubes.* Dissertation, TU Dresden, 2009.

[154] F. Schäffel, C. Täschner, M. H. Rümmeli, V. Neu, U. Wolff, U. Queitsch, D. Pohl, R. Kaltofen, A. Leonhardt, B. Rellinghaus, B. Büchner, and L. Schultz, "Carbon nanotubes terminated with hard magnetic FePt nanomagnets," *Appl. Phys. Lett.*, vol. 94, 193107, 2009.

[155] G. Wulff, "Zur Frage der Geschwindigkeit des Wachstums unter Auflösung der Kristallflächen," *Z. Kristallogr.*, vol. 34, pp. 449–530, 1901.

[156] J. H. Warner, F. Schäffel, G. Zhong, M. H. Rümmeli, B. Büchner, J. Robertson, and G. A. D. Briggs, "Investigating the diameter dependent stability of single walled carbon nanotubes," *ACS Nano*, vol. 3, pp. 1557–1563, 2009.

[157] T. Konno and R. Sinclair, "Crystallization of co-sputtered amorphous cobalt-carbon alloys - morphology and kinetics of spherulitic growth," *Mat. Sci. Eng. A*, vol. 179, pp. 297–302, 1994.

[158] T. Tanaka, K. N. Ishihara, and R. H. shingu, "Formation of metastable phases of Ni-C and Co-C systems by mechanical alloying," *Met. Trans.*, vol. 23, pp. 2431–2435, 1992.

[159] X. B. Liu, J. Wang, and Z. Z. Fang, "Hexagonal cobalt carbide formed by carbon ion-implantation," *J. Appl. Phys.*, vol. 69, pp. 7342–7344, 1991.

[160] Y.-W. Son, M. L. Cohen, and S. G. Louie, "Half-metallic graphene nanoribbons," *Nature*, vol. 444, pp. 347–349, 2006.

[161] L. Brey and H. A. Fertig, "Electronic states of graphene nanoribbons studied with the Dirac equation," *Phys. Rev. B*, vol. 73, 235411, 2006.

[162] I.-C. Chen, L.-H. Chen, A. Gapin, S. Jin, L. Yuan, and S.-H. Liou, "Iron-platinum-coated carbon nanocone probes on tipless cantilevers for high resolution magnetic force imaging," *Nanotechnology*, vol. 19, 075501, 2008.

[163] T. Tsoufis, A. Tomou, D. Gournis, A. P. Douvalis, I. Panagiotopoulos, B. Kooi, V. Georgakilas, I. Arfaoui, and T. Bakas, "Novel nanohybrids derived from the attachment of FePt nanoparticles on carbon nanotubes," *J. Nanosci. Nanotech.*, vol. 8, pp. 5942–5951, 2008.

[164] C. T. Kuo, C. H. Lin, and A. Y. Lo, "Feasibility studies of magnetic particle-embedded carbon nanotubes for perpendicular recording media," *Diam. Relat. Mater.*, vol. 12, pp. 799–805, 2003.

[165] X. Wang, Y. Wenbo, M. He, M. Liu, J. Zhang, and Z. Liu, "Bimetallic catalysts for the efficient growth of SWNTs on surfaces," *Chem. Mater.*, vol. 16, pp. 799–805, 2004.

[166] C. Schünemann, *Synthese von Kohlenstoffnanoröhren unter Verwendung von FePt-Katalysatoren.* Diploma thesis, TU Dresden, 2008.

[167] A. R. Harutyunyan, T. Tokune, and E. Mora, "Liquid as a required catalyst phase for carbon single-walled nanotube growth," *Appl. Phys. Lett.*, vol. 87, 051919, 2005.

[168] X. Liu, W. Li, H. Xu, and Y. Chen, "A comparative study of non-oxidative pyrolysis and oxidative cracking of cyclohexane to light alkenes," *Fuel Proc. Tech.*, vol. 86, pp. 151–167, 2004.

[169] K. Bartsch, K. Biedermann, T. Gemming, and A. Leonhardt, "On the diffusion-controlled growth of multiwalled carbon nanotubes," *J. Appl. Phys.*, vol. 97, 114301, 2005.

[170] F. Kurth, *Struktur und hartmagnetische Eigenschaften ultradünner FePt-Schichten.* Diploma thesis, TU Dresden, 2006.

[171] T. de los Arcos, F. Vonau, M. G. Garnier, V. Thommen, H.-G. Boyen, P. Oelhafen, M. Düggelin, D. Mathis, and R. Guggenheim, "Influence of iron-silicon interaction on the growth of carbon nanotubes produced by chemical vapor deposition," *Appl. Phys. Lett.*, vol. 13, pp. 2383–2385, 2002.

[172] Y. Homma, Y. Kobayashi, T. Ogino, D. Takagi, R. Ito, Y. J. Jung, and P. M. Ajayan, “Role of transition metal catalysts in single-walled carbon nanotube growth in chemical vapour deposition,” *J. Phys. Chem. B*, vol. 107, pp. 12161–12164, 2003.

[173] A. Bachmatiuk and M. H. Rümmeli *to be published,* 2009.

Curriculum vitae

Date of birth 29th August 1980 in Dresden

Citizenship German

Experience May 2006 - present

PhD-studies at the Leibniz Institute for Solid State and Materials Research, Dresden, Germany

- CVD synthesis of CNT from predefined nanoparticles
- Synthesis of hard-magnetically terminated CNT
- Aberration corrected HRTEM

October 2000 - March 2006

Material Science studies at the Dresden University of Technology, Dresden, Germany

- Specialization in Functional Materials
- Diploma thesis: "Morphological and crystallographic characterization of FePt nanoparticles from a gas aggregation source"
- Diploma with distinction

October 2003 - March 2004

Internship at the Research Centre for Advanced Mineral and Materials Processing in Perth, Australia

- Mechanochemical processing of iron oxide nanoparticles

September 1999 - August 2000
Gap Student at St. James School, Great Malvern, UK
- German foreign language assistant
- Tutoring in maths and music

Education

August 1992 - June 1999
St. Benno Gymnasium, Dresden, Germany
- Abitur

Awards

PhD stipend from Cusanuswerk

Poster awards:
- Deutsche Physikerinnentagung - Berlin, Germany (2006)
  Best poster at the German conference of female physicists
- Trends in Nanotechnology, TNT08 - Oviedo, Spain (2008)
  Poster prize from the GDR-I (France) on the Science and Application of Nanotubes

Languages

German (mother tongue)
English (excellent, C2 in the European Standard of Languages)
French (good, B1 in the European Standard of Languages)
Latin (Latinum)

Interests

Music
- Saxophone (member of the IFW-Band "Nanonics")
- Choir, piano, guitar

Sport
- Rock climbing, hiking

Publication list

[1] F. Schäffel, C. Täschner, M. H. Rümmeli, V. Neu, U. Wolff, U. Queitsch, D. Pohl, R. Kaltofen, A. Leonhardt, B. Rellinghaus, B. Büchner, L. Schultz, *Carbon nanotubes terminated with hard magnetic FePt nanomagnets*, Appl. Phys. Lett. **94**, 193107/1-3 (2009).

[2] F. Schäffel, J. H. Warner, A. Bachmatiuk, B. Rellinghaus, L. Schultz, M. H. Rümmeli, *Shedding light on the crystallographic etching of multi-layer graphene at the atomic scale*, Nano Res. **2**, 695-705 (2009).

[3] J. H. Warner, F. Schäffel, G. Zhong, M. H. Rümmeli, B. Büchner, J. Robertson G. A. D. Briggs, *Investigating the diameter dependent stability of single walled carbon nanotubes*, ACS Nano **3**, 1557-1563 (2009).

[4] J. H. Warner, F. Schäffel, M. H. Rümmeli, B. Büchner, *Examining the edge structure of multi-layer graphene sheets*, Chem. Mater. **21**, 2418-2421 (2009).

[5] S. B. Menzel, J. Thomas, U. Weißker, F. Schäffel, C. Hoßbach, M. Albert, S. Hampel, T. Gemming, *Preparation of CNT-copper matrix composite films*, J. Nanosci. Nanotechnol. **9**, 6096-6103 (2009).

[6] U. Queitsch, C. Hamann, F. Schäffel, B. Rellinghaus, L. Schultz, A. Blüher, M. Mertig, *Towards dense bio-templated magnetic nanoparticle arrays: Probing the particle-template interaction*, J. Phys. Chem. C **113**, 10471-10476 (2009).

[7] A. Bachmatiuk, F. Börrnert, M. Grobosch, F. Schäffel, U. Wolff, A. Scott, M. Zaka, J. H. Warner, R. Klingeler, M. Knupfer, B. Büchner, M. H. Rümmeli, *Investigating the graphitization mechanism of SiO_2 nanoparticles in CVD*, ACS Nano (2009), DOI 10.1021/nn9009278.

[8] F. Schäffel, J. H. Warner, A. Bachmatiuk, B. Rellinghaus, B. Büchner, L. Schultz, M. H. Rümmeli, *On the catalytic hydrogenation of graphite for graphene nanoribbon fabrication*, Phys. Stat. Sol. b **246**, 2540-2544 (2009).

[9] M. H. Rümmeli, F. Schäffel, A. Bachmatiuk, G. Trotter, D. Adebimpe, G. Simha-Martynková, D. Plancha, B. Rellinghaus, P. G. McCormick, E. Borowiak-Palen, P. Ayala, T. Pichler, R. Klingeler, M. Knupfer, B. Büchner, *Oxide catalysts for carbon nanotubes and few layer graphene formation*, Phys. Stat. Sol. b **246**, 2530-2533 (2009).

[10] A. Bachmatiuk, M. Bystrzejewski, F. Schäffel, P. Ayala, U. Wolff, C. Mickel, T. Gemming, T. Pichler, E. Borowiak-Palen, R. Klingeler, H.-W. Hübers, M. Ulbrich, M. Knupfer, D. Haberer, B. Büchner, M. H. Rümmeli, *Carbon nanotube synthesis via ceramic catalysts*, Phys. Stat. Sol. b **246**, 2486-2489 (2009).

[11] S. M. Gorantla, F. Börrnert, A. Bachmatiuk, M. Dimitrakopoulou, F. Schäffel, R. Schönfelder, J. Thomas, T. Gemming, J. H. Warner, G. Cuniberti, J. Eckert, B. Büchner, M. H. Rümmeli, *Enhanced $\pi - \pi$ interactions between a C_{60} fullerene and a buckle bend on a double-walled carbon nanotubes*, accepted in Nano Res. (2009).

[12] A. Bachmatiuk, F. Schäffel, D. Planchà, G. Simha Martynkovà, N. Ioannides, T. Gemming, T. Pichler, R. J. Kalenczuk, E. Borowiak-Palen, M. H. Rümmeli, *Tuning carbon nanotubes through poor metal addition to iron catalysts in CVD*, accepted in Fullerenes Nanotubes and Carbon Nanostructures (2009).

[13] M. H. Rümmeli, F. Schäffel, T. de los Arcos, D. Haberer, A. Bachmatiuk, C. Kramberger, P. Ayala, E. Borowiak-Palen, D. Adebimpe, T. Gemming, A. Leonhardt, B. Rellinghaus, L. Schultz, T. Pichler, B. Büchner, *On the graphitisation role of oxide supports in carbon nanotube CVD synthesis* Phys. Stat. Sol. b **245**, 1939-1942 (2008).

[14] F. Schäffel, C. Schünemann, M. H. Rümmeli, C. Täschner, D. Pohl, C. Kramberger, T. Gemming, A. Leonhardt, T. Pichler, B. Rellinghaus, B. Büchner, L. Schultz, *Comparative study on thermal and plasma enhanced CVD grown carbon nanotubes from gas phase prepared elemental and binary catalyst particles* Phys. Stat. Sol. b **245**, 1919-1922 (2008).

[15] F. Schäffel, M. H. Rümmeli, C. Kramberger, U. Queitsch, E. Mohn, R. Kaltofen, T. Pichler, B. Büchner, *Tailoring the diameter, density and number of walls of carbon nanotubes through predefined catalyst particles*, Phys. Stat. Sol. a **205**, 1382-1385 (2008).

[16] M. H. Rümmeli, F. Schäffel, M. Löffler, C. Kramberger, D. Adebimpe, T. Gemming, P. Ayala, B. Rellinghaus, L. Schultz, B. Büchner, T. Pichler, *Unifying catalyst size dependencies in floating catalyst and supported catalyst carbon nanotube synthesis* Phys. Stat. Sol. a **205**, 1386-1390 (2008).

[17] F. Schäffel, C. Kramberger, M. H. Rümmeli, D. Grimm, E. Mohn, T. Gemming, T. Pichler, B. Rellinghaus, B. Büchner, L. Schultz, *Nanoengineered catalyst particles as a key for tailor-made carbon nanotubes*, Chem. Mater. **19**, 5006-5009 (2007).

[18] M. H. Rümmeli, F. Schäffel, C. Kramberger, T. Gemming, A. Bachmatiuk, R. J. Kalenczuk, B. Rellinghaus, B. Büchner, T. Pichler, *Oxide-driven carbon nanotube growth in supported catalyst CVD*, J. Am. Chem. Soc. **129**, 15772-15773 (2007).

[19] F. Schäffel, C. Kramberger, M. H. Rümmeli, R. Kaltofen, D. Grimm, A. Grüneis, E. Mohn, T. Gemming, T. Pichler, B. Büchner, B. Rellinghaus, L. Schultz, *Carbon nanotubes grown from individual gas phase prepared iron catalyst particles* Phys. Stat. Sol. a **204**, 1786-1790 (2007).

[20] M. H. Rümmeli, C. Kramberger, F. Schäffel, E. Borowiak-Palen, T. Gemming, B. Rellinghaus, O. Jost, M. Löffler, P. Ayala, T. Pichler, R. J. Kalenczuk, *Catalyst size dependencies for carbon nanotubes synthesis*, Phys. Stat. Sol. b **244**, 3911-3915 (2007).

[21] U. Queitsch, E. Mohn, F. Schäffel, L. Schultz, B. Rellinghaus, A. Blüher, M. Mertig, *Regular arrangement of nanoparticles from the gas phase on bacterial surface-protein layers*, Appl. Phys. Lett. **90**, 113114/1-3 (2007).

[22] M. H. Rümmeli, C. Kramberger, M. Löffler, M. Kalbac, H.-W. Hübers, A. Grüneis, A. Barreiro, D. Grimm, P. Ayala, T. Gemming, F. Schäffel, L. Dunsch, B. Büchner, T. Pichler, *Synthesis of single wall carbon nanotubes with invariant diameters using a modified laser assisted chemical vapour deposition route*, Nanotechnology **17**, 5469-5473 (2006).

Acknowledgements/Danksagung

An erster Stelle gilt mein tief empfundener Dank meinen Eltern, die mich auf meinem Weg immer unterstützt haben und mir gleichzeitig alle Freiheiten gelassen haben, meinen eigenen Weg zu finden.

Besonderer Dank gebührt Prof. Dr. Ludwig Schultz für die Möglichkeit, die Dissertation am IFW Dresden durchzuführen, für die sehr gute Betreuung während dieser Zeit und für seine konstante und engagierte Fürsprache bei Bewerbungen um Stipendien und Konferenzzuschüsse.

Ein herzliches Dankeschön an Prof. Dr. Gianaurelio Cuniberti für die Erstellung des zweiten Gutachtens und die Anleitung und Unterstützung meiner Bewerbung um ein Postdoc-Stipendium.

Ich bedanke mich außerdem bei Prof. Dr. Marc-Thorsten Hütt, der mir in einer schwierigen Phase meine Motivation zurückgegeben hat und mich ermutigt hat, die wissenschaftliche Laufbahn weiter zu verfolgen.

Ein großer Dank gilt Dr. Bernd Rellinghaus für die Betreuung meiner Dissertation und die Ermöglichung der Teilnahme an zahlreichen Konferenzen im In- und Ausland und der damit verbundenen Chance, wertvolle Kontakte zu knüpfen.

Mein tief empfundener Dank gilt Dr. Mark Rümmeli für die kontinuierliche Unterstützung und Anleitung während meiner Dissertation, für die Einführung in die Kohlenstoffnanomaterialien, das geduldige Lehren des wissenschaftlichen Handwerkszeugs und die vielen Diskussionen, "Ideenfindungsabende" und die Interpretationshilfe, die entscheidend zum Gelingen dieser Arbeit beigetragen haben.

Ein großer Dank gebührt außerdem Dr. Christine Täschner für die erfolgreiche Zusammenarbeit auf dem Gebiet der magnetischen Terminierung der Nanoröhren, Dr. Jamie Warner für die zahlreichen Diskussionen zum Ätzen von Graphen und ganz besonders Dipl.-Phys. Christoph Schünemann, meinem hoch motivierten Diplomanden, für seine

sehr engagierte und eigenständige Arbeit zu thermisch gewachsenen Nanoröhren und für das kostenfreie Verbreiten guter Laune.

Für die gute und erfolgreiche Zusammenarbeit in den verschiedenen Projekten meiner Dissertation bedanke ich mich weiterhin herzlich bei Dr. Alicja Bachmatiuk, Dr. Christian Kramberger, Dr. Thomas Gemming, Dr. Daniel Grimm, Rainer Kaltofen, Dr. Volker Neu, Prof. Dr. Paul McCormick, Dr. Siegfried Menzel, Elias Mohn, Prof. Dr. Thomas Pichler, Ute Queitsch, Darius Pohl, Maria Sparing, Geoff Trotter, Uhland Weißker und Dr. Ulrike Wolff.

Für die freundliche Unterstützung im Labor und in technischen Belangen danke ich Björn Bieniek, Sven Donath, Melanie Dudek, Irina Fiering, Michael Frey, Falk Herold, Cornelia Krien, Christine Mickel, Stephan Leger, Sieglinde Pichl, Almut Pöhl, Monika Siegert und Tina Sturm.

Vielen Dank auch an meinen very British roommate Tom für heiße Schokolade und englische Vokabelhilfe. Den nanonics sei Dank für die gelungene Abwechslung und Ablenkung.

Ein großes Dankeschön an meine Freunde Franziska, Ute, Tine, Torsten und Tobias für ein immer offenes Ohr und dafür, dass ihr mich erfolgreich daran erinnert, dass es eine Welt außerhalb des Instituts gibt.

Ich bedanke mich außerdem beim Cusanuswerk, das die Entstehung dieser Arbeit durch ein Stipendium gefördert hat.